



Universidad de la República

Facultad de Ingeniería

Instituto de Mecánica de los Fluidos e Ingeniería Ambiental

Wind gust forecast, in support of wind energy.

Ing. Alejandro Gutiérrez Arce

*Tutor Robert Fovell,
presentada para completar los requerimientos del
grado de Doctor en Mecánica de los Fluidos.*

Montevideo, Uruguay, Diciembre 2017

Agradecimientos

a:

- Andrea Esperanza y Candelaria por su paciencia y amor.
- Robert Fovell por su generosidad y paciencia.
- José Cataldo por su confianza y apoyo en todo momento.
- Gabriel Cazes por propiciar los primeros contactos UCLA, por haberme enseñado Linux y WRF, por haberme presentado y recomendado con Ann y Mechoso.
- Schenzer por todo lo que aprendo de turbomaquinas con el y por otras lecturas recomendadas.
- Roberto Mechozo por su hospitalidad conmigo y su compromiso en mejorar las condiciones de desarrollo en Uruguay, por tener siempre presente al IMFIA, por haberme presentado a Fovell.
- Ann por su simpatía, por su hospitalidad, por haber abierto su casa en los Angeles varias veces, por todo lo que aprendí del pueblo de EEUU a través de los largos intercambios de ideas con ella.
- Marcelo Romero y Davidson Moreira por iniciar un trabajo conjunto en la región y por las facilitar el acceso a nuevas capacidades de calculo que hoy tenemos disponibles.
- Los compañeros de Gerencia de Energía Eólica de UTE por hacer posible que por medio del SGE tengamos disponible la valiosa información de mediciones de energía eólica.
- Pablo P, Daniel y Ricardo porque siempre están disponibles para apoyar, porque me bancan cuando estamos apurados con los tiempos.
- Gabriel U por ayudarme en el Cluster-FING.

- Laura, Rodolfo, Gabriel y Valeria , por compartir el trabajo de enseñanza en estos años.
- Ignacio, Clauio, Everton, Sofia, Ivan, Federico, Vivian, Rodrigo A, Eliana, Pablo E, Ernesto, PBT, Martín, por compartir el trabajo en los proyectos recientes.
- La Gerencia y los compañeros del Despacho Nacional de Carga de UTE, por la buena disposición al trabajo conjunto, por la confianza, por el buen ambiente humano que construimos a partir del trabajo riguroso.
- A los compañeros de Facultad en especial aquellos con los que compartimos muchos desafíos que llevamos adelante en paralelo con este trabajo todos estos años, salud por los logros en varios planos. Por la buena onda que construimos en nuestro ambiente de trabajo, por las palabras de aliento en los días buenos, pero especialmente en los días malos que allí son más necesarias :).

Thanks

to:

- Andrea, Esperanza y Candelaria for they patience and love.
- Robert Fovell for his generosity and patience.
- José Cataldo for his trust and support for all the moments all the time.
- Gabriel Cazes for making possible my first contacts in UCLA, for teach me Linux and WRF, for presented and recommended me with Ann and Mechoso.
- Schenzer for all the thinks I learn every time about fluid machines and for the other literature lecture recommendation.
- Roberto Mechozo for his hospitality with me and his commitment in the improvement of the condition for the development of our country Uruguay, for have every time in mind IMFIA, for presented and recommended me with Fovell.
- Ann for his sympathy, hospitality, for open the doors of his house in LA, for all the learning about the EEUU workers people, for all the exchange ideas we have done.
- Marcelo Romero y Davidson Moreira for the start of the partner work in the region, for making possible the access to new computing resources available.
- the partner people of Wind Energy section in UTE for making possible with SGE we have access to the relevant observational data of wind.
- Pablo P, Daniel, Ricardo and Gonzalo for being always available to done the work, for the patience when we need to do the thinks quickly.
- Gabriel U, for help me with Cluster-FING.

- Laura, Rodolfo, Gabriel and Valeria, for share the teaching work all these years.
- Ignacio, Clauio, Everton, Sofia, Ivan, Federico, Vivian, Rodrigo A, Eliana, Pablo E, Ernesto, PBT, Martín, for share the works in projects.
- the partner of National Dispatch UTE, for the open mind to work together, the trust, the excellent work human environment we build with rigorous analysis in every step of the forecast development.
- the partners of the School of Engineering with special mention to all who we have share challenges in different dimensions, in all these years, good heath for all the thinks we have done. Thanks for being cool, in the good days (sunny days) and also in the bad day (with some cloud) which being cool is more necessary:).

Dedicatoria

*Este trabajo esta dedicado a Andrea, Esperanza y
Candelaria*

La ciencia y la técnica científica no se diferencian por sus métodos, sino solo por sus objetivos. La primera tiene que ver con el descubrimiento y establecimiento de las leyes que rigen los fenómenos naturales. La segunda busca objetivos útiles al hombre. El método de búsqueda en ambos casos es el método científico. Las técnicas científicas no pueden desarrollarse sin que exista una adecuada investigación científica pura, fuente de los conocimientos de donde deriva la información necesaria para procesar la nueva técnica. De los dos aspectos que comporta la libertad académica, la que se refiere a la elección del tema, debe ser preservada en los laboratorios tipo universitarios donde se hace ciencia solamente. En cambio, cuando se entra en el campo de la investigación aplicada, íntimamente conectada al proceso industrial, la libertad de tema queda sustituida por la conveniencia colectiva. Esta no puede aceptarse por mandato superior, sino que debe provenir del análisis científico, objetivo e imparcial de que la investigación propuesta efectivamente propende al bien social y no a mantener las ventajas de unos pocos sobre los más

Oscar Maggiolo, Ciencia y técnica, 1970.

Resumen

Recientemente un numero significativo de países han tomado la iniciativa de avanzar en el uso de la energía eólica, dicha tecnología convierte la energía cinética contenida en el viento en energía eléctrica suministrada a los sistemas eléctricos. Uruguay es uno de los países destacados estando en los primeros lugares en el mundo en lo que se refiere a la participación relativa de la energía eólica en el sistema. Esta realidad implica la necesidad de avanzar en el entendimiento de los fenómenos físicos relacionados con el viento en la Capa Limite Atmosférica (CLA). Dada la necesidad de cuantificar el recurso eólico y el desarrollo de parques eólicos, se han incrementado el numero de torres de medición instaladas en Uruguay. Estas torres registran mediadas típicamente a los 100 metros de altura sobre el nivel del suelo. Este trabajo fue posible dado el apoyo y la disponibilidad de datos brindados por parte de UTE. La motivación del presente trabajo es desarrollar un modelo de ráfagas a alturas del eje de los aerogeneradores, para su aplicación en la simulación numérica en modelos de circulación atmosférica de mesoescala. Este trabajo contiene simulaciones numéricas realizadas en Cluster FING-UdelaR, Unipampa, and SENAI CIMATEC cluster Yemoja.

Las ráfagas son relevantes para diferentes aplicaciones de la ingeniería. El desarrollo de un modelo operacional de pronóstico de variables asociadas al viento, resulta de ayuda para la gestión del sistemas eléctricos con altos niveles de participación de energía eólica como lo es el sistema uruguayo con una participación relativa de 35%.

Del análisis realizado se observa que tanto las ráfagas como el factor de ráfagas (definido como el cociente entre la ráfaga y la velocidad media) se incrementan en la medida que la atmosférica se vuelve menos estable, los resultados muestran un valor asintótico del factor de ráfaga igual a 1.33.

Se identifico un numero característico de Richardson Ri en los primeros 100 m sobre el nivel del suelo, para los casos de eventos de rafagas significativas $-0.2 < Ri < 0$. Todos los esquemas numéricos de CLA simulados en el modelo de mesoescala Weather Research and Forecast (WRF) subestiman el cortante en los primeros 100 metros de altura para condiciones de eventos de

ráfaga $g > 15m/s$. Es sobrestimado el Ri para todos los esquemas numéricos simulados.

Para todos los esquemas de CLA simulados, el modelo clásico basado en la velocidad media y la velocidad de fricción ECMWF, muestra capacidad de pronosticar ráfagas a las alturas típicas de los ejes de los aerogeneradores (100 m) con mejores resultados a medida que se aumenta la resolución de la grilla. Proponemos una parametrización de ráfagas (Gust Parametrization GP) discriminando la estabilidad a partir del gradiente vertical de temperatura $\frac{\partial T}{\partial z}$, una discriminación de eventos de ráfagas significativas por el numero de Ri , calculando la velocidad en el tope de la CLA (V_{MAX}) como variable de entrada en la parametrización.

El GP muestra mejor desempeño en el dominio de menor resolución (12 km). Se observa un incremento de la velocidad media y las ráfagas pronosticadas, a medida que se incrementa la resolución horizontal del modelo, se observan mejores resultados en el pronostico de las rafagas a medida que aumenta la resolución del modelo. Analizando los intervalos de tiempo para el desarrollo de un sistema de alarmas, se observa un incremento de aciertos y un descenso en las falsas alarmas a medida que aumenta el intervalo de tiempo considerado. El modelo GP propuesto puede ser de utilidad en modelos operacionales dado su mejor desempeño en el dominio de menor resolución de grilla horizontal, lo que implica que puede ser implementado con menores costos computacionales. En este trabajo no se evaluó el horizonte de pronostico, el mismo puede ser considerado como una evaluación de modelos en términos de identificar las configuraciones más adecuadas. En el caso de la implementación de un modelo operacional, se debe analizar el impacto del horizonte de pronostico en el desempeño, así como el impacto del uso de corridas de conjuntos.

Abstract

Recently, a number of countries have taken new initiatives with regard to energy technology applications related to the installation of wind turbines, which convert the kinetic energy of the wind into electric power to supply electricity systems. Uruguay, in particular, is one of the countries at the forefront of new energy technology applications; currently, the country's relative wind power participation rate is one of the highest in the world. This reality implies the need for a better understanding of the physical phenomena related to wind in the atmospheric planetary boundary layer (PBL). Given the need to quantify wind resources for the development wind farms, the number of towers collecting new observational data in Uruguay has increased. These towers are typically located 100 meters above ground level (AGL). The present work was possible due the assistance provided by the National Electric Company of Uruguay (UTE), which provided access to wind data.

The aim of this work was to develop a wind gust parametrization model at wind turbine height, based on numerical simulation of a mesoscale model. This thesis contains results of numerical simulations run on the Cluster FING-UdelaR, Unipampa, and SENAI CIMATEC cluster Yemoja.

Wind gusts are relevant to different wind engineering applications. Therefore, development of an operational wind forecast model could help manage electrical systems with relatively high levels of wind power participation, such as those in Uruguay, which has a wind power participation of 35 %. It was observed that both gust magnitude and factors (the ratio of gusts to mean wind speed) increased as the atmosphere became less stable, and the results indicated an asymptotic gust factor value of 1.33. A characteristic observed bulk Richardson number Ri was identified for gusty cases $-0.2 < Ri < 0$ in the first 100 meters AGL. All PBL schemes run in the mesoscale Weather Research and Forecast (WRF) model under-predict the shear in the first 100 m for gusty cases when observed gust $g > 15m/s$. The forecast Ri is over-predict for all PBL schemes.

For all PBL schemes, the established, theory-based gust parameterizations based on mean velocity and friction velocity data from the ECMWF

model provided reasonable forecasts of the gusts at hub wind turbine height (100 m) with increasing skill as the grid resolution was increased. We propose a gust parameterization (GP) that includes a discrimination of stability computing $\frac{\partial T}{\partial z}$, and discrimination of gusty cases based on Ri , computing the velocity at the top of the PBL V_{MAX} as an input in the parameterization. The GP shows better performance in the gross domain (12 km). Increased mean and gust values were forecast with increasing horizontal grid resolution, and it was observed that skill at forecasting gusty cases increased with increasing grid resolution. Analysis of time intervals for forecast alarms for gusty cases showed an increase in true alarms and a decrease in false alarms when the time interval increased. The proposed GP can be useful in an operational model because of better skill in gross domain, which means, could be implemented with lower computational cost. This work did not evaluate the forecast horizon, and can be considered as providing better configuration relative to other models. If an operational model is to be implemented, further analysis of the time horizon and impact on skill while working with ensembles need to be computed.

Contents

1	Introduction	1
2	Atmospheric and Numerical Models	7
2.1	Atmospheric and Numerical Models	7
2.2	Mesoscale models	10
2.3	Basic equations in mesoscale models	11
2.4	Physics parameterizations	14
2.4.1	Microphysics of clouds	15
2.4.2	Cloud Parameterization and Cloud-Resolving Models	16
2.4.3	Radiation	17
2.4.4	Land surface	17
2.4.5	Planetary boundary Layer (PBL)	18
2.4.6	Physics interactions between parameterizations	18
2.5	Limit between mesoscale and large-eddy simulation models	20
3	Planetary Boundary Layer (PBL)	22
3.1	PBL Parametrizations	29
3.2	Atmospheric surface layer	31
3.3	Parameterizations and local closure order	37
3.3.1	First-order closure	37
3.3.2	One-and-a-half-order closure	38
4	Wind Gusts: observational data	41
4.1	Analysis of wind gust observational data	45
4.1.1	Extreme wind gust cases	56

5	Numerical model and methods	62
5.1	The Weather Research and Forecasting (WRF) model	62
5.2	Numerical model and methods	62
6	Gust model formulations	65
6.1	Gust model formulations	65
6.1.1	The ECMWF reference wind model	65
6.1.2	Analysis of the vertical structure of PBL schemes . . .	66
6.1.3	Surface layer sensitivity	70
6.1.4	Stability discrimination analysis	71
6.1.5	Proposed Gust Parameterization (GP)	73
7	Analysis of numerical results	79
7.1	Analysis of discrimination of gusty cases with Ri in GP	80
7.2	Wind gust alarms	82
7.3	Skill of forecast gust with increasing horizontal grid resolution	83
7.4	Skill of alarms, for all PBL schemes and resolutions	90
8	Conclusion	92
9	Appendix	94
9.1	Diurnal cycle by seasons of mean wind observed and forecast velocity by each PBL scheme	94
9.2	Diurnal cycle by seasons of PBL height computed by different schemes	103
9.3	Gust Parametrization Coefficients	104
	Bibliography	112

List of Figures

2.1	National Aeronautics and Space Administration (NASA) satellite view of Earth from space.	8
2.2	Global budget of energy in the atmosphere from [Trenberth, 2009] (on the left) and the vertical temperature profile of the layers of the atmosphere (on the right).	9
2.3	Time and length scale in mesoscale models from [Markowski, 2010]	11
2.4	Processes included in typical general circulation models [Randall, 2000]	15
2.5	Scheme of the radiation processes included under radiation parameterizations	18
2.6	A schematic of the turbulence spectrum in the horizontal plane as a function of the horizontal wavenumber magnitude [Wyngaard, 2004]	21
3.1	The troposphere can be divided into two parts: a boundary layer (shaded) near the surface and the free atmosphere above it. [Stull, 1988]	23
3.2	Residual Layer and convective mixed layer: evolution over time [Stull, 1988]	24
3.3	Plot of observational data taken at the Colonia Eulacio tower on December 6, 2014. From [de Almeida, Gutierrez, 2015] . . .	26
3.4	Plot of observational data taken at the Colonia Eulacio tower on July 15, 2015. From [de Almeida, Gutierrez, 2015]	27

3.5	Diurnal cycle of solar irradiance W/m^2 using data recorded at the Colonia Rubio tower by season (summer, autumn, winter, and spring) in 2012; data shown are hourly mean value and 16th and 84th percentiles (vertical bars) and are sourced from [Gutierrez, 2015].	28
3.6	Diurnal cycle of the shear $\frac{\partial V}{\partial z}$ (1/s) between 60–80 m (blue) and 80–101 m (red), discriminated by season (summer, autumn, winter, and spring 2012), measured at the Colonia Rubio tower. Values shown are the hourly mean value and the 16th and 84th percentiles vertical bars [Gutierrez, 2015].	29
3.7	Dimensionless wind shear with the interpolation formula in the surface layer [Businger, 1971]	34
3.8	Dimensionless temperature gradient with the interpolation formula in the surface layer [Businger, 1971]	35
3.9	Typical variation of K_m with height. Taken from [Stull, 1988]	38
4.1	Instruments with orthogonal azimuths on top of the Colonia Eulacio (CE) tower	42
4.2	Locations and topography (m) of towers from where observational data was measured	43
4.3	Photographs taken from different directions near the location of the Colonia Eulacio tower.	44
4.4	Diurnal variation in the gradient of temperature at the Aparicio Saravia (AS) tower (red; temperatures measured at 99 m and 5 m), the Jose Ignacio (JI) tower (blue; temperatures measured at 98 m and 12 m), and the Rosendo Mendoza (RM) tower (black; temperatures measured at 100 m and 2 m, (C°/m)). Vertical bars show 16th and 84th percentiles, and the horizontal green line marks the dry adiabatic lapse rate $\Gamma = -0.0098C^\circ/m$	47
4.5	Diurnal variations in the gust factor at Aparicio Saravia (AS) tower (red; 101 m), Jose Ignacio (JI) tower (blue; 98 m) and Rosendo Mendoza (RM) tower (black; 101 m). Vertical bars show the mean and 16th and 84th percentiles.	49

4.6	Left-hand column: gust factor versus mean velocity (strongly stable regime, i.e., when stable when $0.01C^\circ/m \leq \frac{\partial T}{\partial z}$; green), right-hand column: gust versus mean velocity (strongly stable regime) at Aparicio Saravia (AS; 101 m tall), Jose Ignacio (JI; 98 m tall), and Rosendo Mendoza (RM; 101 m tall).	51
4.7	Left-hand column: gust factor versus mean velocity (slightly stable regime, i.e., when $0C^\circ/m \leq \frac{\partial T}{\partial z} < 0.01C^\circ/m$; blue), right-hand column: gust versus mean velocity (slightly stable regime) at Aparicio Saravia (AS; 101 m), Jose Ignacio (JI; 98 m), and Rosendo Mendoza (RM; 101 m).	52
4.8	Left-hand column: gust factor versus mean velocity (proximity to adiabatic lapse rate (near neutral, i.e., when $-0.01C^\circ/m \leq \frac{\partial T}{\partial z} < 0C^\circ/m$; magenta)), right-hand column: gust versus mean velocity (proximity to adiabatic lapse rate (near neutral)) at Aparicio Saravia (AS; 101 m), Jose Ignacio (JI; 98 m), and Rosendo Mendoza (RM; 101 m).	53
4.9	Left-hand column: gust factor versus mean velocity (unstable adiabatic conditions, i.e., when $\frac{\partial T}{\partial z} < -0.01C^\circ/m$; red), right-hand column: gust versus mean velocity (unstable adiabatic conditions) at Aparicio Saravia (AS; 101 m), Jose Ignacio (JI; 98 m), and Rosendo Mendoza (RM; 101 m).	54
4.10	Left-hand column: gust factor versus mean velocity, right-hand column: gust versus mean velocity at Aparicio Saravia (AS; 101 m), Jose Ignacio (JI; 98 m), and Rosendo Mendoza (RM; 101 m). Scatterplot colors show all classes of stability regimes defined; the black line represents a GF asymptotic value of 1.33	55

4.11	Data from the Colonia Eulacio (CE) tower including histograms $\frac{\partial V}{\partial z}$ of measurements taken from heights of 101.8 m and 10.1 m (in the first row). Histograms in the second row show the vertical temperature gradient $\frac{\partial T}{\partial z}$ measured at 100.8 m and 3.4 m. The left-hand column shows the relative frequencies of all cases analyzed in one year, the middle column shows the histogram of $g > 15m/s$, and the right-hand column shows $g > 20m/s$	57
4.12	Data from the Jose Ignacio (JI) tower, including histograms of relative frequency $\frac{\partial V}{\partial z}$ measured at 98 m and 12 m. The second row shows the vertical temperature gradient $\frac{\partial T}{\partial z}$ measured at 98 m and 12 m. The left-hand column shows the relative frequencies of all cases analyzed in one year, the middle column shows the histogram $g > 15m/s$, and the right-hand column shows $g > 20m/s$	58
4.13	Scatterplot of Ri and gust g (m/s) in 2012 for the Jose Ignacio (JI) tower, and for August 8, 2014 to August 7, 2015 for the Colonia Eulacio (CE) tower	60
4.14	Histogram of Ri for cases when $g > 15m/s$ during 2012 for Jose Ignacio (JI) and from August 8, 2014 to August 7, 2015 for Colonia Eulacio (CE)	61
5.1	Telescoping Weather Research and Forecasting (WRF) domains with horizontal grids of 12 km, 4 km, 1.3 km, and 444 m	63
6.1	Histogram of shear between $\frac{\partial V}{\partial z}$ (~ 100 m and ~ 10 m) (1/s) in cases where $g > 15m/s$ at the top of the CE tower (101.8 m AGL), modeled using PBL schemes YSU, MYJ, ACM2–Pleim, Boulac, Bretherton–Park, and GBM–TKE PBL, with a horizontal grid resolution of 4 km.	67

6.2	Histogram of the vertical temperature gradient $\frac{\partial T}{\partial z}$ (~ 100 m and ~ 10 m) (C°/m) in cases where $g > 15m/s$ measured at the top of the CE tower (101.8 m AGL), using the PBL schemes YSU, MYJ, ACM2–Pleim, Boulac, Bretherton–Park, and GBM–TKE PBL, with a horizontal grid resolution of 4 km.	68
6.3	Ri computed with the WRF model using six different planetary boundary layer schemes with a horizontal grid resolution of 4 km, when the observed gust in tower CE was > 15 m/s.	69
6.4	Histogram of shear $\frac{\partial V}{\partial z}$, vertical temperature gradient $\frac{\partial T}{\partial z}$, and Ri (~ 100 m and ~ 10 m) in cases where $g > 15m/s$ at the top of the CE tower (101.8 m AGL), for Shin–Hong and MYNN PBL schemes	71
6.5	PBL simulated height vs. observed gusts in the CE tower, for the PBL schemes YSU, MYJ, ACM2–Pleim, Boulac, Bretherton–Park, GBM–TKE, Shin–Hong, and MYNN, with a 4 km horizontal grid. Green dots represent $\frac{\partial T}{\partial z} > 0$ and red dots represent $\frac{\partial T}{\partial z} \leq 0$; the color codes are as computed by the WRF model	72
6.6	PBL simulated height vs. observed gusts in the CE tower, for the PBL schemes YSU, MYJ, ACM2–Pleim, Boulac, Bretherton–Park, GBM–TKE, Shin–Hong, and MYNN, with a 4 km horizontal grid size. Green dots represent $\frac{\partial T}{\partial z} > 0$ and red dots represent $\frac{\partial T}{\partial z} \leq 0$; the color codes are as computed by temperatures observed in the CE tower	73
6.7	K and $Gmin$ fit optimally with the CE tower observational data for Shin–Hong horizontal grid resolutions of 12 km and 0.44 km. Blue represents $\frac{\partial T}{\partial z} \geq 0$ and red represents $\frac{\partial T}{\partial z} < 0$. Intervals of velocities computed with the WRF model are $0m/s < V \leq 5m/s$, $5m/s \leq V < 9m/s$ and $9m/s \leq V$	76
6.8	Schematic of further relevant parameters proposed for gust parameterization formulations, for wind turbine hub height in unstable conditions.	78

7.1	Shin-Hong PBL, using 4 km grid resolution, for the RM tower. The left-hand column shows forecast gust Ri when $S_{Ri} = 1$ and the right-hand column shows forecast gust when $S_{Ri} = 1.15$. The blue dots show all cases, the magenta dots show cases when the observed gust $g > 15m/s$, and the green line shows $g = 15m/s$. The bottom row shows the histograms of errors for gusty cases when observed gust $g > 15m/s$	81
7.2	ECMWF g (m/s) vs. GP (m/s) gusts forecast at the RM tower, using the Shin-Hong PBL scheme at 12 km, 4 km, 1.3 km, and 0.44 km horizontal grid resolution. Red dots show gusts observed at $g > 15m/s$ for 1 h.	84
7.3	ECMWF g (m/s) vs. GP (m/s) gusts forecast at the RM tower, using the Shin-Hong PBL scheme for 12 km, 4 km, 1.3 km, and 0.44 km horizontal grid resolution. Red dots show gusts observed at $g > 15m/s$ for 6 h.	85
7.4	ECMWF g (m/s) vs. GP (m/s) gusts forecast at the RM tower, using the Shin-Hong PBL scheme for 12 km, 4 km, 1.3 km, and 0.44 km horizontal grid resolution. Red dots show gusts observed at $g > 15m/s$ for 12 h.	86
7.5	ECMWF g (m/s) vs. GP (m/s) gusts forecast at the RM tower, using the Shin-Hong PBL scheme for 12 km, 4 km, 1.3 km, and 0.44 km horizontal grid resolution. Magenta dots show gusts observed at $g < 15m/s$ for 1 h.	87
7.6	ECMWF g (m/s) vs. GP (m/s) gusts forecast at the RM tower, using the Shin-Hong PBL scheme for 12 km, 4 km, 1.3 km, and 0.44 km horizontal grid resolution. Magenta dots show gusts observed at $g < 15m/s$ for 6 h.	88
7.7	ECMWF g (m/s) vs. GP (m/s) gusts forecast at the RM tower, using the Shin-Hong PBL scheme for 12 km, 4 km, 1.3 km, and 0.44 km horizontal grid resolution. Magenta dots show gusts observed at $g < 15m/s$ for 12 h.	89

9.1	Mean wind velocity at 101.8 meters at CE tower diurnal cycle by seasons, blue observed velocity, red computed by WRF with YSU PBL scheme, 4 km horizontal grid resolution, vertical bar considering 16th and 84th percentiles.	95
9.2	Mean wind velocity at 101.8 meters at CE tower diurnal cycle by seasons, blue observed velocity, red computed by WRF with MYJ PBL scheme, 4 km horizontal grid resolution, vertical bar considering 16th and 84th percentiles.	96
9.3	Mean wind velocity at 101.8 meters at CE tower diurnal cycle by seasons, blue observed velocity, red computed by WRF with ACM2-Pleim PBL scheme, 4 km horizontal grid resolution, vertical bar considering 16th and 84th percentiles.	97
9.4	Mean wind velocity at 101.8 meters at CE tower diurnal cycle by seasons, blue observed velocity, red computed by WRF with Bretherton Park PBL scheme, 4 km horizontal grid resolution, vertical bar considering 16th and 84th percentiles.	98
9.5	Mean wind velocity at 101.8 meters at CE tower diurnal cycle by seasons, blue observed velocity, red computed by WRF with Bretherton-Park PBL scheme, 4 km horizontal grid resolution, vertical bar considering 16th and 84th percentiles.	99
9.6	Mean wind velocity at 101.8 meters at CE tower diurnal cycle by seasons, blue observed velocity, red computed by WRF with GBM PBL scheme, 4 km horizontal grid resolution, vertical bar considering 16th and 84th percentiles.	100
9.7	Mean wind velocity at 101.8 meters at CE tower diurnal cycle by seasons, blue observed velocity, red computed by WRF with Shin-Hong PBL scheme, 4 km horizontal grid resolution, vertical bar considering 16th and 84th percentiles.	101
9.8	Mean wind velocity at 101.8 meters at CE tower diurnal cycle by seasons, blue observed velocity, red computed by WRF with MYNN PBL scheme, 4 km horizontal grid resolution, vertical bar considering 16th and 84th percentiles.	102

- 9.9 Diurnal cycle by seasons of PBL height computed by different schemes, 4 km horizontal grid resolution, blue YSU, red MYJ, yellow ACM2, black Bretherton Park, cyan Shin-Hong, green MYNN, vertical bar considering 16th and 84th percentiles . . . 103
- 9.10 K and $Gmin$ optimal fit with CE tower observational data for YSU 12km and 0.44km horizontal grid resolution, blue for $\frac{\partial T}{\partial z} \geq 0$ and red for $\frac{\partial T}{\partial z} < 0$, intervals of velocities computed by WRF $0m/s < V \leq 5m/s$, $5m/s \leq V < 9m/s$ and $9m/s \leq V$. 104
- 9.11 K and $Gmin$ optimal fit with CE tower observational data for MYJ 12km and 0.44km horizontal grid resolution, blue for $\frac{\partial T}{\partial z} \geq 0$ and red for $\frac{\partial T}{\partial z} < 0$, intervals of velocities computed by WRF $0m/s < V \leq 5m/s$, $5m/s \leq V < 9m/s$ and $9m/s \leq V$. 105
- 9.12 K and $Gmin$ optimal fit with CE tower observational data for YSU 4km and 1.3km horizontal grid resolution, blue for $\frac{\partial T}{\partial z} \geq 0$ and red for $\frac{\partial T}{\partial z} < 0$, intervals of velocities computed by WRF $0m/s < V \leq 5m/s$, $5m/s \leq V < 9m/s$ and $9m/s \leq V$. 106
- 9.13 K and $Gmin$ optimal fit with CE tower observational data for Buolac 12km and 4km horizontal grid resolution, blue for $\frac{\partial T}{\partial z} \geq 0$ and red for $\frac{\partial T}{\partial z} < 0$, intervals of velocities computed by WRF $0m/s < V \leq 5m/s$, $5m/s \leq V < 9m/s$ and $9m/s \leq V$. 107
- 9.14 K and $Gmin$ optimal fit with CE tower observational data for Bretherton Park 12km and 4km horizontal grid resolution, blue for $\frac{\partial T}{\partial z} \geq 0$ and red for $\frac{\partial T}{\partial z} < 0$, intervals of velocities computed by WRF $0m/s < V \leq 5m/s$, $5m/s \leq V < 9m/s$ and $9m/s \leq V$ 108
- 9.15 K and $Gmin$ optimal fit with CE tower observational data for GBM-TKE 12km and 4km horizontal grid resolution, blue for $\frac{\partial T}{\partial z} \geq 0$ and red for $\frac{\partial T}{\partial z} < 0$, intervals of velocities computed by WRF $0m/s < V \leq 5m/s$, $5m/s \leq V < 9m/s$ and $9m/s \leq V$. 109
- 9.16 K and $Gmin$ optimal fit with CE tower observational data for Shin-Hong 4km and 1.3km horizontal grid resolution, blue for $\frac{\partial T}{\partial z} \geq 0$ and red for $\frac{\partial T}{\partial z} < 0$, intervals of velocities computed by WRF $0m/s < V \leq 5m/s$, $5m/s \leq V < 9m/s$ and $9m/s \leq V$. 110

9.17 K and $Gmin$ optimal fit with CE tower observational data for MYNN 12km and 14km horizontal grid resolution, blue for $\frac{\partial T}{\partial z} \geq 0$ and red for $\frac{\partial T}{\partial z} < 0$, intervals of velocities computed by WRF $0m/s < V \leq 5m/s$, $5m/s \leq V < 9m/s$ and $9m/s \leq V$. 111

List of Tables

2.1	Physics Interactions. Columns correspond to model physical processes: radiation (Rad), microphysics (MP), cumulus parameterization (CP), planetary boundary layer/vertical diffusion (PBL), and surface physics (Sfc). Rows correspond to model variables, where i and o indicate whether a variable is an input or an output (updated) by a physical process. [Skamarock, 2008]	19
4.1	Tower locations, height of measurement considered, and period of analysis	45
5.1	PBL parameterizations scheme order of closure and height computing method	64
7.1	True alarm (TA) and false alarm (FA) conditions for reference model ECMWF (EU) and the proposed GP model (GP) for all PBL schemes and grid horizontal resolutions within the time window at the RM tower from August 8, 2014, to August 7, 2015	90

Chapter 1

Introduction

When we refer to wind, we mean the flux of air in the planetary boundary layer (PBL). The relevant variables to describe wind are mean velocity and gust, the latter being the peak of the velocity of the flux. Recently, a number of countries have taken new initiatives in energy technology applications related to the installation of wind turbines. Such turbines convert the kinetic energy of wind into electric power to supply a grid. Uruguay, in particular, has been quite proactive in this regard; its relative wind power participation is one of the highest in the world today. Thus, there is a need to improve our understanding of the lowest region of the atmosphere. In the recent decades, towers collecting new observational data up to 100 m above ground level (AGL) have been constructed in Uruguay given the need to quantify wind resources for the development of wind farms. The present work was possible due the National Electric Company of Uruguay (UTE), which provided access to wind data.

The aim of this work was to develop a wind gust parametrization at wind turbine height, based on numerical simulation of a mesoscale model. This thesis contains results of numerical simulations run on the Cluster FING-UdelaR, UNIPAMPA, and SENAI CIMATEC cluster Yemoja.

Wind gusts are measured as the maximum wind speed observed over a fixed period. [Friederichs, 2009] argues that reliable forecasts of wind gusts can potentially mitigate the destruction and human losses they can cause. Thus, it is crucial to improve the quality of gust warnings. Wind gusts are relevant in different wind engineering applications. Therefore, development

of an operational wind forecast model could help in managing electrical systems with relatively high levels of wind power participation [Ackerman, 2005], [Fox, 2014] such as those in Uruguay, which has a wind power participation of 35 % [web, UTE]. Considering the magnitudes of wind gusts, the control configurations of commercial wind turbines define the cut-out velocity as 15–25 m/s, depending on the model of the wind turbine. When the wind gust measured by wind anemometers installed at the turbine hub exceeds the cut-out velocity, the machine abruptly stops. Cut-out events pose a risk because they cause transitory changes in power flux transmissions in electric lines [Anca, 2010]. Also, since wind gusts can occur at synoptic or mesoscale times and lengths, the entire electric grid may be at risk of damage when extreme wind gusts occur, which would in turn affect electricity supply.

In determining the region of the atmosphere of interest for wind energy applications, it is observed that the wind blades at onshore wind farms sweep areas at 60–120 m AGL; new technological applications of wind power provide data at heights that were previously not rigorously studied. This region lies within the atmospheric boundary layer (ABL) or the PBL. The PBL is closest to the terrestrial surface and is directly affected by exchanges of momentum, heat, and mass with the surface. The region of the PBL closest to the ground is called the surface layer (SL) [Monin, 1954]. The region above the SL after sunset is known as the residual layer (RL); after sunrise, it is called the convective mixed layer (CML) [Stull, 1988]. The CML increases in height throughout the morning, reaching a height of 1–2 km by mid-afternoon. At sunset, a rapid decrease in turbulent motion in the boundary layer occurs as buoyant plumes that maintain the motion lose their energy source near the surface. This is because the ground cools quickly as radiative heat is lost to space. The diurnal solar radiation cycle thus determines the condition of stability in the PBL. Periodic changes that occur in the vertical structure of the atmospheric region over the course of one day were analyzed in this work. The early evening surface layer transition was analyzed in previous research [Acevedo, 2001], which revealed abrupt changes in this region of the atmosphere in the evening under clear skies. The stable and unstable conditions of the atmosphere can be classified with the vertical temperature gradient [Arya, 1998]. This parameter is relevant in this study because data

availability of temperature measured at different heights in towers enables a clearer description of the physics associated with gusts. Wind energy is harvested at the lowest region of the PBL, where diurnal changes associated with heating and cooling of the surface terrain are strong.

Wind gusts inside the PBL are phenomena that develop at mesoscale range [Orlanski, 1975], and are associated with the length as well as the time scales. [Fujita, 1981] presented more detail regarding the spatial and temporal scales of tornadoes and downbursts. Wind gusts can be produced by thunderstorms, downbursts, convective systems, and other mesoscale phenomena with spatial scales ranging from hundreds of meters to hundreds of kilometers. [Markowski, 2010] described the physics and scale in addition to the nondimensional parameters for computing the characteristic mesoscales of different physical phenomena, using the Brunt–Väisälä frequency (N). Generally, $N^2 = (g/\Theta_V \frac{\partial \Theta_V}{\partial z})$, where Θ_V is the virtual potential temperature. In this case, the frequency of the buoyancy oscillation also depends on the contribution of water vapor to the buoyancy. The mesoscale is directly related to local geographic conditions such as topography or distance to the sea. In the present work, an analysis of historical observational data from different regions is followed by a numerical results model focused on one defined region.

[Wyngaard, 2004] reported that in real mesoscale phenomena, the spatial scale of the energy- and flux-containing turbulence is much smaller than the scale of the spatial filter used in equations of motion in the mesoscale numerical model. The present study demonstrates improvements in wind gust simulation when a horizontal grid with higher resolution is used.

[Floors, 2013] reported that traditionally, it has been difficult to verify mesoscale model wind predictions against observations in the PBL.

[Shin and Hong, 2013] examined the grid-size dependencies of resolved and parameterized vertical transports in convective boundary layers (CBLs) for horizontal grid scales, including the gray zone [Wyngaard, 2004], which includes scales with no explicit resolution by the model.

A recent version of the Weather Research and Forecast (WRF) model introduced grid horizontal size dependency in the parameterization of the unresolved vertical transport in PBL [Shin and Hong, 2015].

[Siuta, 2017] evaluated the use of a WRF ensemble model for short-term, hub-height wind speed forecasts in a complex terrain. That work analyzed eight PBL schemes using post-processing with a probabilistic approach.

[Wieringa, 1973] analyzed wind measurement data for wind gusts at different heights (between 8–80 m), wherein extreme measurements were collected from open and city sides. In this work, the relationship among gust, friction velocity, and standard deviation of measurements was analyzed, and the data presented were classified according to the Pasquill stability classes.

The European Centre for Medium-Range Weather Forecasts (ECMWF) [IFS, 2011] has presented a gust model based on [Panofky, 1977]. [Gray, 2003] used an algorithm to predict maximum convective gust in the formulation, in which gust is computed by considering cloud top height, cloud depth, and a defined vertical virtual potential temperature.

[Sheridan, 2011] summarized different parameterizations for the most relevant nonconvective and convective gusts. The documented parameterizations have formulations similar to those of the ECMWF, which include the components of mean velocity and friction velocity. A second group of convective gust formulations has been reported in closer relation to the formulations of [Nakamura, 1996]. [Friederichs, 2009] tested different predictor variables for 10 m wind gusts and reported that the most informative predictor is the ECMWF 10 m wind velocity model.

[Fovell, 2016] presented an analysis of gusts using ECMWF models in a complex terrain in two tower locations of the mesonet observational network in San Diego County. The wind was measured at a height of 6.1 m AGL. Fovell focused on the the Santa Ana winds occurring in southern California from September–May. Gust magnitudes were found to have pronounced diurnal cycles, with the highest wind gust frequencies occurring between 15:00–18:00 UTC.

[Gutierrez and Fovell, 2015] analyzed a subset of towers representing three different regions of Uruguay, and observed that gust magnitudes and factors increased as the atmosphere became less stable. This previous work includes the relevant results of the aforementioned research in wind gust variations, including those under stable and unstable atmospheric conditions.

The present work analyzes measurements from towers in Uruguay, a

south-central region of South America, with a focus on forecasting gusts at about 100 m AGL using targeted WRF and Advanced Research WRF (ARW) core [Skamarock, 2008] simulations. Different PBL schemes available in the WRF model were run for a selected period of 365 continuous days, using high-quality observational data with increasing horizontal grid resolutions. Grid resolutions of 4 km and higher, with a cloud-resolving model [Arakawa, 2004], and two PBL schemes with telescoping domains of 1.3 km and 0.44 km, were run. These included a region in which two wind measurement observational towers represented the same mesoscale conditions.

Our work analyzes the applicability of the ECMWF model at 100 m AGL. A gust parameterization model that considers atmospheric stability and Ri as dimensionless characteristic parameters to discriminate gusty cases is proposed. Both gust models are compared to approaches with different PBL schemes and increasing horizontal grid resolutions. Gusts are first described with observational data, and the applicability of the ECMWF model at 100 m AGL is analyzed. Then, a gust parameterization model is formulated considering stability in the atmosphere and a Richardson number Ri as nondimensional forecast parameters for identifying gusty cases. Both gust model approaches are compared by running eight different PBL schemes and increasing horizontal grid resolutions.

The analyzed gust models are used to develop a gust alarm model defining the time interval for which a forecast gust is greater than a selected wind gust value. The proposed alarm is analyzed with the main objective of developing an operational model that can provide the probability of a power ramp in an electric system with a high level of wind power participation.

This work is organized as follows. Chapter 2 summarizes the formulation of atmospheric circulation models and the parametrization considered in mesoscale numerical models. Chapter 3 includes the theoretical approach to the numerical formulation of the PBL and SL parameterizations.

In Chapter 4, the observational wind measurement data are described, followed by the observed diurnal cycle, and the relationship between stability regime and extreme wind gust cases are analyzed with a focus on the formulation of a wind gust parametrization. Chapter 5 presents the PBL parametrization, domains, and mesoscale model run in the present work.

Chapter 6 shows the ECMWF gust model and the gust parameterization proposed and developed in the present work, and analyzes the ability of different PBL schemes to compute shear and vertical gradients of temperature. The skill of wind gust models, independence of horizontal grid resolution, and PBL scheme are described in Chapter 7. Finally, Chapter 8 presents the conclusions.

Chapter 2

Atmospheric and Numerical Models

2.1 Atmospheric and Numerical Models

The American Meteorological Society glossary [AMS glossary, 2017] examines images of the Earth from space (Figure 2.1), and intricate cloud structures can be seen. Water in Earth’s atmosphere plays a very important role in the energy cycle; because of its chemical composition, most incoming sunlight passes through Earth’s atmosphere and is absorbed at the planet’s surface. Part of this heat is transported back to the atmosphere through sensible heat and moisture fluxes.

The thermodynamics of water vapor are crucial to the existence of severe storms in the Earth’s atmosphere. Since more solar radiation is absorbed in the tropics than at high latitudes, the atmosphere transports heat poleward, as do the oceans. These motions, heavily altered by the effects of planetary rotation, determine the atmospheric general circulation. Fluid dynamic instabilities play a large role in this circulation and are crucial in determining fluctuations in it; these are known as “weather”. The atmosphere is divided into several layers according to their thermal and ionization structures. The region where the temperature decreases because of the upward heat flux is called the troposphere; the lowest level of troposphere, and that closest to the Earth’s surface, is the PBL.

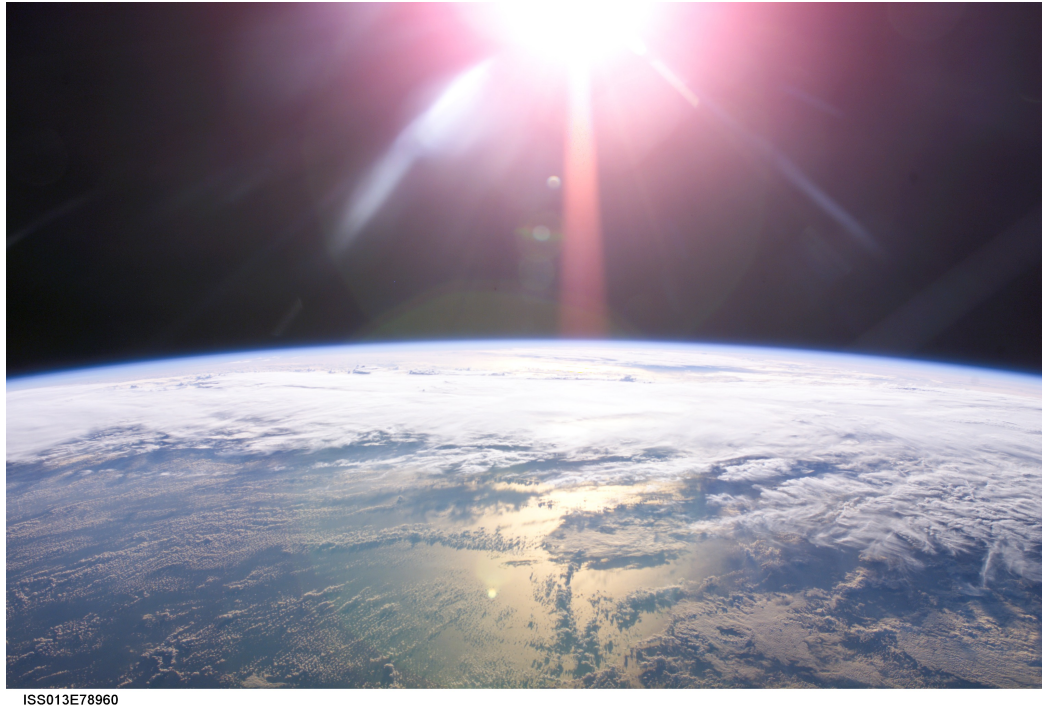


Figure 2.1: National Aeronautics and Space Administration (NASA) satellite view of Earth from space.

The total mass of the atmosphere is approximately $5,3 \times 10^{18}$ kg. Solar radiation is the primary energy that creates the fluid dynamic motion and makes life on our planet possible. In figure 2.2, the mean global energy budget of one year (W/m^2), is presented on the left as given in [Trenberth, 2009], and the vertical temperature profile in the atmosphere appears on the right-hand side. Taking account of the fact that the mean incoming solar radiation in one year is $341.3 W/m^2$, only a small part of this becomes wind (a flux of air in the atmosphere in the region closer to the Earth's surface, which is also referred to as mean kinetic energy).

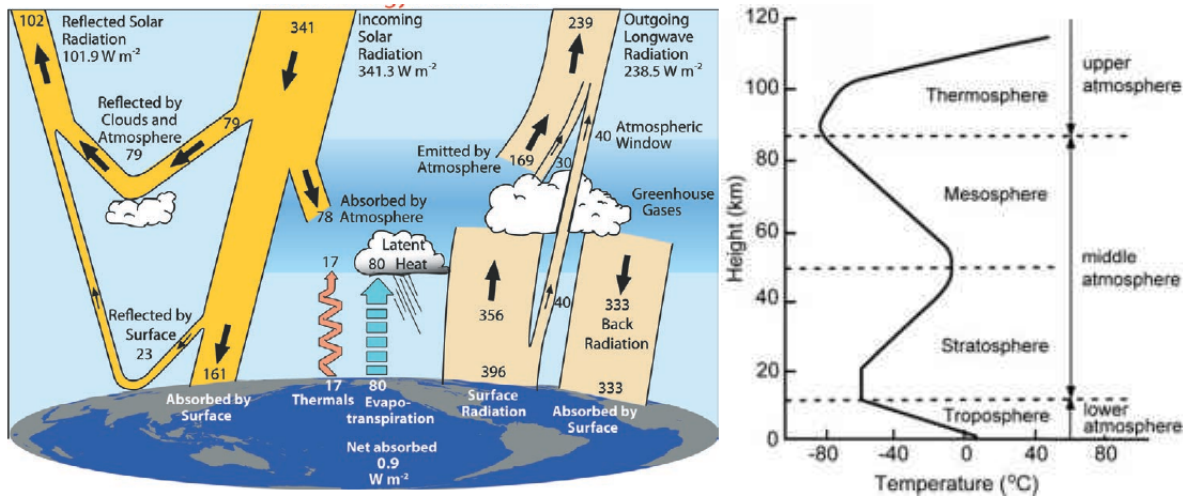


Figure 2.2: Global budget of energy in the atmosphere from [Trenberth, 2009] (on the left) and the vertical temperature profile of the layers of the atmosphere (on the right).

In [Stensurd, 2007], the initial models used for numerical weather prediction were simplified versions of the complete equations of motion and were applied over relatively small portions of the globe. In 1949, Charney, Fjörtoft, and von Neumann produced the first one-day weather forecast using a one-layer barotropic model [Charney, 1950]. The state-of-the-art general circulation models and mesoscale models used today came into being because of improvements that occurred over the past 60 years. The improvements can be categorized as improved numerical techniques, model resolutions, and model physical process parameterization schemes. In addition to model improvements, there were significant advances in data assimilation techniques [Kalnay, 2003]. A further description of the recent evolution of the atmospheric general circulation models is presented in [Randall, 2000]. General and regional (or mesoscale) models are developed under resolutions that refer to the horizontal and vertical grid size, related to scales that can be resolved or reproduced by the numerical scheme formulations. Note that some physical processes and scales of motion cannot be represented regardless of the resolution. Parameterization is a numerical scheme formulation by which the important physical processes that cannot be resolved directly are represented in the corresponding model and grid resolution.

2.2 Mesoscale models

[Markowski, 2010] The adjective “synoptic” is defined in the American Meteorological Society’s Glossary of Meteorology as referring to meteorological data that are obtained simultaneously over a wide area in order to present a nearly instantaneous snapshot of the state of the atmosphere. The term “synoptic” though not initially intended to define scale, ultimately came to be used to describe the scale of large-scale weather systems, which were the only types of meteorological phenomena that could be resolved regularly by the coarse resolution observing platforms of the mid-19th century. The term “mesoscale” was introduced by [Ligda, 1951] in an article reviewing the use of weather radar observation. The author concluded that radar would provide useful information concerning the structure and behavior of the portion of the atmosphere not covered by either micro or synoptic meteorological studies. Phenomena of this size might well be designated as “mesometeorological” to describe phenomena smaller than the synoptic scale but larger than “microscale” [Orlanski, 1975] and [Fujita, 1981] define the range of mesoscale phenomena.

As per [AMS glossary, 2017], mesoscale phenomena range from a few to several hundred km, and include thunderstorms, squall lines, fronts, precipitation bands in tropical and extratropical cyclones, and topographically generated weather systems such as mountain waves and sea and land breezes.

From a dynamical perspective, this term pertains to processes with timescales ranging from the inverse of the Brunt–Väisälä frequency $N^2 = (g/\Theta_V \frac{\partial \Theta_V}{\partial z})$ (with Θ_V virtual potential temperature) to a pendulum day. Then synoptic-scale phenomena, which have a characteristic Rossby number $R_O = \frac{V}{Lf}$ less than 1, where R_O is a dimensionless number relating the ratio of inertial to Coriolis forces for a given flow of a rotating fluid, V is the velocity scale, f is the Coriolis parameter, and L is the horizontal length scale. Figure 2.3 presents the relationship between the spatial and temporal scales for mesoscale models.

Mesoscale phenomena can either be entirely topographically forced or driven by any one or a combination of the wide variety of instabilities that operate on the mesoscale, such as thermal, symmetric, and barotropic insta-

bility. The dominant instability on a given day depends on the local state of the atmosphere on that day.

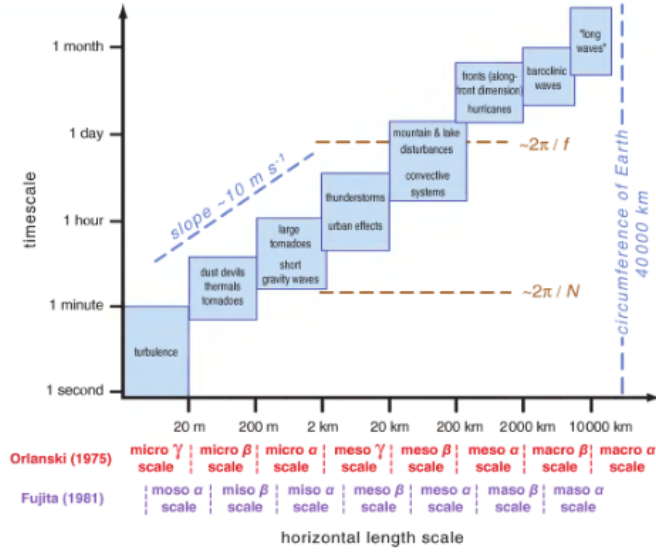


Figure 2.3: Time and length scale in mesoscale models from [Markowski, 2010]

2.3 Basic equations in mesoscale models

According to [Pielke, 2013], mesoscale atmospheric numerical models the conservation principles must be satisfied simultaneously in the numerical discretization and individual expressions, are as follows:

- i) Conservation of mass
- ii) Conservation of heat
- iii) Conservation of quantity of motion
- iv) Conservation of water
- v) Conservation of other gaseous and aerosol materials

The constitutive equation is also included.

Taking into account the need to present balances considering the turbulence, it is described the mean velocity component $\bar{V} = (\bar{u}, \bar{v}, \bar{w})$, potential temperature $\bar{\theta}$, and fluctuant component $V' = (u', v', w')$, θ' with $V = \bar{V} + V'$ of the turbulent regime, $\theta = \bar{\theta} + \theta'$, the system of equations for the conservation principles will be presented.

The conservation of mass i) Eq. 2.1, the conservation of heat (with S_θ the entropy) ii) Eq. 2.2, the conservation of quantity of motion iii) Eq. 2.3 wheres is included the viscous, and turbulent component $T = T_V + T_T$; $T_V = -pI - 2\mu D$ Eq. 2.4 (tensor notation).

$$\frac{\partial \rho}{\partial t} + \nabla \rho V = 0 \quad (2.1)$$

$$\frac{\partial \theta}{\partial t} + \nabla \theta V = S_\theta \quad (2.2)$$

$$\nabla T + \rho \vec{F} = \rho \frac{d\vec{V}}{dt} \quad (2.3)$$

$$T_T = -\rho \begin{pmatrix} \overline{u'u'} & \overline{u'v'} & \overline{u'w'} \\ \overline{v'u'} & \overline{v'v'} & \overline{v'w'} \\ \overline{w'u'} & \overline{w'v'} & \overline{w'w'} \end{pmatrix} \quad (2.4)$$

Consider the vertical balance of quantity of motion in Eq. 2.5:

$$\frac{\partial w}{\partial t} = -g - \frac{1}{\rho} \frac{\partial p}{\partial z} + \nu \frac{\partial^2 w}{\partial x_j^2} \quad (2.5)$$

Consider the turbulent flux $\rho = \bar{\rho} + \rho'$, $w = \bar{w} + w'$ y $p = \bar{p} + p'$, with the decomposition of the mean and fluctuation.

$$(\bar{\rho} + \rho') \frac{\partial(\bar{w} + w')}{\partial t} = -(\bar{\rho} + \rho')g - \frac{\partial(\bar{p} + p')}{\partial z} + \nu \frac{\partial^2(\bar{w} + w')}{\partial^2 x_j} \quad (2.6)$$

Dividing by $\bar{\rho}$, from Eq. 2.6, we obtain Eq. 2.7:

$$\left(1 + \frac{\rho'}{\bar{\rho}}\right) \frac{\partial(\bar{w} + w')}{\partial t} = -\frac{\rho'}{\bar{\rho}}g - \frac{1}{\bar{\rho}} \frac{\partial p'}{\partial z} + \nu \frac{\partial^2(\bar{w} + w')}{\partial^2 x_j} - \frac{1}{\bar{\rho}} \left[\frac{\partial \bar{p}}{\partial z} + \bar{\rho}g \right] \quad (2.7)$$

Assuming hydrostatic equilibrium $\frac{\partial \bar{p}}{\partial z} = -\bar{\rho}g$, and $\frac{\rho'}{\bar{\rho}} \approx 3.33 \times 10^{-3}$, $(1 + \frac{\rho'}{\bar{\rho}}) \approx 1$ is used to obtain Eq. 2.8 (As per the Boussinesq hypothesis, density variation is considered only in the vertical component):

$$\frac{\partial(\bar{w} + w')}{\partial t} = -\frac{\rho'}{\bar{\rho}}g - \frac{1}{\bar{\rho}} \frac{\partial p'}{\partial z} + \nu \frac{\partial^2(\bar{w} + w')}{\partial^2 x_j} \quad (2.8)$$

Then, considering the mean vertical component \bar{w} as depreciable (the measurements show it varies from 0 to 0.1 m/s, and the fluctuations w' can vary from 0 to 5 m/s), $\bar{w} \approx 0$ can be obtained from Eq. (2.9) as follows:

$$\frac{\partial(w')}{\partial t} = -\frac{\rho'}{\bar{\rho}}g - \frac{1}{\bar{\rho}} \frac{\partial p'}{\partial z} + \nu \frac{\partial^2(w')}{\partial^2 x_j} \quad (2.9)$$

Considering the variations in density associated with the variations in potential virtual temperature, Eq. 2.10 is obtained.

$$\frac{\partial(w')}{\partial t} = -\frac{\Theta'_v}{\Theta_v}g - \frac{1}{\bar{\rho}} \frac{\partial p'}{\partial z} + \nu \frac{\partial^2(w')}{\partial^2 x_j} \quad (2.10)$$

Then, the conservation of water (principle iv) is shown in Eq. 2.11, with q_n as the ratios of solid, liquid, and water vapor (n=1,2,3) and S_q as the deposition term.

$$\frac{\partial q_n}{\partial t} + \nabla q_n V = S_{q_n} \quad (2.11)$$

Then, the conservation of the quantity of gaseous species (principle v) Eq. 2.12 can be presented with χ_m as the aerosol species and S_{χ_m} as the deposition term.

$$\frac{\partial \chi_m}{\partial t} + \nabla \chi_m V = S_{\chi_m} \quad (2.12)$$

Finally, the constitutive law of gases (Eq. 2.13) with virtual temperature T_v , density ρ , and pressure P is given as

$$\frac{\bar{P}}{R} = \bar{\rho} \bar{T}_v \quad (2.13)$$

2.4 Physics parameterizations

In atmospheric models, the numerical techniques [Stensurd, 2007] are used to bring the equations of motion forward in time. The numerical techniques use different strategies to represent the original continuous equations with a finite data set that can be stored on a computer, and to compute the derivatives. The basic approaches used are grid point and finite-element methods. Model resolution refers to the size of the horizontal and vertical scales resolved or reproduced by the numerical model. Due to restrictive computational costs, the atmosphere cannot be perfectly represented by a numerical model, and is instead approximated by a finite data set. Parameterization is the process by which the most relevant physical processes that cannot be resolved directly by a numerical model are represented in a numerical scheme.

In figure 2.4 taken from [Randall, 2000], the process (parameterization) interactions that occur in current, state-of-the-art, general circulation models

are the same for mesoscale models; in this case, the hydrological processes are static information.

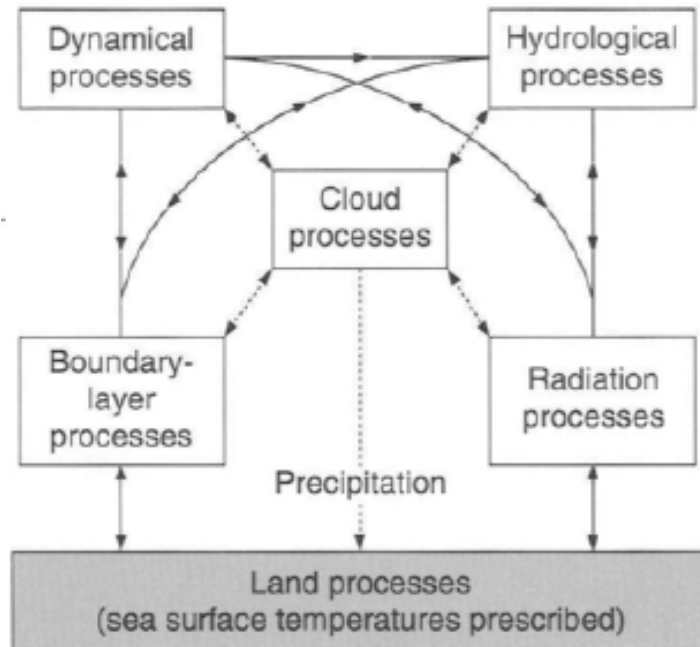


Figure 2.4: Processes included in typical general circulation models [Randall, 2000]

Parameterizations focus on the effects of the subgrid physical processes within the vertical column of each individual grid cell in the model. The vertical orientation of parameterization schemes is chosen since many of the physical processes naturally rearrange energy in this direction. Parameterizations represent subgrid physical processes for which the model has no direct information, and schemes must relate the subgrid processes to known model variables.

2.4.1 Microphysics of clouds

Clouds are extremely relevant in numerical simulations of the atmosphere [Cotton, 1989], as the presence of clouds is associated with unstable conditions and factors that produce such conditions. The mesoscale can, for the most part, be considered the environment of the cloud scale. In particular,

gusts in the presence of clouds could be associated with a gust event and a storm. The latent heat released in clouds serves as the “engine” that drives global atmospheric circulation, and when this phenomenon develops, gusty conditions are possible. Clouds are also a major factor in determining the Earth’s radiation budget as they reflect incoming solar radiation and absorb upwelling terrestrial radiation. Variations in the coverage and heights of clouds, and even the number and sizes of individual cloud particles, all have large effects on the Earth’s radiation budget. Microphysics refers to the dynamics of droplet size distribution, water ice formation and size, and the development of clouds. Microphysics schemes are numerical schemes that reproduce the evolution of clouds. They offer better representations using the known physics and statistical information on clouds, enabling the development of the microstructure. Microphysical processes can alter the macroscale dynamics and thermodynamic structure of clouds. However, in some cases, the physics is not sufficiently well known or is too complex to have its essence fully captured in simple formulations.

2.4.2 Cloud Parameterization and Cloud-Resolving Models

Once the microphysics of clouds is formulated in a parameterization, two basic strategies may be applied. These are called cloud parameterizations when the formation of clouds did not use the information in the horizontal grid resolution. They can be termed as cloud-resolving models (CRMs) when the horizontal grid size information of the equation of transport explicitly solves for the heat and water vertical transport used to study the presence of a cloud.

According to [Khairoutdinov, 2005], with the exception of microphysics, which is still highly parameterized, unlike parameterizations, CRMs use the first-principle approach to model cloud dynamics. Several case studies have demonstrated that CRM results are better than models that use parameterizations [Randall, 2003]. In terms of the relationship between the horizontal grid resolutions, CRMs are implemented for grid domains with resolutions of 4 km and higher resolution (horizontal grid cell less than 4 km).

2.4.3 Radiation

Radiation is the driver of atmospheric circulations; it passes through the atmosphere and reaches the Earth's surface in amounts that are unequally distributed in space and time. This unequal energy distribution, due in part to the Earth's spherical shape, produces horizontal temperature gradients that produce atmospheric motions. Radiation parameterizations provide a fast and accurate method of determining the total radiative flux at any given location. The interaction of radiation and clouds determines the stability in the PBL. The most important process responsible for energy transfer in the atmosphere is electromagnetic radiation. Electromagnetic radiation travels in waves, and all electromagnetic waves travel at the speed of light [Liou, 2002].

Scattering is a physical process by which a particle in the path of an electromagnetic wave continuously abstracts energy from the incident wave and reradiates that energy in all directions. In the atmosphere, the particles responsible for scattering range in size from gas molecules ($10 - 4\mu m$) to aerosols ($\sim 1\mu m$), water droplets ($10\mu m$), ice crystals ($100\mu m$), and large raindrops and hail ($1cm$).

The absorption of energy by particles and molecules leads to emission. The concept of emission is associated with blackbody radiation.

The Earth's surface also emits radiation in short electromagnetic waves, depending on the temperature of the skin. Figure 2.5 presents a scheme of radiation processes that are included under radiation parameterizations.

2.4.4 Land surface

Heat exchange with the land surface determines the evolution of the skin surface temperature of the terrain T_{sk} , which is governed by the energy balance at the surface as shown in Eq. 2.14 [Stensurd, 2007].

$$C_g \frac{\partial T_{sk}}{\partial t} = R_n - F_h - F_q - F_s \quad (2.14)$$

where C_g is the thermal capacity of the soil slab, R_n is the net radiative flux at the surface, F_h is the sensible heat flux into the surface layer of the

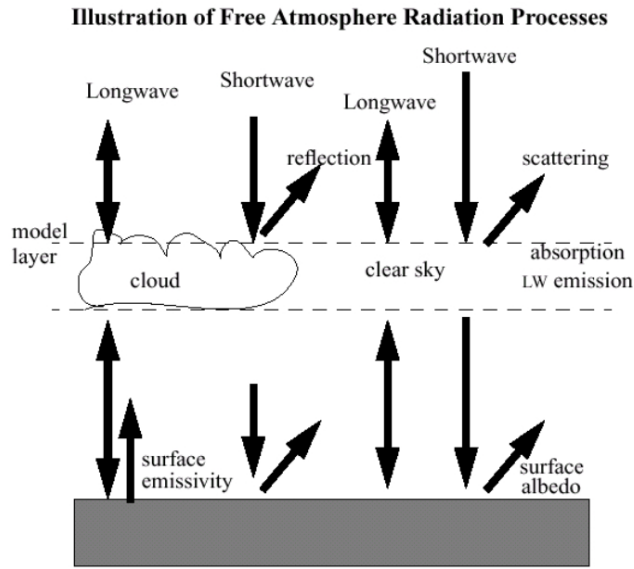


Figure 2.5: Scheme of the radiation processes included under radiation parameterizations

atmosphere, F_q is the latent heat flux, and F_s is the heat flux into the substrate. The first three terms of the right hand represent diurnal atmospheric forcings on the ground surface temperature, while F_s tends to restore T_{sk} toward a slow-varying deep soil temperature.

2.4.5 Planetary boundary Layer (PBL)

The PBL is the region of the atmosphere most relevant to the present work, as heat, mass, and quantity of motion exchanges between the atmosphere and the land or ocean surface occur in this region. The next chapter describes the conceptual approach and numerical formulation for the PBL.

2.4.6 Physics interactions between parameterizations

The physics categories (parameterizations) in WRF mesoscale models [Skamarock, 2008] are microphysics (MP), cumulus parameterization (CU), surface physics (Sfc), radiation (Ra), and PBL. The model's physics parameterizations are categorized in a modular way (related to the physics of the code scheme), and there are many interactions between them via the model state variables (such

as potential temperature, moisture, and wind velocity) and their tendencies, and via the surface fluxes. Table 2.1 presents the input and output states and surfaces fluxes in each parametrization scheme in the WRF model.

		Rad	MP	CP	PBL	Sfc
Atmospheric State or Tendencies	Momentum			i	io	
	Pot. Temp.	io	io	io	io	
	Water Vapor	i	io	io	io	
	Cloud	i	io	o	io	
	Precip	i	io	o		
Surface Fluxes	Longwave Up	i				o
	Longwave Down	o				i
	Shortwave Up	i				o
	Shortwave Down	o				i
	Sfc Convective Rain			o		i
	Sfc Resolved Rain		o			i
	Heat Flux				i	o
	Moisture Flux				i	o
Surface Stress				i	o	

Table 2.1: Physics Interactions. Columns correspond to model physical processes: radiation (Rad), microphysics (MP), cumulus parameterization (CP), planetary boundary layer/vertical diffusion (PBL), and surface physics (Sfc). Rows correspond to model variables, where i and o indicate whether a variable is an input or an output (updated) by a physical process. [Skamarock, 2008]

It should be noted that in these parameterization categories in the WRF model, the SL (the lowest level of the PBL) includes the surface physics model as well as the land surface (Sfc) model. The surface fluxes are determinants in the full mesoscale simulation; in the present work, these are particularly relevant, considering that the focus of the analysis is on gusts over the first 100 m (AGL) in height. The surface fluxes are determinants in establishing the stability regime.

2.5 Limit between mesoscale and large-eddy simulation models

Another relevant point of view in atmospheric numerical models is the ability to compute the scales inside the physical process. For PBL physical processes, [Wyngaard, 2004] identifies two broad classes of such modeling: mesoscale modeling for the larger domains, and large-eddy simulation (LES) for the smaller ones. They are fundamentally different with respect to the value of l/Δ , ratio of the energy-containing turbulence scale, and scale of the spatial filter used in the equations of motion.

[Peña, 2010] presented the results of an analysis of simultaneous sonic anemometer observations of wind speed and velocity spectra over a flat and homogeneous terrain from 10–160 m performed at the National Test Station for Wind Turbines at Høvsøre, Denmark. The study presents a relationship between the mixing length l , derived from the wind speed profile, and the length scale of turbulence, derived from the peak of the vertical velocity spectrum. The results of this analysis demonstrate a close connection between these two types of length scales. The length scale of turbulence, taken in this context as the peak of the spectrum of the wind velocity components in the energy-containing range, has also been observed to be proportional to height, at least in the SL. The computed mixing length varies from 10–80 m l at a height of 100 m. In the mesoscale numerical simulation applications used today, such as the WRF model, grid domain sizes range from 100-3000 m Δ .

In traditional mesoscale modeling, l/Δ is small, and thus, none of the turbulence is resolved. However, in traditional LES, it is large, and thus, the energy- and flux-containing turbulence is resolved. Figure 2.6 presents the concept in a turbulence spectrum representation of a flux in the PBL. This work analyzed specific horizontal grid resolutions within the limits of mesoscale model application.

[Wyngaard, 2004] described the region grid size of simulations between LES and mesoscale models as “terra incognita” or “gray zone”.

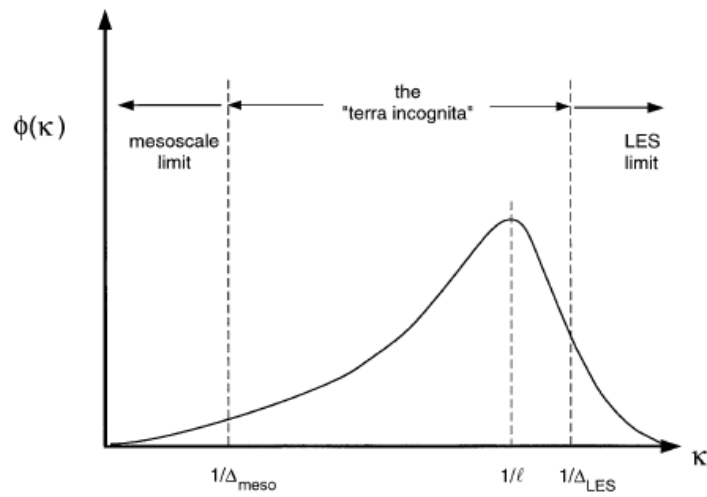


Figure 2.6: A schematic of the turbulence spectrum in the horizontal plane as a function of the horizontal wavenumber magnitude [Wyngaard, 2004]

Chapter 3

Planetary Boundary Layer (PBL)

The earth's surface is a boundary along the atmospheric domain. Transport processes at this boundary modify the lowest layer (within 100–3,000 m) of the atmosphere, creating what is called the boundary layer. The remainder of the air is free atmosphere, as seen in figure 3.1.

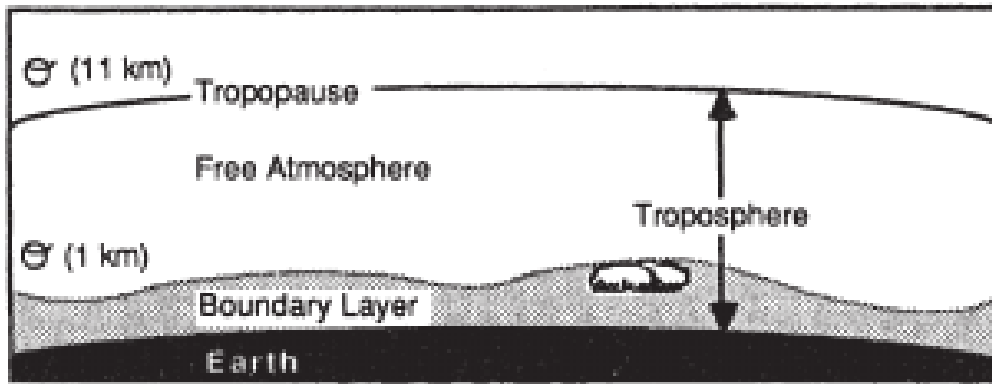


Figure 3.1: The troposphere can be divided into two parts: a boundary layer (shaded) near the surface and the free atmosphere above it. [Stull, 1988]

As per [Stull, 1988], the troposphere extends from the ground up to an average altitude of 11 km, but often only the lowest few kilometers are directly modified by the underlying surface. PBL is the part of the troposphere that is directly influenced by the Earth's surface and responds to surface forcings within about an hour or less. These forcings include frictional drag, evaporation and transpiration, heat transfer, pollutant emissions, and terrain-induced flow modifications. The thickness of the boundary layer is quite variable in time and space, ranging from hundreds of meters to a few kilometers. In the mesoscale numerical model, PBL parameterization uses different approaches to compute the PBL height, the most common being a computed critical flux Richardson number and the minimum value of total kinetic energy at that height.

In figure 3.2, the PBL is presented in an illustration with a temporal line on the horizontal axis; the evolution of the region of atmosphere is limited by the SL, the residual layer (RL) during stable conditions on top, and the region defined as the CML after sunrise. The CML of the atmosphere grows in height throughout the morning, reaching a height of 1–2 km by mid-afternoon.

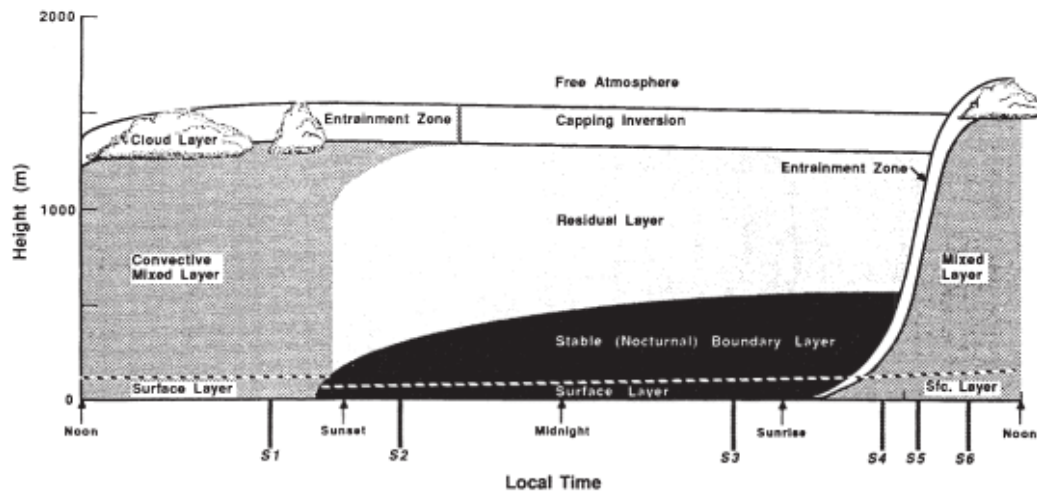


Figure 3.2: Residual Layer and convective mixed layer: evolution over time [Stull, 1988]

The PBL height is used to describe the CML and the stable nocturnal boundary layer. In numerical mesoscale models, PBL height could be computed as a few meters under stable conditions, reaching up to several kilometers in the case of CML. The turbulence in the stable nocturnal PBL is produced by the mean wind shear. It is destroyed by the buoyancy effects and (at a greater rate) by viscous dissipation [Wyngaard, 1985].

The diurnal cycle of solar radiation is the most relevant factor in determining the heat exchange between the land and atmosphere, and thus, in determining the vertical stability. The heat exchange with the land determines the evolution of the skin surface temperature parameter, which has a determining incidence in the vertical wind profile. To show the diurnal changes in PBL related to the zone of interest, velocities up to 100 m are plotted during a 10 min interval for the Colonia Eulacio tower during a summer and winter day (presented in figures 3.3 and 3.4, respectively) [de Almeida, Gutierrez, 2015]. The figures show the evolution with time of the principal variables that describe the daily cycle related to sunset and sundown. In the top row of the plot, the mean velocity near the surface atmosphere is shown in a continuous line, and the transparent area shows the standard deviation of the velocity. Each color represents a height: 101.8 m (blue), 81.8 m (red), 60.8 m (green), 25.7 m (black), and 10.1 m (magenta). The plot in the middle row is the vertical temperature gradient $\frac{\partial T}{\partial z}$ measured at 100.8 m and 3.4 m. The radiation measured on the horizontal plane is plotted in the bottom row.

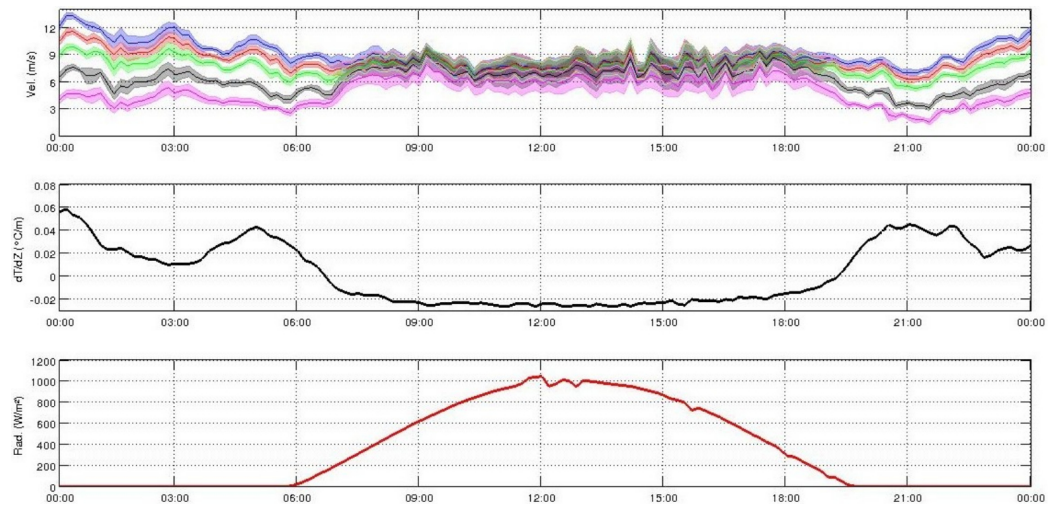


Figure 3.3: Plot of observational data taken at the Colonia Eulacio tower on December 6, 2014. From [de Almeida, Gutierrez, 2015]

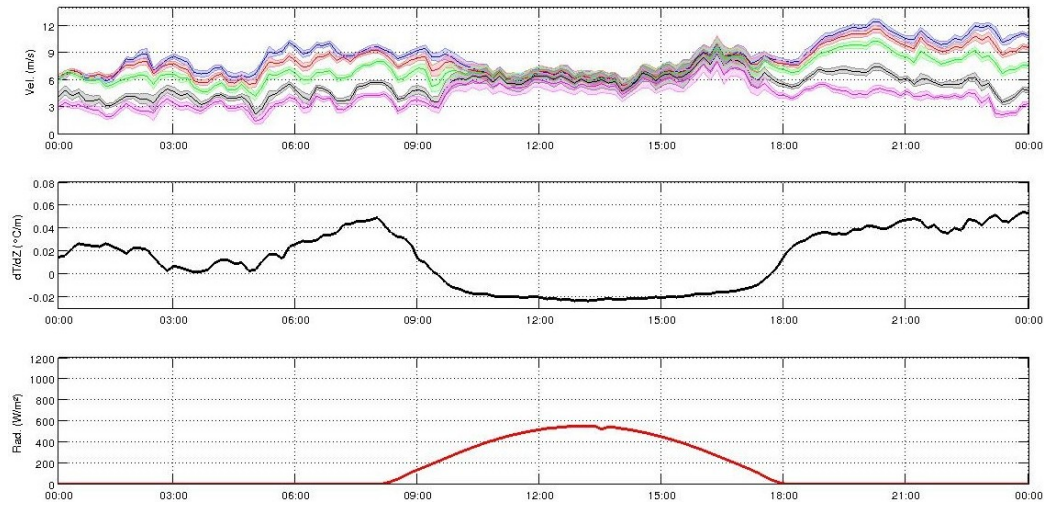


Figure 3.4: Plot of observational data taken at the Colonia Eulacio tower on July 15, 2015. From [de Almeida, Gutierrez, 2015]

To show the incidence of solar irradiance by season in the lower region of the PBL, the analysis with one year's worth of data (2012) measured at the Colonia Rubio (CR) tower (Lat 31.238 Long 57.465), with a pyranometer (Li-Cor LI-200SZ, NRG Systems), is presented. Computations were conducted in terms of hourly average for the mean, standard deviation, and maximum value. Figure 3.5 shows the diurnal cycle of solar irradiance W/m^2 divided by season (summer, autumn, winter, and spring 2012), hourly mean value, and the 16th and 84th percentiles (vertical bars) [Gutierrez, 2015].

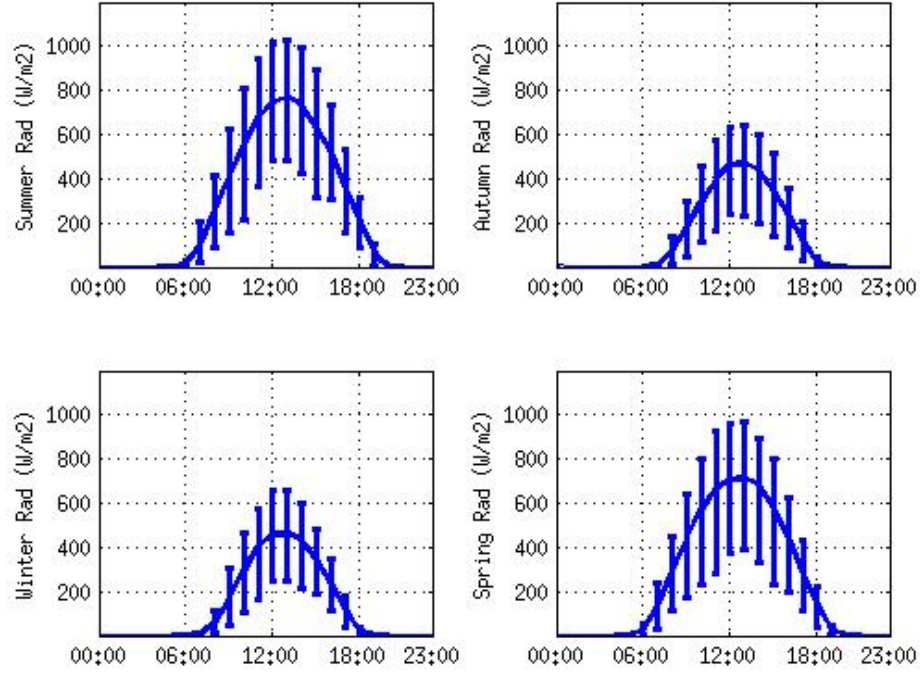


Figure 3.5: Diurnal cycle of solar irradiance W/m^2 using data recorded at the Colonia Rubio tower by season (summer, autumn, winter, and spring) in 2012; data shown are hourly mean value and 16th and 84th percentiles (vertical bars) and are sourced from [Gutierrez, 2015].

Data presented for the same year (2012) and tower (Colonia Rubio) in figure 3.6 include the shear $\frac{\partial V}{\partial z}$ (1/s) (vertical velocity gradient of the sweep of wind turbine blade heights) and are sourced from [Gutierrez, 2015]. $\frac{\partial V}{\partial z}$ is calculated from the measurements (1/s) made by cup anemometers (NRG Systems) at different heights between 60–80 m (blue) and 80–101 m (red), discriminated by season (summer, autumn, winter, and spring 2012). The continuous lines show the means and the vertical bars show the 16th and 84th percentiles.

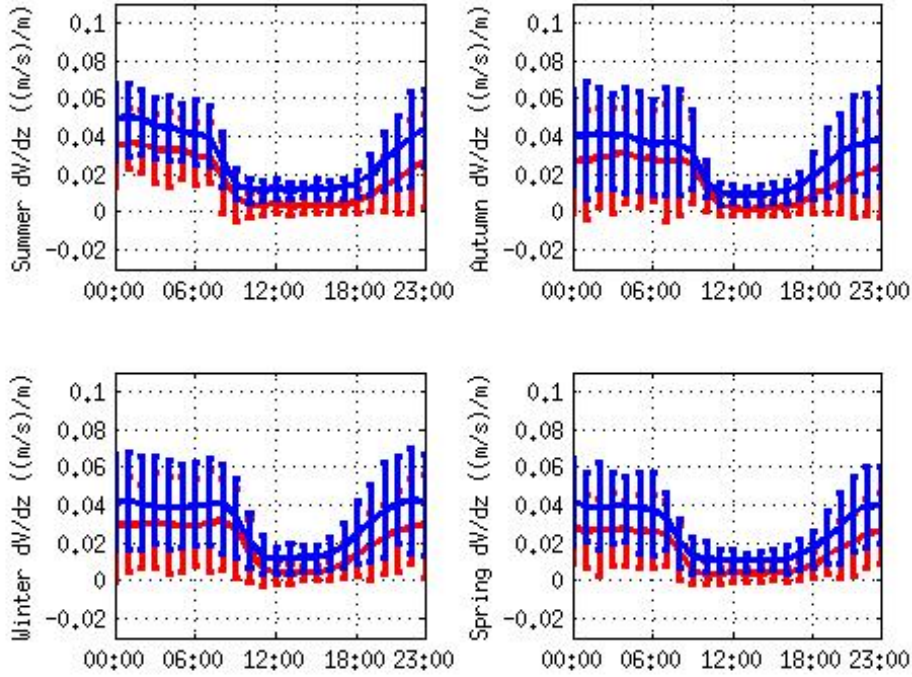


Figure 3.6: Diurnal cycle of the shear $\frac{\partial V}{\partial z}$ ($1/s$) between 60–80 m (blue) and 80–101 m (red), discriminated by season (summer, autumn, winter, and spring 2012), measured at the Colonia Rubio tower. Values shown are the hourly mean value and the 16th and 84th percentiles vertical bars [Gutierrez, 2015].

At night, at heights between 60–100 m, the velocity of the vertical gradient varies from $0\frac{1}{s}$ to $0.08\frac{1}{s}$. During the day it varies from $0\frac{1}{s}$ to $0.02\frac{1}{s}$. During the day, the lower levels of the atmosphere are heated by the skin surface temperature and the induced thermal vortex produces a more uniform vertical profile.

3.1 PBL Parametrizations

In general circulation models, the numerical formulation of the PBL is extremely relevant. The more general equation included in numerical models, such as the WRF model, is presented below in a summary of numerical for-

mulations that need to be solved.

With the simplifying assumption of horizontal homogeneity, ($\frac{\partial \bar{u}}{\partial x} = 0$ and $\frac{\partial \bar{v}}{\partial y} = 0$), and $w \approx 0$, the model's basic set of equations of quantity of motion can be derived using Equations 3.1 and 3.2.

The $U_g = -\frac{1}{f_c \bar{\rho}} \frac{\partial \bar{P}}{\partial y}$ and $V_g = \frac{1}{f_c \bar{\rho}} \frac{\partial \bar{P}}{\partial x}$ terms represent the components of the wind driven by the large-scale horizontal pressure gradient (so-called geostrophic wind). f_c is the Coriolis parameter.

$$\frac{\partial \bar{u}}{\partial t} = f_c(\bar{v} - V_g) - \frac{\partial(\overline{w'u'})}{\partial z} \quad (3.1)$$

$$\frac{\partial \bar{v}}{\partial t} = -f_c(\bar{u} - U_g) - \frac{\partial(\overline{v'w'})}{\partial z} \quad (3.2)$$

Then, the heat and water vapor q_v balance Equations 3.23 and 3.4:

$$\frac{\partial \bar{\theta}}{\partial t} = -\frac{\partial(\overline{w'\theta'})}{\partial z} \quad (3.3)$$

$$\frac{\partial \bar{q}_v}{\partial t} = -\frac{\partial(\overline{w'q'_v})}{\partial z} \quad (3.4)$$

With regard to turbulence closure, it is problematic to relate the turbulent fluxes to the mean (resolved) state of the atmosphere. Following the assumption of horizontal homogeneity, only the vertical component in Eqs. 3.5, 3.6, and 3.7 remains:

$$\overline{w'u'} = -K_m \frac{\partial \bar{u}}{\partial z} \quad (3.5)$$

$$\overline{w'v'} = -K_m \frac{\partial \bar{v}}{\partial z} \quad (3.6)$$

$$\overline{w'\theta'} = -K_H \frac{\partial \bar{\theta}}{\partial z} \quad (3.7)$$

where K_m and K_H are eddy diffusivity coefficients. Numerous formulations for eddy diffusivity have been proposed, forming the basis of various boundary layer parameterization schemes used in operational and research mesoscale models.

3.2 Atmospheric surface layer

The lowest atmospheric cap is the surface layer (SL). In this region, the wind shear is the determinant in the configuration of the vertical structure of the speed field and temperature. The principal physical magnitudes in the SL are height z , surface stress τ_0 , heat exchange with the surface Q_0 , and temperature T .

The coupling between the ground surface and the atmosphere occurs through fluxes between the surface and the lowest model level SL. The numerical scheme includes different formulations for surface fluxes based on [Monin, 1954], [Businger, 1971], and [Pleim, 2007a], [Pleim, 2007b] [Nakanishi 2001].

SL schemes define a velocity scale. Here, the friction velocity, u_* , is defined (Eq. 3.8), and its magnitude is related to the vertical flux of the horizontal momentum measured near the surface, considering the following terms of the Reynolds tensor (as in Eq. 2.3) $\tau_{xz} = -\overline{\rho u'w'}$ and $\tau_{yz} = -\overline{\rho v'w'}$.

$$u_*^2 = [\tau_{xz}^2 + \tau_{yz}^2]^{1/2} = [\overline{\rho u'w'^2} + \overline{\rho v'w'^2}]^{1/2} \quad (3.8)$$

The surface layer temperature scale

$$\theta_*^{SL} = \frac{-\overline{w'\theta'_S}}{u_*} \quad (3.9)$$

and the humidity scale

$$q_*^{SL} = \frac{-\overline{w'q'_S}}{u_*} \quad (3.10)$$

are also introduced. Based on mixing length theory [Prandtl, 1925], it is possible to propose a length scale related to the description of turbulence. Considering a mean wind direction co-linear with \bar{u} , a turbulent eddy, and upward movement by z' towards some reference level z , it might be possible to determine a vertical velocity w' as shown below.

$$u' = -\frac{\partial \bar{u}}{\partial z} z' \quad (3.11)$$

$$w' = -c \left| \frac{\partial \bar{u}}{\partial z} \right| z' \quad (3.12)$$

This defines the mixing length l with $l^2 = cz'^2$. The most common assumption is $l = kz$ ($k = 0.40$, or the Von Karman constant determines the logarithmic wind vertical profile).

Then, the viscosity of a turbulent eddy (Eq. 3.13) can be computed as a function of the mixing length scale l and the shear $\left| \frac{\partial \bar{u}}{\partial z} \right|$:

$$K_m = l^2 \left| \frac{\partial \bar{u}}{\partial z} \right| \quad (3.13)$$

Another relevant magnitude in the description of the physics of the SL is the Obukhov length given by Eq. 3.14

$$L = \frac{-\bar{\theta}u_*^3}{kg(\overline{w'\theta'})} \quad (3.14)$$

One interpretation of the Obukhov length is that it is proportional to the height above the surface at which buoyant factors first dominate over mechanical (shear) production of turbulence. It is defined as a dimensionless parameter $\zeta = \frac{z}{L}$ that describes the stability regime (L) for a given height (z). ($\zeta > 0$ denotes stable, $\zeta < 0$ refers to unstable, and $\zeta = 0$ is determined to be neutral). Numerical SL schemes relate the stability regime (ζ) of dimensionless wind shear in Eq. 3.15 and the dimensionless temperature gradient in Eq. 3.21.

$$\phi_m(\zeta) = \frac{kz}{u_*} \frac{\partial \bar{u}}{\partial z} \quad (3.15)$$

$$\phi_h(\zeta) = \frac{z}{\theta_*} \frac{\partial \bar{\theta}}{\partial z} \quad (3.16)$$

Figures 3.7 and 3.8 present the results of [Businger, 1971] With regard to the dimensionless wind shear and temperature gradient.

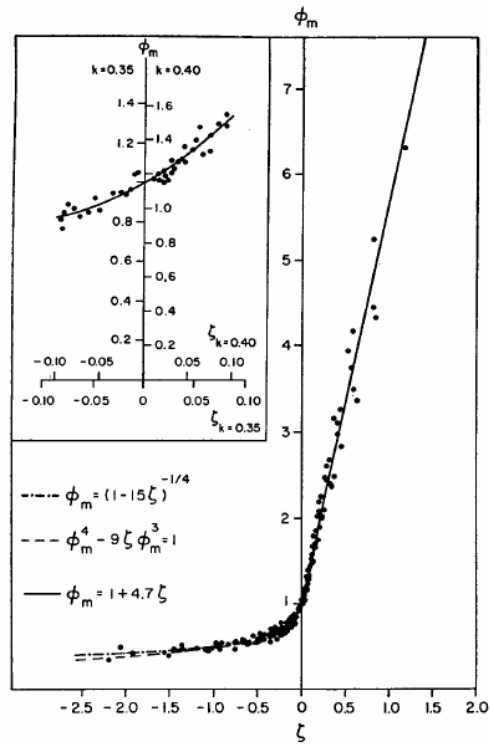


Figure 3.7: Dimensionless wind shear with the interpolation formula in the surface layer [Businger, 1971]

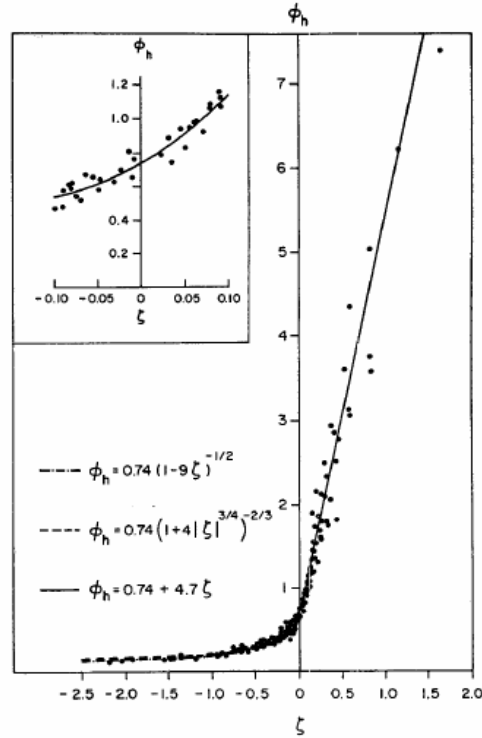


Figure 3.8: Dimensionless temperature gradient with the interpolation formula in the surface layer [Businger, 1971]

[Businger, 1971] is the most common approach used with regard to the numerical schemes of SL. In all the numerical schemes, the mixing length or dimensionless gradients are computed as a function of $\zeta = \frac{z}{L}$, for example, as in [Pleim, 2007a], [Pleim, 2007b], and [Nakanishi 2001]; in these cases, the eddy viscosity is computed independent of ζ .

[Nakanishi 2001] is an adaptation of [Mellor and Yamada, 1974] work on the PBL, and uses a different numerical formulation for the SL. The alternative formulation for the SL presents a proposed master length scale l that can be assimilated with the concept of the mixing length (in the present work, the same notation was used for the master length scale and mixing length (l)). The expression 3.17 presents the formulation for the master length scale in [Nakanishi 2001] and proposes the diagnostic equation for l , which consists of three length scales: l_S , l_T , and l_B .

$$\frac{1}{l} = \frac{1}{l_S} + \frac{1}{l_T} + \frac{1}{l_B} \quad (3.17)$$

In this expression, the shortest scale of the three (l_S , l_T , l_B) could control l .

l_S , computed by the expression 3.2 and independent of the stability regime, is denoted as the length scale in the SL.

$$l_S = \begin{cases} kz/3.7 & \zeta \geq 1 \\ kz(1 + \alpha_0\zeta)^{-1} & 0 \geq \zeta > -1 \\ kz(1 - \alpha_4\zeta)^{0.2} & \zeta < -1 \end{cases} \quad (3.18)$$

Following [Mellor and Yamada, 1974], who built on the work done by [Blackadar, 1957], l_T is the length scale depending on the turbulent structure of the PBL, and q is the mean square component of fluctuation velocity related to the turbulent kinetic energy (TKE) $e = (u'^2 + v'^2 + w'^2)/2$ as $e = q^2/2$.

$$l_T = \alpha_1 \frac{\int_0^\infty qz dz}{\int_0^\infty q dz} \quad (3.19)$$

l_B is the length scale limited by the buoyancy effect, as in Eq. 3.2, where $q_c = [(g/\theta)(w'\theta')]^{1/3}$ is a vertical velocity scale.

$$(3.20) \quad l_B = \begin{cases} \alpha_2 q / N, & \frac{\partial \bar{\theta}}{\partial z} > 0, \quad \zeta \geq 0 \\ [\alpha_2 q + \alpha_3 q (\frac{q_c}{l_T N})^{1/2}] / N, & \frac{\partial \bar{\theta}}{\partial z} > 0, \quad \zeta < 0 \\ \infty, & \frac{\partial \bar{\theta}}{\partial z} \geq 0, \end{cases}$$

α_0 , α_1 , α_2 , α_3 , and α_4 are parameters of the parameterization. The original values from [Nakanishi 2001] were $\alpha_0 = 2.7$, $\alpha_1 = 0.23$, $\alpha_2 = 1$, $\alpha_3 = 5$, and $\alpha_4 = 100$. A new version of the PBL scheme in the WRF model has the seated parameters $\alpha_0 = 2.1$, $\alpha_2 = 0.6$, and $\alpha_4 = 20$.

3.3 Parameterizations and local closure order

In mesoscale models, approaches to the numerical schemes of the PBL are developed using different strategies for computing the vertical structure of turbulence. The height h of the PBL is a relevant parameter. To compute it, the two most common methodologies relate to the height at which the TKE becomes lower than an arbitrary small value or when a critical Richardson number is reached. The diurnal cycle of the PBL height computed by numerical schemes and seasons is presented in the Appendix.

3.3.1 First-order closure

In the first-order closure, the conservation of mass (i), conservation of heat (ii), conservation of quantity of motion (iii), conservation of water (iv), and conservation of other gaseous and aerosol materials (v), are considered as described in section 2.

The first-order closure means that the turbulent fluxes $\overline{u'w'}$, $\overline{v'w'}$, and $\overline{\Theta'w'}$ are parameterized. This closure approximation is often called gradi-

ent transport theory or K-theory. K_m and K_H (turbulent viscosity or eddy viscosity coefficients) are described in terms of a formulation. The reference works for the K-theory formulation are [Wyngaard, 1983], and [Troen, Marth 1986], where h is the height of the PBL:

$$K_m = u_* k z \phi_m^{-1} \left(1 - \frac{z}{h}\right)^p \quad (3.21)$$

This formulation is consistent with the SL similarity theory for heights relatively lower than the PBL height $z \ll h$.

Figure 3.9 presents the typical variation of K_m with height, from [Stull, 1988].

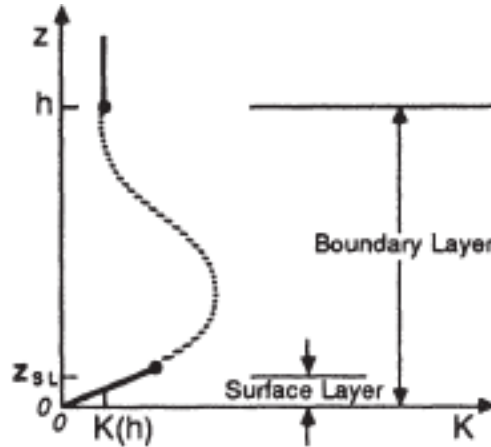


Figure 3.9: Typical variation of K_m with height. Taken from [Stull, 1988]

3.3.2 One-and-a-half-order closure

In the case of the local closure of one-and-a-half orders, one-order closure of the turbulent kinetic energy balance is added. The kinetic energy balance is obtained by multiplying the fluctuation of velocity V' , balancing the quantity of motion of the turbulent flux, averaging in time, and obtaining the balance of turbulent energy in Eq. 3.22, where the total kinetic energy $e = (u'^2 + v'^2 + w'^2)/2$ (TKE) and ε is the dissipation of turbulence [Stull, 1988].

$$\frac{\partial \bar{e}}{\partial t} = -\overline{u'w'} \frac{\partial \bar{u}}{\partial z} - \overline{v'w'} \frac{\partial \bar{v}}{\partial z} + \left(\frac{g}{\bar{\theta}}\right) \overline{w'\theta'} - \frac{\partial[\overline{w'}((p'/\rho) + e)]}{\partial z} - \varepsilon \quad (3.22)$$

The heat balance equation is multiplied by θ' and integrates Eq. 3.23, with ε_θ and ε_R as dissipation components.

$$\frac{\partial(\overline{\theta'^2})}{\partial t} = -2\overline{w'\theta'} \frac{\partial \bar{\theta}}{\partial z} - \frac{\partial \overline{w'\theta'^2}}{\partial z} - 2\varepsilon_\theta - \varepsilon_R \quad (3.23)$$

The unknowns fluxes are $\overline{u'w'}$, $\overline{v'w'}$, $\overline{w'\theta'}$, and $\overline{w'\rho'}/\bar{\rho}$; components of third moments $\overline{w'e}$ and $\overline{w'\theta'^2}$, and dissipation ε , ε_θ and ε_R .

The TKE and temperature variance give a measure of the intensity of turbulence. These variables are used in the parameterization of the eddy turbulence diffusivity $K_m(\bar{e}, \bar{\theta}'^2)$, as shown in Eqs. 3.24, 3.25, 3.26, 3.27, 3.28, 3.29, 3.30, and 3.32.

$$\overline{w'u'} = -K_m(\bar{e}, \bar{\theta}'^2) \frac{\partial \bar{u}}{\partial z} \quad (3.24)$$

$$\overline{w'v'} = -K_m(\bar{e}, \bar{\theta}'^2) \frac{\partial \bar{v}}{\partial z} \quad (3.25)$$

$$\overline{w'\theta'} = -K_H(\bar{e}, \bar{\theta}'^2) \frac{\partial \bar{\theta}}{\partial z} - \gamma_c(\bar{e}, \bar{\theta}'^2) \quad (3.26)$$

Next, the formulation of the one-and-a-half-order closure based on [Mellor and Yamada, 1974] is presented, where Λ_1 , Λ_2 , Λ_3 , and Λ_4 (scales), γ_c (correction to the local gradient), and S_m (stability correction function) are parameters of the numerical scheme.

$$\frac{\partial[\overline{w'}((p'/\rho) + e)]}{\partial z} = \frac{5}{3}\Lambda_4 e^{-1/2} \frac{\partial \bar{e}}{\partial z} \quad (3.27)$$

$$\overline{w'\theta'^2} = \Lambda_3 e^{-1/2} \frac{\partial \bar{\theta}'^2}{\partial z} \quad (3.28)$$

$$\varepsilon_R = 0 \quad (3.29)$$

$$\varepsilon = \frac{e^{-3/2}}{\Lambda_1} \quad (3.30)$$

$$\varepsilon_\theta = \frac{e^{-1/2} \bar{\theta}'^2}{\Lambda_2} \quad (3.31)$$

Then the turbulent viscosity K_m is computed using the mixing length l , a function of the stability regime S_m , and the TKE e :

$$K_m = l S_m (e)^{1/2} \quad (3.32)$$

Independent of numerical schemes of the PBL, different methodologies for computing the turbulent viscosity as function of e , and stability regime S_m , are proposed.

Chapter 4

Wind Gusts: observational data

Wind gusts are measured as the maximum wind speed observed over a fixed period. With a focus on developing a gust parameterization, we analyzed observational data recorded by the UTE to assess wind energy resources. The UTE installed a set of towers with anemometers, wind vanes, pyranometers, and thermometers throughout Uruguay, which is dominated by rolling plains and low mountain ranges. Wind energy towers are located in three geographical regions. The first region is close to the La Plata River, including an estuary composed of seawater and freshwater from the Parana River, one of the world's longest; its main tributary, the Paraguay River; and the Uruguay River. The second region is close to the Atlantic Ocean, and the third region is further inland, at least 300 km from the La Plata River and the Atlantic Ocean.

The towers are equipped with anemometers with orthogonal azimuth angles to each height, to filter the effect of the tower wake. The installation was performed following the recommendations of the IEC standard 61400-12 [IEC.61400-12, 1998]. Figure 4 presents the configuration of the anemometers and wind vane at 98 m. The wind measurements were performed with cup anemometers (NRG 40, NRG Systems) and wind vanes (NRG 200P, NRG Systems) at various heights including approximately 100 m, where the turbines are mounted. Care was taken to determine and remove the tower wake effect.

Figure 4.2 shows the locations of the towers Colonia Eulacio (CE), Rosendo Mendoza (RM), Jose Ignacio (JI), and Aparicio Saravia (AS), and the to-

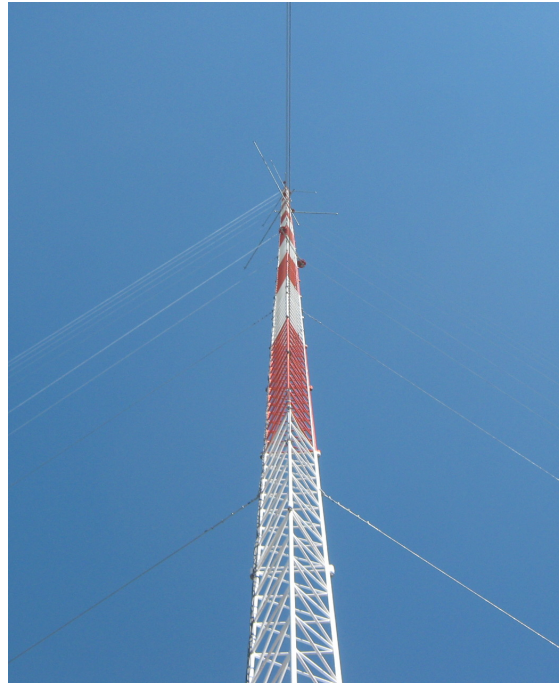


Figure 4.1: Instruments with orthogonal azimuths on top of the Colonia Eulacio (CE) tower

pography in m. Altitudes in the study region are below 500 m.

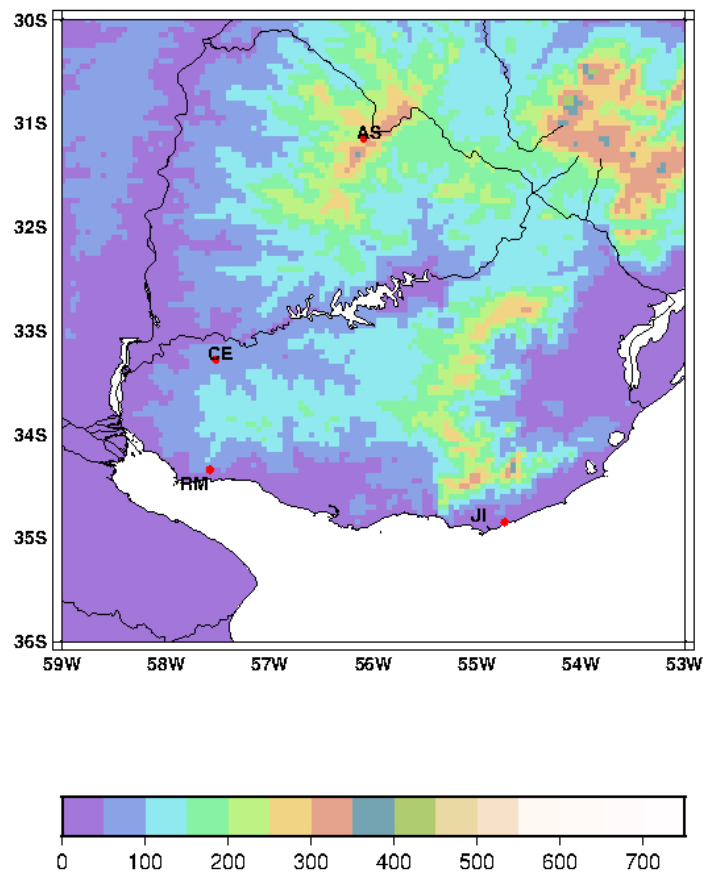


Figure 4.2: Locations and topography (m) of towers from where observational data was measured

The land use for each tower location is representative of rural areas in figure 4.3, which shows photographs captured from different directions near the location of the CE tower.

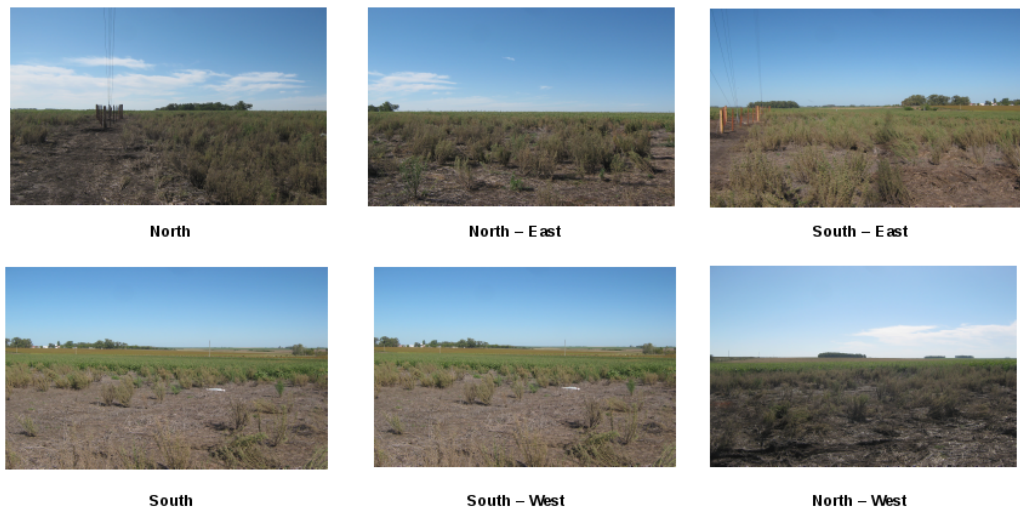


Figure 4.3: Photographs taken from different directions near the location of the Colonia Eulacio tower.

Table 4.1 presents the measurements considered in this work. The time periods and tower locations selections are related to the quality of continuous data available.

	Lat South	Long West	Height in tower of top wind velocity measurement analyzed (m)	Height in tower of bottom wind velocity measurement analyzed (m)	Height of bottom temperature measurement in tower (m)	Height of top temperature measurement in tower (m)	Period of time data observation considered in the analysis
AS	31.143	56.095	101	-----	5	99	1 Jan 2012 to 31 Dec 2012
CE	33.28	57.522	101.8	10.1	3.4	100.8	8 Aug 2014 to 7 Aug 2015
JI	34.85	54.735	98	12	12	98	1 Jan 2012 to 31 Dec 2012
RM	34.343	57.578	101	-----	2	100	1 Jan 2012 to 31 Dec 2012 and 8 Aug 2014 to 7 Aug 2015

Table 4.1: Tower locations, height of measurement considered, and period of analysis

To determine the diurnal cycle, the mean and maximum values were computed for 1 h intervals based on 10 min data. Gusts were determined from 2 s samples.

4.1 Analysis of wind gust observational data

The analysis of the observational data in this section begins with a description of the mean diurnal cycle and seasonal variations of gust relative to the stability regime. First, the analysis focuses on the means and amplitudes of the variations considering the 16th and 84th percentiles. Then a more detailed analysis is given for extreme gust events, where the goal was to identify dimensional and nondimensional parameters that could be helpful in the development of a wind gust numerical parameterization model.

To analyze the variations in different seasons of the year in terms of the diurnal cycle, the 10 min data were processed to obtain the mean and maximum hourly values of each variable in each season. The analysis is presented by season: winter, autumn, spring, and summer. The plot shows the dates of the season, for example, winter is June 21 to September 20, because significant changes occur in solar radiation during the year at 30 and 35S latitude.

The temperature gradient, which describes atmospheric stability [Arya, 1998] if it is computed in the lowest cap of the atmosphere, can be associated with heat exchange between Earth's surface and the atmosphere.

The temperature gradient presented in this work covers heights from 2–12 m to 98–101.8 m AGL, depending on the location of the tower.

When the temperature gradient is used as an indicator of stability, a

higher positive value indicates a strongly stable regime. A superadiabatic temperature gradient indicates a strongly unstable regime with an adiabatic temperature lapse rate $\Gamma = -g/c_p$, with $c_p \simeq 1005 \frac{J}{C^\circ.kg}$ of $\Gamma = -0.0098C^\circ/m$. At the 100 m nearest the ground, there is no significant change in hydrostatic pressure with height; thus, the potential temperature can be assumed to be similar to measured temperature in towers.

Figure 4.4 shows the diurnal cycle for observations of the vertical temperature gradient $\frac{\partial T}{\partial z}$, made in 2012 and discriminated by season, at the RM tower, where temperatures were measured at 100 m and 2 m; the AS tower, where temperatures were measured at 99 m and 5 m; and the JI tower, where temperatures were measured at 98 m and 12 m (the horizontal green line on the plot marks the dry adiabatic lapse rate $\Gamma = -0.0098C^\circ/m$). After sunrise, regimes with a superadiabatic temperature gradient were frequently observed. A study of hourly measurements of ΔT taken from a tower between 2–32 m high, located in a primarily rural area, found 2,828 superadiabatic periods over six years [Talke, 1983]. Another study observed surface-based superadiabatic and autoconvective layers and concluded that the former can be long-lived in the daytime [Czarnetzki, 2012].

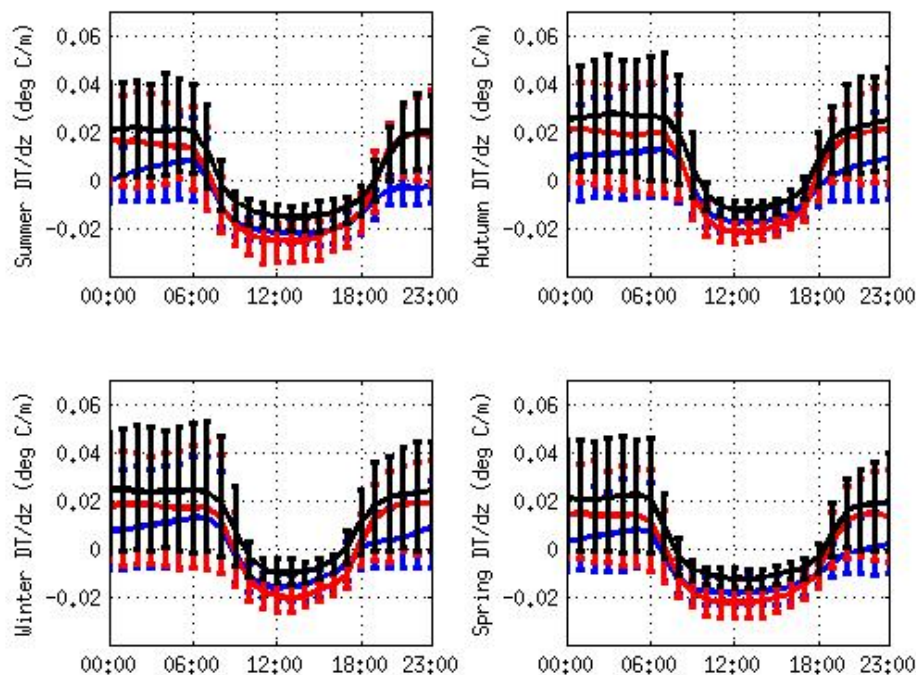


Figure 4.4: Diurnal variation in the gradient of temperature at the Aparicio Saravia (AS) tower (red; temperatures measured at 99 m and 5 m), the Jose Ignacio (JI) tower (blue; temperatures measured at 98 m and 12 m), and the Rosendo Mendoza (RM) tower (black; temperatures measured at 100 m and 2 m, (C°/m)). Vertical bars show 16th and 84th percentiles, and the horizontal green line marks the dry adiabatic lapse rate $\Gamma = -0.0098C^\circ/m$.

The vertical temperature gradient $\frac{\partial T}{\partial z}$ is a parameter that clearly shows different patterns of stability regimes for different mesoscale conditions related to the geographical location of the observation tower. The description of a mesoscale regime with $\frac{\partial T}{\partial z}$ is also applied in noncomplex regions, where each tower giving the analyzed observational data is no longer located in close proximity to the others but has a different geographical condition, such as proximity to ocean or estuary, or a more continental location.

A negative vertical temperature gradient means that the surface of the terrain is heating the near atmosphere, implying thermal turbulence production and mixing. This occurs after sunrise. To examine how this condition

affects the mean values of wind gusts, we present this information for the same tower locations and study period in figure 4.5, which also plots the gust factor GF in Eq. 4.1 as the ratio of gust g divided by mean velocity \bar{V} . The figure shows the diurnal cycle of the gust factor GF discriminated by season at the AS, JI, and RM towers, which were 101 m, 98 m, and 101 m high, respectively. The hourly data for analysis of the diurnal gust cycle and the hourly maximum wind speed were also recorded; the data logger had a sampling frequency of 0.5 Hz.

$$GF = g/\bar{V}. \quad (4.1)$$

This plot demonstrates that the GF is indeed higher when the near-surface layer is strongly unstable $\frac{\partial T}{\partial z} < 0$. During the night, when there were positive vertical gradients of temperature $\frac{\partial T}{\partial z} > 0$ (stable condition), it is observed that GFs were smaller.

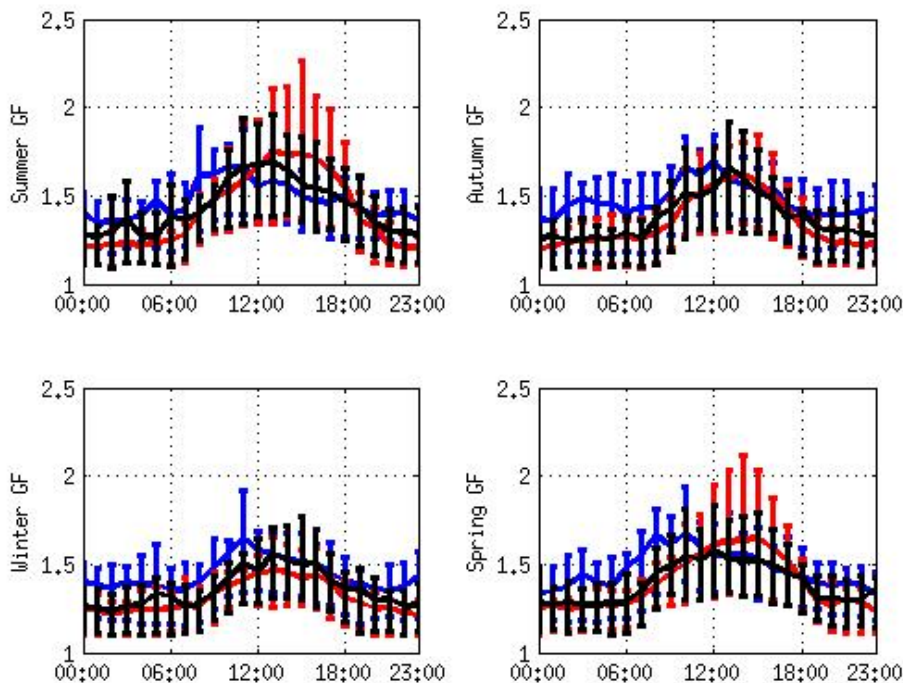


Figure 4.5: Diurnal variations in the gust factor at Aparicio Saravia (AS) tower (red; 101 m), Jose Ignacio (JI) tower (blue; 98 m) and Rosendo Mendoza (RM) tower (black; 101 m). Vertical bars show the mean and 16th and 84th percentiles.

In contrast, strong stability was observed at night at tower locations far from the ocean. At night the sea breeze mixes the air at different level at JI also, which is a mesoscale pattern in the diurnal cycle that clearly differs from those recorded at the other tower locations. The mean values of solar radiation for the analyzed region [Abal, 2011] shows that the east coast closer to the ocean receives less radiation during the day, which is related to the higher incidence of cloud cover. If the cloudiness persists into the night, the cloud cover implies less stability in JI than at AS or RM. The La Plata River (RM) tower also shows more stability during the night.

During the day, the gust factor varied more in the seasons with more solar radiation potentially being available, which is reasonable because larger instabilities should enhance the TKE [Stull, 1988]. At AS, the most inland

tower, GF peaked in the mid-afternoon hours during the period in which the boundary layer was least stable, especially in summer (Figure 4.4). The day-to-day variability was also large because the site is well protected from the moderating influence of the ocean. The summertime peak occurred closer to local noon at RM, which was influenced by the nearby La Plata River. The variability at JI was suppressed at all hours in all seasons and tended to reach its maximum prior to local noon. This tower is close to the Atlantic coastline and is significantly affected by sea breeze.

The seasonal daily cycle of GF in the 16th and 84th percentiles show the incidences of a stable regime under average (mean) wind conditions.

Regarding the historical observation data used in this work, the relevant tower measurements from some of the towers were provided by UTE. These data can be used to compute the vertical temperature gradient and horizontal velocity. In this section, towers with temperature measurements in two vertical levels and horizontal wind velocity measurement obtained at 10–12 m and 98–101 m, respectively, are considered.

In this work, the local vertical stability regime in the lowest level (the first 100 m) of the PBL, was classified by computing the vertical gradient of temperature at each tower. This information was assessed directly from different temperature measurements.

The four stability classes are defined empirically as follows:

- Strongly stable when $0.01C^\circ/m \leq \frac{\partial T}{\partial z}$; green in the scatterplots
- Slightly stable when $0C^\circ/m \leq \frac{\partial T}{\partial z} < 0.01C^\circ/m$; blue in the scatterplots
- Proximity to adiabatic lapse rate (near neutral condition) when $-0.01C^\circ/m \leq \frac{\partial T}{\partial z} < 0C^\circ/m$; magenta in the scatterplots
- Unstable superadiabatic when $\frac{\partial T}{\partial z} < -0.01C^\circ/m$; red in the scatterplots

Figures 4.6, 4.7, 4.8, 4.9, and 4.10 show plots for each tower, representative of the different mesoscale regimes of AS, RM and JI, and each previously

defined stability class. Scatterplots in the left-hand column show GF versus mean velocity (m/s) at the highest levels measured in a tower, and those in the right-hand column shows gust versus mean velocity (m/s). Colors represent the stability regimes defined previously.

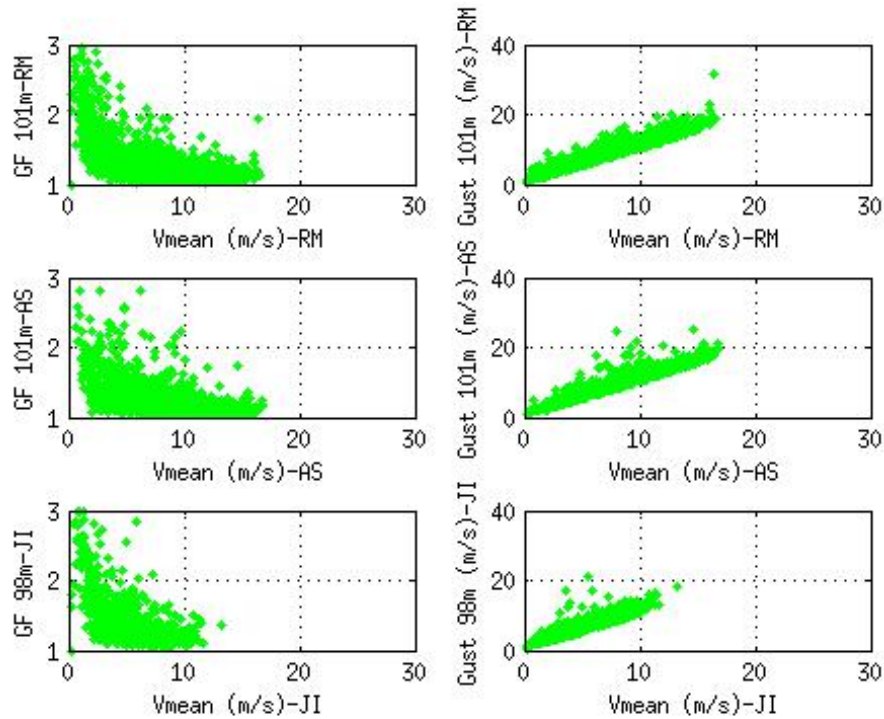


Figure 4.6: Left-hand column: gust factor versus mean velocity (strongly stable regime, i.e., when stable when $0.01C^\circ/m \leq \frac{\partial T}{\partial z}$; green), right-hand column: gust versus mean velocity (strongly stable regime) at Aparicio Saravia (AS; 101 m tall), Jose Ignacio (JI; 98 m tall), and Rosendo Mendoza (RM; 101 m tall).

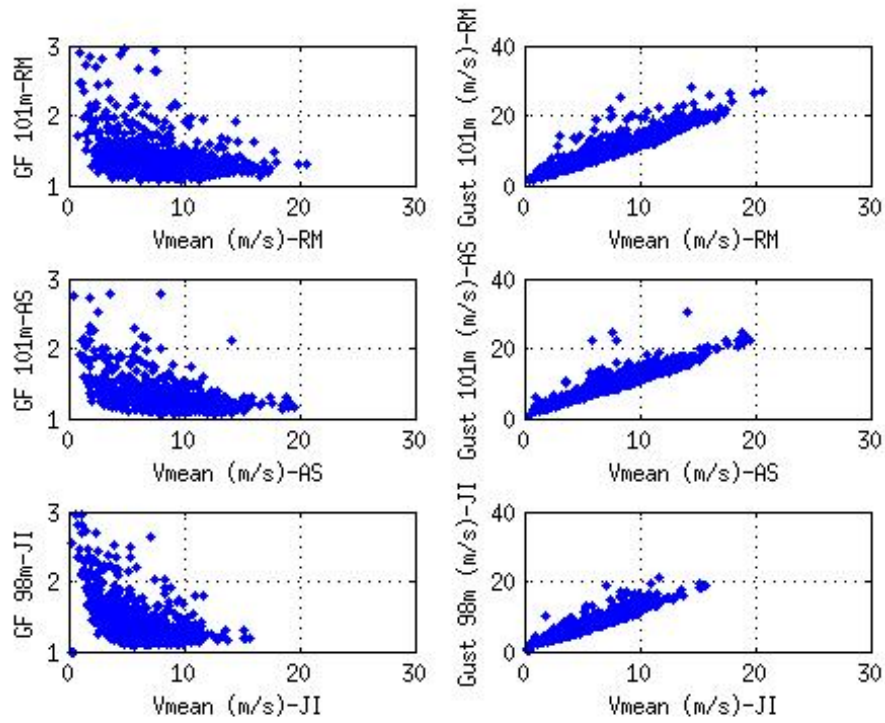


Figure 4.7: Left-hand column: gust factor versus mean velocity (slightly stable regime, i.e., when $0C^\circ/m \leq \frac{\partial T}{\partial z} < 0.01C^\circ/m$; blue), right-hand column: gust versus mean velocity (slightly stable regime) at Aparicio Saravia (AS; 101 m), Jose Ignacio (JI; 98 m), and Rosendo Mendoza (RM; 101 m).

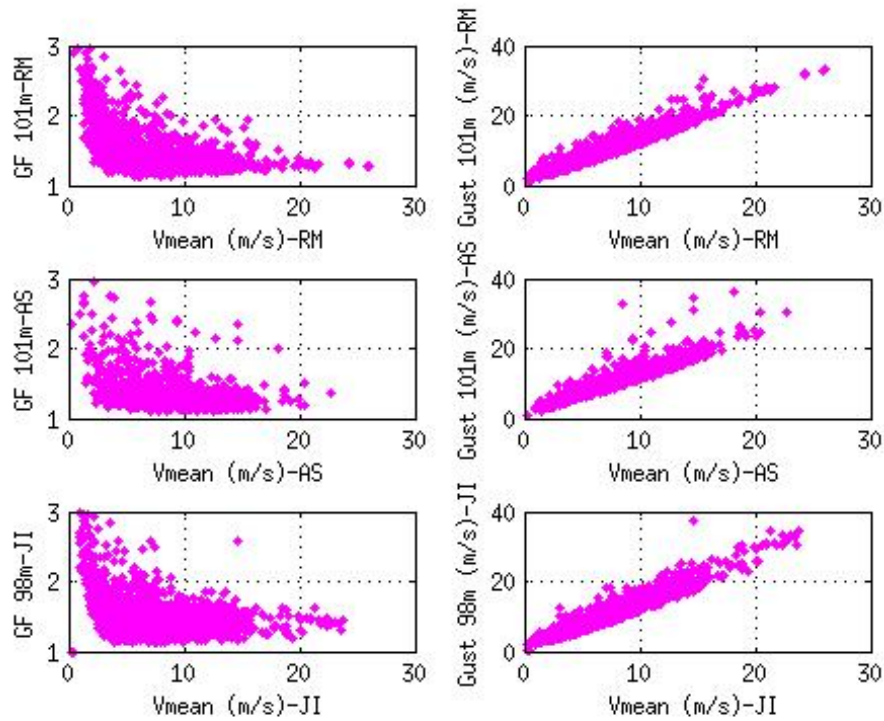


Figure 4.8: Left-hand column: gust factor versus mean velocity (proximity to adiabatic lapse rate (near neutral, i.e., when $-0.01C^\circ/m \leq \frac{\partial T}{\partial z} < 0C^\circ/m$; magenta)), right-hand column: gust versus mean velocity (proximity to adiabatic lapse rate (near neutral)) at Aparicio Saravia (AS; 101 m), Jose Ignacio (JI; 98 m), and Rosendo Mendoza (RM; 101 m).

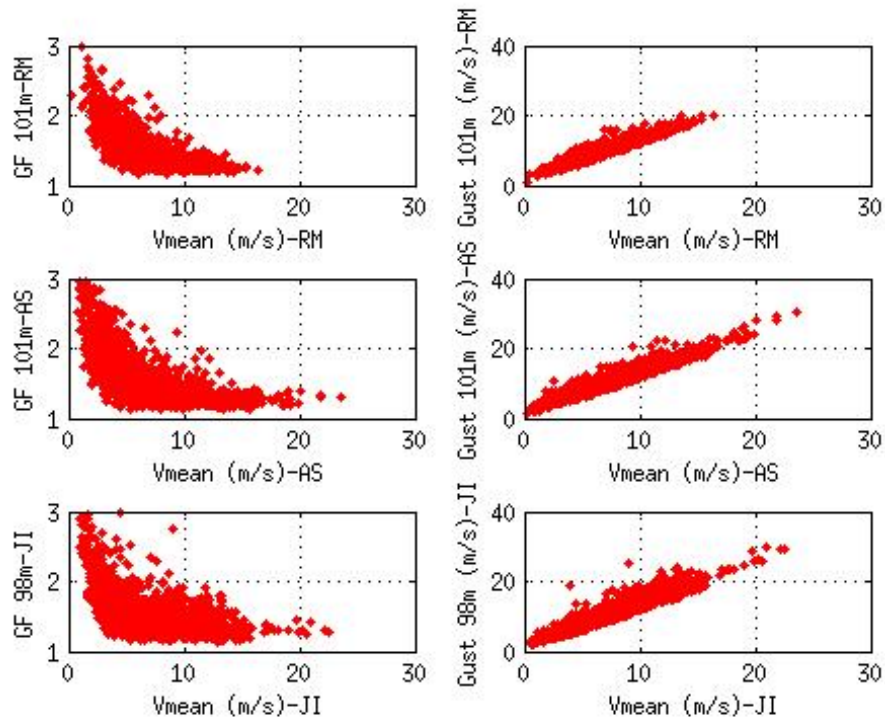


Figure 4.9: Left-hand column: gust factor versus mean velocity (unstable adiabatic conditions, i.e., when $\frac{\partial T}{\partial z} < -0.01C^\circ/m$; red), right-hand column: gust versus mean velocity (unstable adiabatic conditions) at Aparicio Saravia (AS; 101 m), Jose Ignacio (JI; 98 m), and Rosendo Mendoza (RM; 101 m).

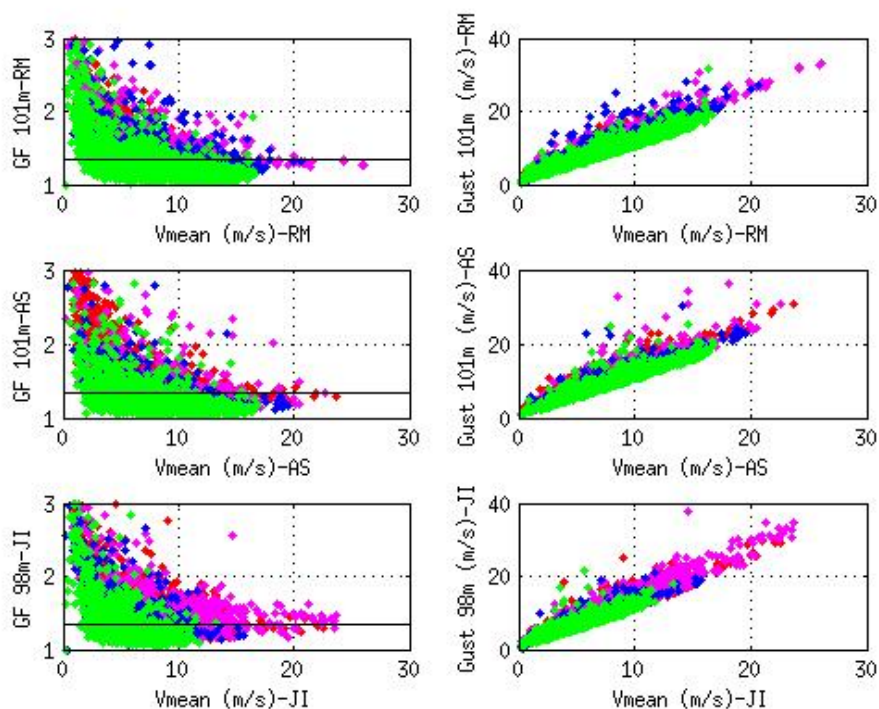


Figure 4.10: Left-hand column: gust factor versus mean velocity, right-hand column: gust versus mean velocity at Aparicio Saravia (AS; 101 m), Jose Ignacio (JI; 98 m), and Rosendo Mendoza (RM; 101 m). Scatterplot colors show all classes of stability regimes defined; the black line represents a GF asymptotic value of 1.33

The strongly stable conditions (green) show that when there are no significant cases with gusts stronger than $g > 15m/s$, the stratification of the atmosphere tends to stop the turbulence. The slightly stable conditions (blue) show more gusty cases than the strongly stable conditions and are also associated with higher mean wind velocity (higher shear), which produces mixing in the vertical profile. These cases, could be related to transitional conditions (from stable to unstable or from unstable to stable). The superadiabatic lapse rate in vertical temperature gradient (red in the scatterplots) creates buoyancy forces that produce vertical mixing which acts to reduce vertical shear, which in turn reduces gust. The gustiest cases occurred when the proximity to adiabatic lapse rate was near neutral condition (magenta in the

scatterplots). For all stability classes, the gust factor decreased when the mean velocity increased.

For higher values of mean velocity, the gust factor trended toward an asymptotic value of 1.33 (the line plotted in GF versus \bar{V}).

4.1.1 Extreme wind gust cases

To develop a numerical forecast model for wind gust, it is of interest to identify the parameters that can be useful in cases of extreme wind gust occurrence. The data are analyzed to identify changes in wind vertical profile and stability regime patterns during extreme wind gust events. At two towers, CE and JI, temperature measurements were taken at two vertical levels, 3–12 m and 98–101 m, respectively, and horizontal wind velocity measurements were taken at the top and bottom of the towers at 10–12 m and 98–101 m, respectively. The following analysis was conducted with data obtained during two different periods in which one year of information, including high-quality data in both cases, was available, as shown in Table 4.1.

We analyzed the changes in vertical temperature gradient patterns and vertical shear which was computed as the vertical gradient of horizontal velocity at the occurrence of the gusty wind event. The first row of figures 4.11 and 4.12 shows histogram plots of the vertical gradient of velocity $\frac{\partial V}{\partial z}$; the second row shows the vertical gradient of temperature $\frac{\partial T}{\partial z}$; and the left-hand column shows the frequency for all cases analyses over one year. The histograms in the middle column measure gusts greater than 15 m/s at the top level, and the right-hand column shows wind gusts greater than 20 m/s. These data are from the CE and JI towers. The red line shows the adiabatic lapse rate in the vertical temperature gradient.

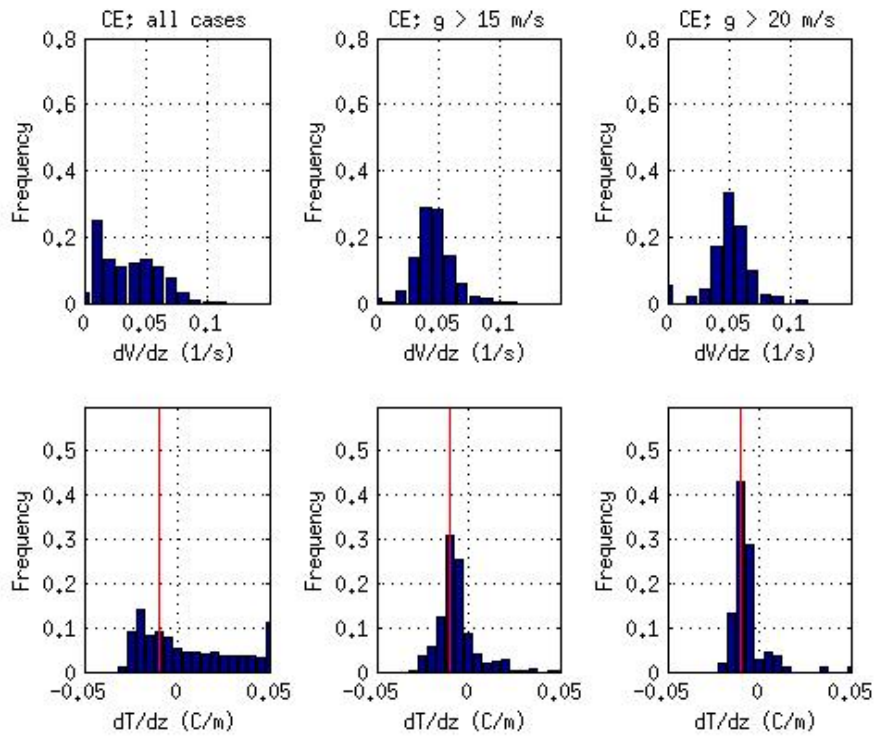


Figure 4.11: Data from the Colonia Eulacio (CE) tower including histograms $\frac{\partial V}{\partial z}$ of measurements taken from heights of 101.8 m and 10.1 m (in the first row). Histograms in the second row show the vertical temperature gradient $\frac{\partial T}{\partial z}$ measured at 100.8 m and 3.4 m. The left-hand column shows the relative frequencies of all cases analyzed in one year, the middle column shows the histogram of $g > 15$ m/s, and the right-hand column shows $g > 20$ m/s

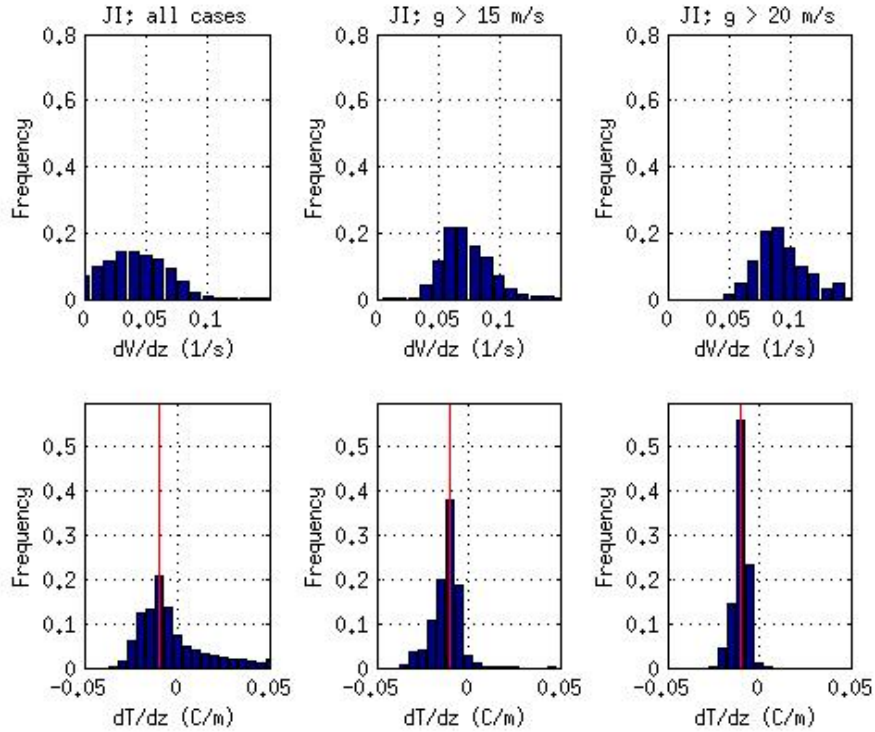


Figure 4.12: Data from the Jose Ignacio (JI) tower, including histograms of relative frequency $\frac{\partial V}{\partial z}$ measured at 98 m and 12 m. The second row shows the vertical temperature gradient $\frac{\partial T}{\partial z}$ measured at 98 m and 12 m. The left-hand column shows the relative frequencies of all cases analyzed in one year, the middle column shows the histogram $g > 15\text{m/s}$, and the right-hand column shows $g > 20\text{m/s}$

The vertical wind velocity profile $\frac{\partial V}{\partial z}$ is a measurement of shear. The histograms in the first row of figures 4.11 and 4.12 show the computed shear for all cases and the occurrence of extreme wind gust events ($g > 15\text{m/s}$ (the middle histograms) and $g > 20\text{m/s}$ (the right-hand histograms)). At the CE tower, when the wind gust was greater than 15 m/s at the anemometer placed at 101 m, the likely $\frac{\partial V}{\partial z}$ value was 0.05 (1/s). This tendency became evident when the frequencies of wind gusts greater than 20 m/s were plotted. At the JI tower, when the wind gust was greater than 15 m/s (i.e., when it was extreme) at the anemometer placed at 98 m; the likely $\frac{\partial V}{\partial z}$ value was between 0.05 and 0.10 (1/s). This tendency was accentuated when the wind

gust was greater than 20 m/s.

In figures 4.11 and 4.12, it can be seen that extreme wind gust events occur with a vertical temperature gradient $\frac{\partial T}{\partial z}$ near an adiabatic lapse rate. Analyses of the tendencies in the vertical gradient data measured at the CE and JI towers revealed a clear asymptotic vertical temperature gradient $\frac{\partial T}{\partial z}$. In the second row of figures 4.11 and 4.12, $\frac{\partial T}{\partial z}$ is computed when extreme wind gust events occurred. The red line in the figures ($\Gamma = -g/c_p = -0.0098C^\circ/m$) indicates that the extreme wind gust events occurred in an adiabatic atmosphere. When the samples analyzed are narrowed to large gust events (> 15 and > 20 m/s), it is observed that most commonly occurring situation is for neutral conditions in the surface layer, which was noted in [Pasquill 1961] and utilized in the definition of stability classes in atmosphere. As previously stated, wind gusts are produced by strongly vertical shears in unstable atmospheric conditions. These events occur when there is a strong interaction between mechanical forces (high shear) and thermal buoyancy mixing forces, which determines the adiabatic lapse rate.

[Businger, 1971] analyzed wind and temperature profiles for a wide range of stability conditions over a dry, flat, homogeneous surface in which the predominant process was the vertical transport of momentum and sensible heat. In this section, the focus is on an extreme wind gust event. It is of interest to identify the relationship between the buoyancy and mechanical (shear) forces measured at the top anemometer in extreme gust cases. The Richardson bulk number Ri with Θ_V is rigorously defined with the potential virtual temperature ($g_0 = 9.8m/s^2$) in Eq. 4.2.

$$Ri = \frac{g_0 \cdot \partial \Theta_V / \partial z}{\Theta_V \cdot (\partial V / \partial z)^2} \quad (4.2)$$

A simplified expression can be computed for the data from the CE and JI towers using the measured temperature T and horizontal velocity V at bottom and top of the towers using Eq. 4.3:

$$Ri = \frac{g_0 \cdot \partial T / \partial z}{T \cdot (\partial V / \partial z)^2} \quad (4.3)$$

Figure 4.13 presents a scatterplot of the observed gusts (g) versus the observed Ri in the CE and JI towers for the period described in Table 4.1,

that is, data for one year for each tower. This period is sufficient to evaluate different mesoscale events that could occur during the simulation of a numerical model.

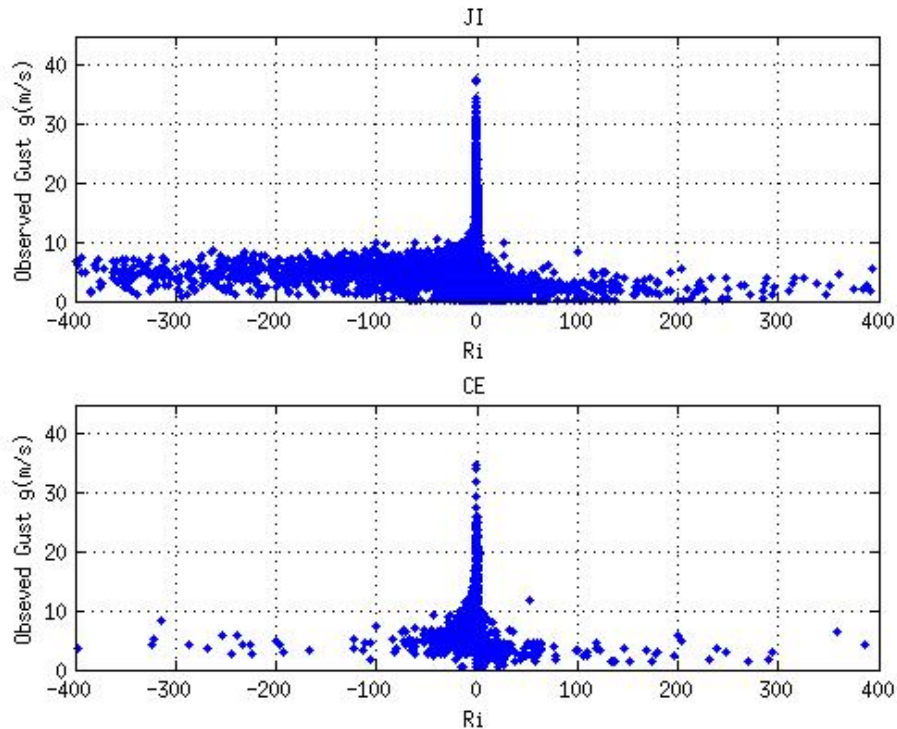


Figure 4.13: Scatterplot of Ri and gust g (m/s) in 2012 for the Jose Ignacio (JI) tower, and for August 8, 2014 to August 7, 2015 for the Colonia Eulacio (CE) tower

The observations from the CE and JI towers have different patterns in terms of the distribution of Ri vs g (observed Ri and gust), and as was shown previously in this section, the location of the JI tower has more neutral and unstable conditions because of the interaction of air over the continent and the ocean. JI has more unstable situations particularly at night (see figure 4.4), which means more mixing and less shear, and a more dispersed scatterplot (4.13). Larger gusts are still very closely associated with $Ri \sim 0$. Then in the scatterplot of the JI, data is more dispersed on the left side of $Ri < 0$ observation, and it can be seen that there are clear differences in the patterns of mesoscale wind regimes at both locations. The gusty cases

showed a characteristic negative critical bulk Richardson number close to zero (in first 100 m AGL), in both towers, for gusts higher than 15 m/s; the most frequent was that between $-0.2 < Ri < 0$. In figure 4.14, the histogram for CE and JI is plotted for observed gusts higher than 15 m/s.

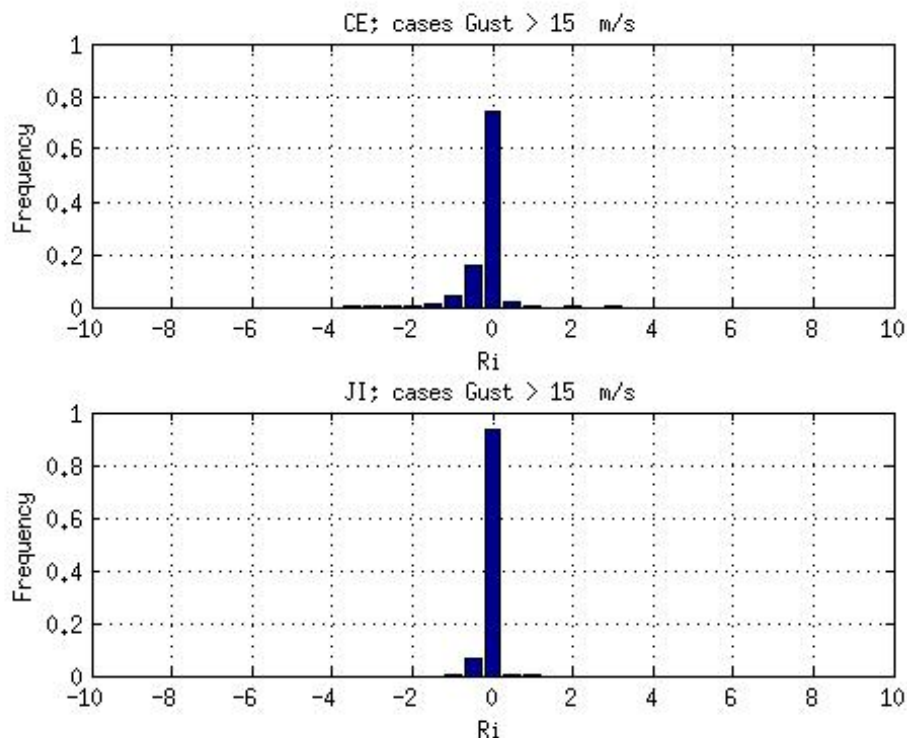


Figure 4.14: Histogram of Ri for cases when $g > 15m/s$ during 2012 for Jose Ignacio (JI) and from August 8, 2014 to August 7, 2015 for Colonia Eulacio (CE)

In this work, the type of mesoscale event that can produce extreme wind events is not characterized. The following section will analyze whether Ri can be a forecast parameter in WRF model simulations to develop a parameterization of gusts, comparing the vertical profiles and skills of different PBL schemes.

Chapter 5

Numerical model and methods

5.1 The Weather Research and Forecasting (WRF) model

The Weather Research and Forecasting (WRF) model is a numerical weather prediction and atmospheric simulation system designed for both research and operational applications. The WRF model is supported as a tool for both communities to promote closer ties between, and address the needs of, both. The Advanced Research WRF (ARW) supports horizontal nesting that allows resolution to be focused over a region of interest by introducing an additional grid into the simulation. The WRF physics options fall into several categories, each containing several choices. These are (1) micro-physics, (2) cumulus parameterization, (3) PBL, (4) land-surface model, and (5) radiation [Skamarock, 2008]. Each PBL parameterization has a surface layer approach that is included in the formulation. The present work will analyze the sensibility of the results independence of the PBL scheme, including different surface layer formulations inside the PBL parameterization.

5.2 Numerical model and methods

In this section, the physical schemes used in numerical running of the ARW core [Skamarock, 2008] are described. The WRF model uses a coordinate system with a staggered C grid [Arakawa, 1977]. The model was run with

telescoping grids with horizontal resolutions from 12 km–444 m, as shown in figure 5.1.

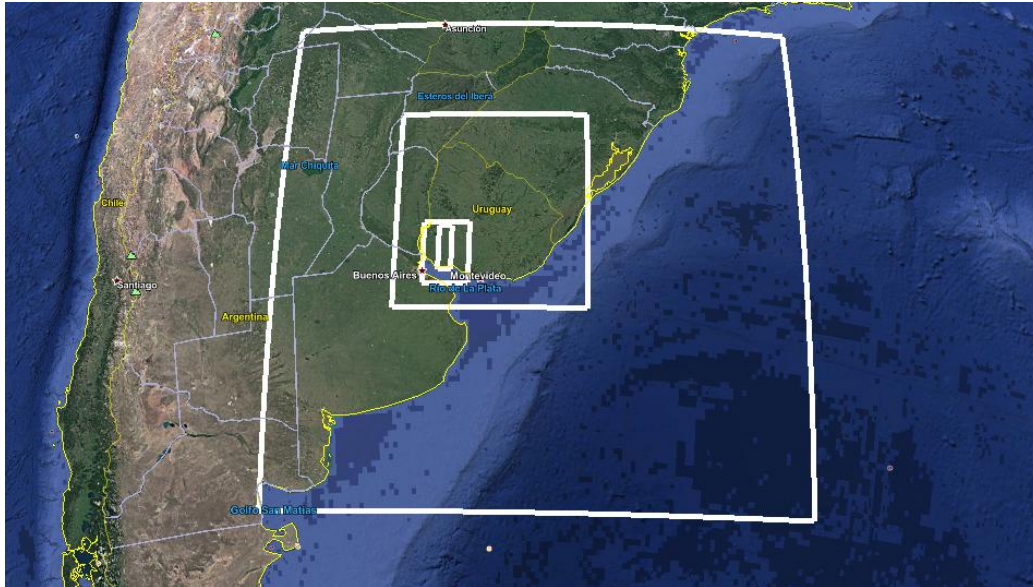


Figure 5.1: Telescoping Weather Research and Forecasting (WRF) domains with horizontal grids of 12 km, 4 km, 1.3 km, and 444 m

Centered on the La Plata River, the 12 km horizontal grid resolution domain covers a significant portion of South America, with a 4 km domain over all the tower locations, and 1.3 km and 444 m in the CE and RM towers. All simulations utilized 41 vertical layers with the model top at 5,000 Pa, the rapid radiative transfer model as the radiation scheme [Mlawe, 1997], Lin microphysics [Lin, 1983], and the Noah land surface model [Chen, 2001]. The Kain–Fritsch [Kain, 2004] cumulus parameterization (insert citation here) was employed in the 12 km domain. The National Centers for Environmental Prediction Global Forecast System operational global analyses were used for the initial and boundary conditions.

The model was run from the period August 8, 2014 to August 7, 2015, with a focus on comparing simulations with measurements available from wind cup anemometers up to 100 m AGL.

Sensitivity to the PBL was assessed with eight PBL schemes: YSU [Dudhia, 2006], MYJ [Mellor and Yamada, 1974], [Mellor and Yamada, 1982], ACM2 Pleim [Pleim, 2007a],

[Pleim, 2007b], Boulac [Bougeault and Lacarrere, 1989], Bretherton–Park [Bretherton and Park, 2009], GBM-TKE [Grenier, 2001], Shin–Hong [Shin and Hong, 2015] and MYNN 2.5 [Nakanishi 2001]. All PBL schemes were run with 4 km horizontal grid resolution, and the higher resolutions (1.3 km and 444 m), were run with Shin–Hong and MYJ.

In Table 5.1, the order closure, and the methodology for computing the height of PBL, are described for schemes included in the simulations in the present work. The PBL height computed, and the skill of mean wind velocity of the PBL schemes running in this work, are presented in the Appendix.

PBL-Scheme	Closure type	PBLH height definition
YSU	1.0 non-local	Ri_b calculated from surface, is determined by the level at which minimum turbulent flux exists (heat, momentum, moisture). Ri_b a threshold value of zero is used for stable cases, while 0.25 is used for unstable flow.
MYJ	1.5 local	TKE prescribed threshold, where the profile decreases to a prescribed low value ($0.2 \text{ m}^2 \text{ s}^{-2}$)
ACM2-Pleim	1.0 combination nonlocal during unstable conditions with local in stable conditions	Ri_b critical bulk calculated above neutral buoyancy.
Boulac	1.5 local	TKE prescribed thresholdt PBLH as the height where the prognostic TKE reaches a sufficiently small value (in the current version of WRF is $0.005 \text{ m}^2 \text{ s}^{-2}$).
Bretheron-Park	1.5 local	Ri_b threshold
GBM-TKE	1.5 local	Is calculated the inversion jumps based on the difference between the adjacent grid points.
Shin-Hong	1.0 non-local	Ri_b threshold
MYNN	1.5 local	TKE prescribed threshold, where the profile decreases to a prescribed low value

Table 5.1: PBL parameterizations scheme order of closure and height computing method

Chapter 6

Gust model formulations

6.1 Gust model formulations

In this section, the formulation of the proposed gust parameterization (GP) model is described. The reference wind gust model from the European Centre for Medium-Range Weather Forecasting (ECMWF) is presented [IFS, 2011]. The formulation is applied assuming the appliance at hub turbine height of ~ 100 m with different PBL schemes and grid resolutions. The next chapter will analyze the validity of the model up to 100 m AGL. Moreover, a formulation for wind gust, which is a more refined approach to the parameterization originally proposed and presented in [Gutierrez and Fovell, 2015], is described. Finally, both wind gust model formulations, running the WRF model with one year of data, are applied. The parameters of the proposed model are computed by fitting the parameters of data from the CE tower. In the following section, the skill with observation data from the RM tower is shown.

6.1.1 The ECMWF reference wind model

The ECMWF has presented a gust model computing wind gust g as a function of mean horizontal velocity \bar{V} and friction velocity u_* (friction velocity). Eq. 6.1 presents the ECMWF gust model formulation:

$$g = \bar{V} + 7.71u_* \quad (6.1)$$

The ECMWF employs this equation to estimate the wind gust with a reference at 10 m AGL. The reference for the ECMWF model [Panofsky, 1977] presents a relationship for the SL between standard deviation and u_* with measurements taken between 4 m and 32 m.

This equation presumes that gusts are nonconvective; the ECMWF includes an augmentation term when convective activity is expected. In the present work it's analyzed the applicability to forecasting gusts at the turbine level (~ 100 m), which is typically the top of the SL in which the logarithmic wind profile is presumed to be valid, is investigated. The WRF model has iterative interactions between numerical land surface and PBL models. In the SL, the surface flux of momentum, heat, and water is computed; the ECMWF model will be as good as the representation of the models of flux momentum and magnitude of mean velocity. This work analyzed the incidence of horizontal grid resolution in the skill of ECWFMF.

6.1.2 Analysis of the vertical structure of PBL schemes

In chapter 4 the vertical temperature gradient and shear observed in the CE tower and the JI towers for gusty cases (see figures 4.11, 4.12, 4.13 and 4.14) were described; therefore, it is of interest to compare the ability of different PBL schemes to reproduce those vertical structures. Our analysis is focused on the goal of introducing Ri as a parameter for discriminating gusty cases and developing a GP. Figure 6.1 shows the histogram of shear $\frac{\partial V}{\partial z}$ between vertical η levels representative of wind velocity measurement at the top and bottom of the CE tower (~ 100 m and ~ 10 m) for those cases where observed gusts were greater than 15 m/s ($g > 15m/s$) at the top level of measurement (101.8 m AGL). It also shows simulations with the YSU, MYJ, ACM2-Pleim, Boulac, Bretherton-Park, and GBM-TKE PBL schemes, using horizontal grid resolutions of 4 km with a cloud-resolving model.

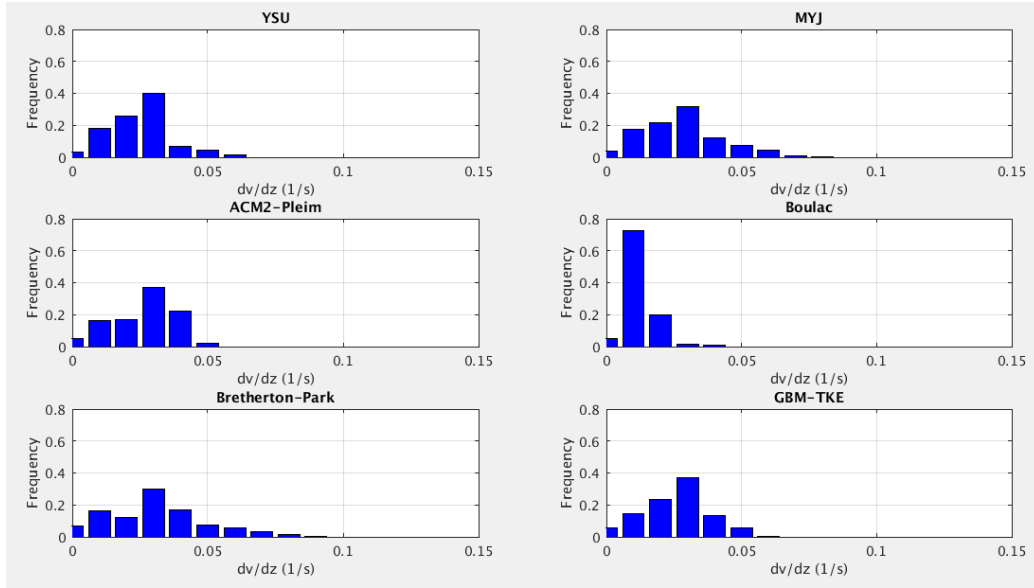


Figure 6.1: Histogram of shear between $\frac{\partial V}{\partial z}$ (~ 100 m and ~ 10 m) (1/s) in cases where $g > 15$ m/s at the top of the CE tower (101.8 m AGL), modeled using PBL schemes YSU, MYJ, ACM2-Pleim, Boulac, Bretherton-Park, and GBM-TKE PBL, with a horizontal grid resolution of 4 km.

Figure 6.2 shows the histogram of the vertical temperature gradient $\frac{\partial T}{\partial z}$ between vertical η levels, representative of temperature measurement at the top and low level in the CE tower (~ 100 m and ~ 10 m) for those cases where observed gusts were greater than 15 m/s ($g > 15$ m/s). The measurements from the top of the CE tower (101.8 m) used the same PBL schemes with horizontal grid resolutions of 4 km in cloud-resolving models.

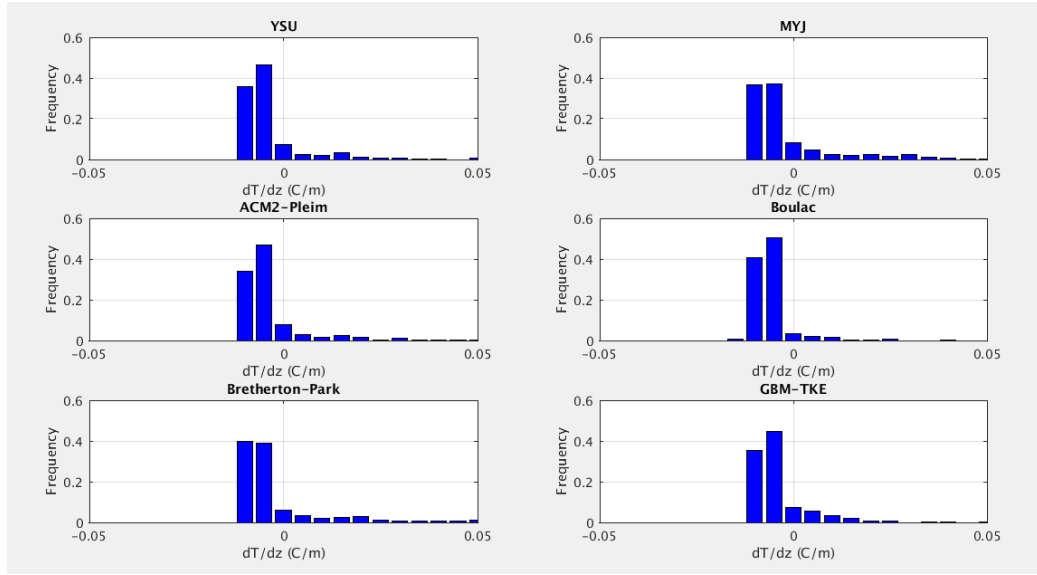


Figure 6.2: Histogram of the vertical temperature gradient $\frac{\partial T}{\partial z}$ (~ 100 m and ~ 10 m) (C°/m) in cases where $g > 15m/s$ measured at the top of the CE tower (101.8 m AGL), using the PBL schemes YSU, MYJ, ACM2–Pleim, Boulac, Bretherton–Park, and GBM–TKE PBL, with a horizontal grid resolution of 4 km.

A comparison of the observed distribution of the vertical temperature gradient $\frac{\partial T}{\partial z}$ and shear $\frac{\partial V}{\partial z}$ for $g > 15m/s$ in the CE tower is shown in figure 4.11, along with forecast simulations for all PBL schemes plotted in figures 6.1 6.2. It can be concluded that the vertical temperature gradient $\frac{\partial T}{\partial z}$ have a realistic representation for all PBL schemes, and shear $\frac{\partial V}{\partial z}$ is under-predicted in all PBL schemes for the first 100 m AGL, with a particular under-prediction in the Boulac PBL scheme.

The Ri is a measure of the relative weight of shear versus buoyancy forces produced by the vertical temperature gradient, therefore we computed Ri for η levels representative of temperature and velocity measurements at top and bottom of the CE tower (~ 100 m and ~ 10 m). Figure 6.3 plots the Ri computed using the WRF model in the CE tower when the observed gusts were greater than 15 m/s, for the same PBL scheme configurations.

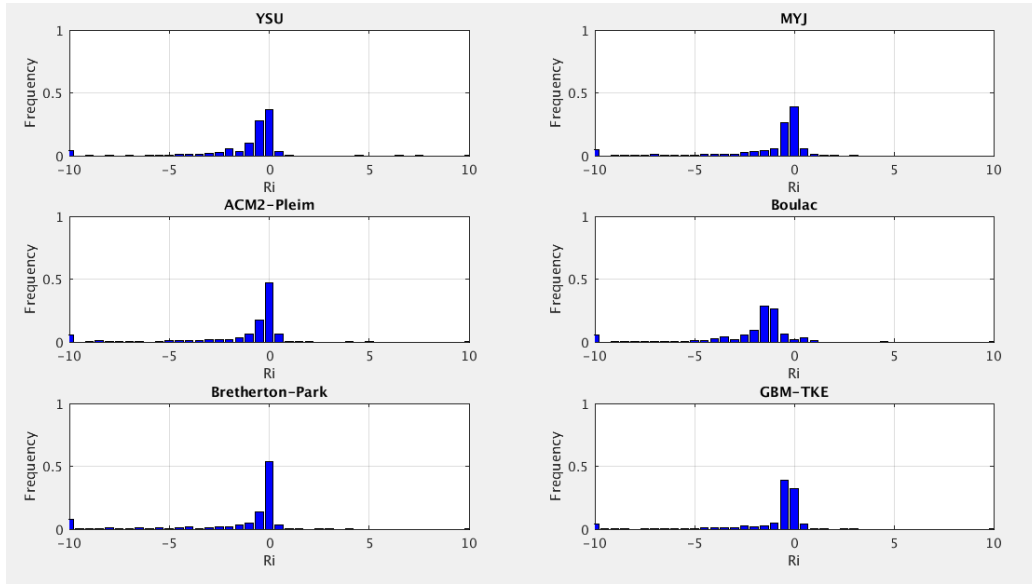


Figure 6.3: Ri computed with the WRF model using six different planetary boundary layer schemes with a horizontal grid resolution of 4 km, when the observed gust in tower CE was > 15 m/s.

As can be seen in figure 6.3, all the models over-predict the magnitude of Ri in comparison with observed Ri in figure 4.14. The best representation of Ri was for Bretherton–Park. In the Boulac PBL, the under-prediction of $\frac{\partial V}{\partial z}$ implies a significant over-prediction in the magnitude of Ri .

The analysis shows that it is possible to tune a marginal critical interval with δRi to introduce the forecast Ri with numerical model to discriminate gusty cases when $-\delta Ri < Ri < \delta Ri$. For some PBL schemes, the Ri computed from the model could be improved with a bias correction, in particular Boulac and GBM-TKE. Further analysis needs to be done to improve the formulation of PBL schemes in order to obtain a more realistic shear in first 100 m AGL.

Gusty cases are more difficult to forecast with numerical models; in particular, marginal stability cases (where transition regimes in PBL physics or small-scale processes are unresolved by WRF); there are also cases where the real vertical temperature gradient is negative but the model forecast a positive value.

However, without considering the Boulac PBL, a significant frequency of gusty cases can be found with marginal Ri . Therefore, the use of a defined interval $-\delta Ri < Ri < \delta Ri$ with $\delta Ri = 0.5$ is proposed as an improvement in computing gust parameterization (as a correction), for the marginal cases discriminated as forecasts of a gusty condition.

6.1.3 Surface layer sensitivity

Figure 6.4 presents a comparison between two PBL numerical schemes that use different formulations for the SL: the Shing-Hong, which uses Monin Obukov [Panofky, 1977], and MYNN 2.5, which uses a specific master length scale (mixing length) [Nakanishi 2001]. These plots summarize the comparison, showing histograms of shear $\frac{\partial V}{\partial z}$, vertical temperature gradient $\frac{\partial T}{\partial z}$, and Ri (~ 100 m and ~ 10 m) in cases where $g > 15$ m/s in the CE tower. The two PBL/surface schemes produce similar results, with a slight advantage for the Shin-Hong, as it has a higher peak at $Ri \sim 0$.

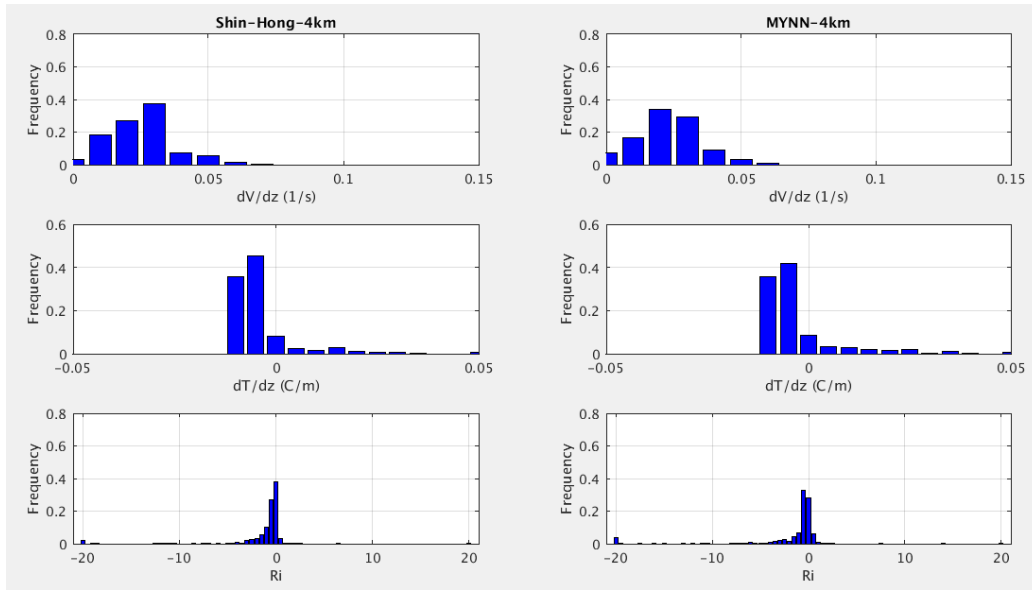


Figure 6.4: Histogram of shear $\frac{\partial V}{\partial z}$, vertical temperature gradient $\frac{\partial T}{\partial z}$, and Ri (~ 100 m and ~ 10 m) in cases where $g > 15$ m/s at the top of the CE tower (101.8 m AGL), for Shin-Hong and MYNN PBL schemes

The present work also analyzed different PBL schemes (figures 6.1, 6.2, and 6.3, including Pleim with surface approach), that had different formulations for the SL [Pleim, 2007a]. The analysis showed no significant differences in the vertical structure forecast, although there is an under-prediction of the shear for all the SL schemes for gusty cases; this impacts the skill of the Ri forecast. Chapter 7 summarizes the skill all the PBLs and different SLs showed at forecasting extreme wind gusts.

6.1.4 Stability discrimination analysis

As presented in Chapter 4, extreme gusts have a direct relationship with stability regimes; therefore, the ability of a PBL scheme to represent the stability regime, and the PBL height computed when an extreme gust occurred, will be analyzed next. Figure 6.5 plots PBL height vs. observed gusts in the CE tower, for the eight PBL schemes simulated: YSU, MYJ, ACM2-Pleim, Boulac, Bretherton-Park, GBM-TKE, Shin-Hong, and MYNN, with a 4 km horizontal grid size, color-coded green when $\frac{\partial T}{\partial z} > 0$ and red when $\frac{\partial T}{\partial z} \leq 0$ as computed by the WRF model.

Figure 6.6 presents the same scatterplot color-coded by $\frac{\partial T}{\partial z}$ observed at the CE tower, as computed with tower temperature measurements. In both plots, the blue line shows the gust limit of 15 m/s.

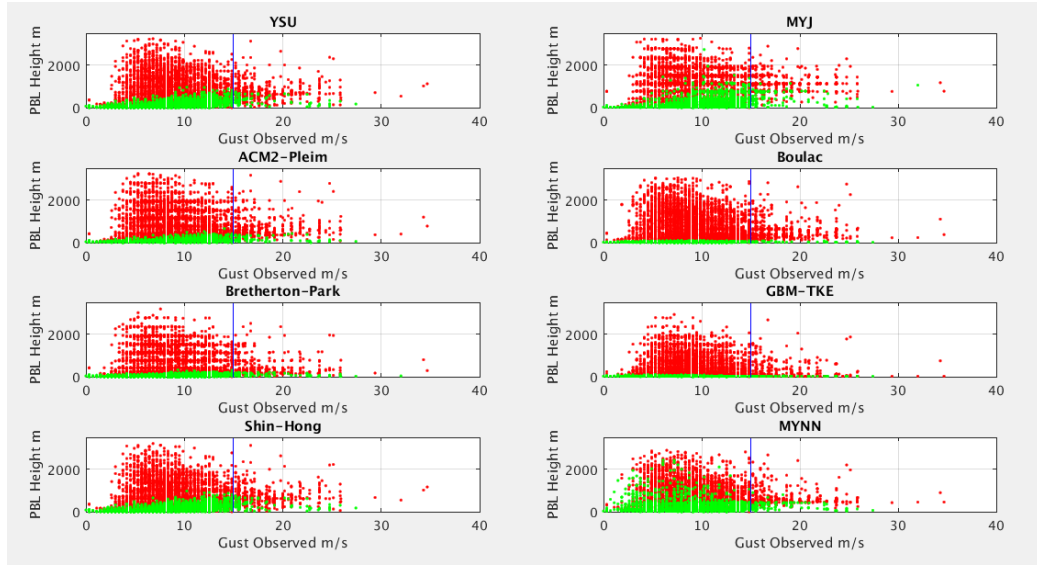


Figure 6.5: PBL simulated height vs. observed gusts in the CE tower, for the PBL schemes YSU, MYJ, ACM2-Pleim, Boulac, Bretherton-Park, GBM-TKE, Shin-Hong, and MYNN, with a 4 km horizontal grid. Green dots represent $\frac{\partial T}{\partial z} > 0$ and red dots represent $\frac{\partial T}{\partial z} \leq 0$; the color codes are as computed by the WRF model

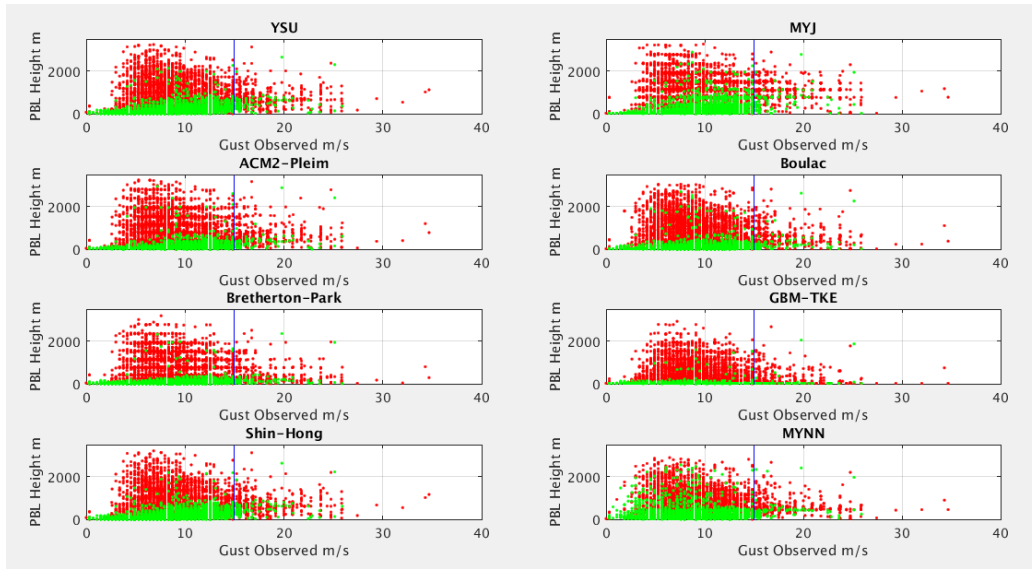


Figure 6.6: PBL simulated height vs. observed gusts in the CE tower, for the PBL schemes YSU, MYJ, ACM2–Pleim, Boulac, Bretherton–Park, GBM–TKE, Shin–Hong, and MYNN, with a 4 km horizontal grid size. Green dots represent $\frac{\partial T}{\partial z} > 0$ and red dots represent $\frac{\partial T}{\partial z} \leq 0$; the color codes are as computed by temperatures observed in the CE tower

The similarity in the color patterns between figures 6.5 and 6.6 show that the WRF model appears to reproduce measured stability ($\frac{\partial T}{\partial z}$) well, at least in bulk. Thus, we now attempt to incorporate stability information into GP more directly.

Another conclusion is that extreme gusts, those higher than 15 m/s, show that PBL height is generally lower than 1,000 m, with different tendencies depending on the scheme formulation. Extreme gusts do not happen in extremely deeper PBLs.

6.1.5 Proposed Gust Parameterization (GP)

Although [Gutierrez and Fovell, 2015] analyzed three different regions with relatively different wind conditions, the focus was on stability regimes with a particular description of diurnal regimes, and the proposed model of gust parameterization includes a fixed top velocity proximity at the PBL height for computing the shear. It is suggested that a wind gust parameterization

should include a more direct awareness of the ambient stability and shear. In the present work, a new and different strategy is proposed that could help capture sizable gusts that occur in marginal stability conditions. The focus of the analysis will be on one geographical region, for a more detailed presentation of wind gust formulation.

As shown in Chapter 4, large gusts require near-neutral SLs ($Ri \sim 0$), copious vertical shear, and rather shallow PBLs. If Ri is too negative, it is probably because there is insufficient vertical shear to support gustiness. If the PBL is too deep, the momentum is probably mixed too thoroughly. This large gust is associated with a higher level of mechanical turbulence, from an event with high horizontal velocity both at wind turbine height and at the top of the PBL.

Chapter 4 presented the analysis of wind velocity observations at ~ 100 m. It was found that GF has a clear pattern of different nighttime results as compared to daytime data. The daily variation in GF is produced by a thermal vortex, produced when the sun's radiation heats the land surface [Kaimal, 1976], and mixing in atmosphere diminishes the shear, but thermal buoyancy produces turbulence and higher fluctuation of mean values. The vertical temperature gradient near the surface ($\frac{\partial T}{\partial z}$) is a measure of heat exchange between the atmosphere and the land surface. $\frac{\partial T}{\partial z}$ near surface levels is introduced to discriminate cases that are related to heat transferred from the land to the lower atmosphere. We computed the vertical temperature gradient ($\frac{\partial T}{\partial z}$), with differences in η levels closer to the surface, at ~ 100 m and ~ 10 m.

The conceptual approach of GP model is focused on forecasting the gust factor GF ; in Eq. 6.2 a minimum value GF_{min} is proposed, with dependency of velocity at hub height V_{100} ($\sim 100m$) and stability regime computed with $\frac{\partial T}{\partial z}$. The GF_{min} proposed was motivated by analysis of observational gust factor data presented in Section 2 (see figures 4.6, 4.7, 4.8, and 4.9). In the proposed parameterization scheme, GF is increased depending on the bulk shear of the PBL, considering the bulk difference in velocity that is a measure of the mechanical production of turbulence. Then a gust factor is computed by adding a term $K \frac{\Delta V^{Top}}{V_{100}}$, related to the computed difference in velocity as a significant scale, related to the bulk share from the top. This scale is

computed by $\Delta V^{Top} = \max(0, (V_{MAX} - V_{100}))$

if $\frac{\partial T}{\partial z} \leq 0$, with V_{MAX} velocity at top of the PBL and if $\frac{\partial T}{\partial z} > 0$, with V_{MAX} a top velocity (arbitrary height) close to the height of the wind turbine, proposed as $\sim 200m$.

Finally, the forecast gust factor is increased by multiplying by a factor, $S_{Ri} = 1.15$, in the gusty cases when $(GF_{min}V_{100} + K\Delta V^{Top}) > 11.5m/s$ for Ri between $(-0.5 < Ri < 0.5)$, as shown in Eq. 6.3.

$$GF = GF_{min} + K \frac{\Delta V^{Top}}{V_{100}} \quad (6.2)$$

If $(GF_{min}V_{100} + K\Delta V^{Top}) > 11.5m/s$ and $(-0.5 < Ri < 0.5)$

$$GF = S_{Ri}(GF_{min} + K \frac{\Delta V^{Top}}{V_{100}}) \quad (6.3)$$

The model is developed with the best fit coefficient K and GF_{min} , the best fit for each PBL scheme is presented in the Appendix. K and GF_{min} depend on the interval of the velocity V_{100} and stability condition $\frac{\partial T}{\partial z}$. Figure 6.7 presents the best fit coefficient K and $Gmin$ for the Shin–Hong PBL scheme for horizontal grid resolutions of 12 km and 0.44 km for observational data from CE tower. The S_{Ri} factor, the coefficient that helps reduce bias, was determined empirically; see the analysis in Chapter 7.

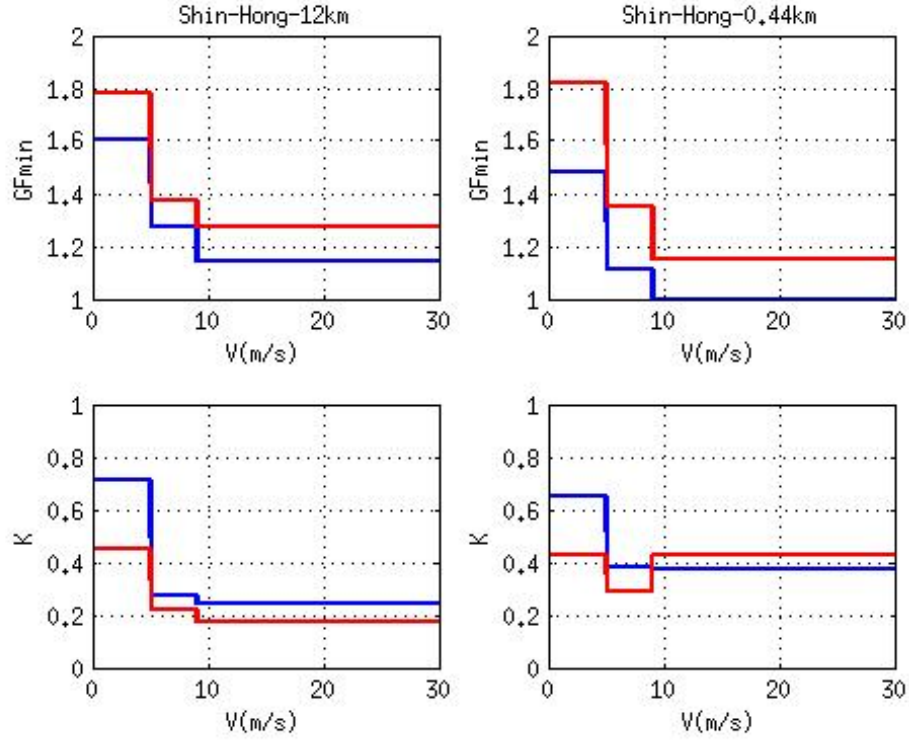


Figure 6.7: K and G_{min} fit optimally with the CE tower observational data for Shin-Hong horizontal grid resolutions of 12 km and 0.44 km. Blue represents $\frac{\partial T}{\partial z} \geq 0$ and red represents $\frac{\partial T}{\partial z} < 0$. Intervals of velocities computed with the WRF model are $0m/s < V \leq 5m/s$, $5m/s \leq V < 9m/s$ and $9m/s \leq V$

$G_{F_{min}}$ shows that the best fit values are higher for low resolution domains, meaning that once the horizontal resolution of the model is increased, velocity values with higher means are forecast by the model with the seated PBL scheme. The $G_{F_{min}}$ and K best fit coefficient for each PBL scheme and horizontal grid resolution are presented in the Appendix.

The V_{MAX} represents velocity at the top of the PBL (when $\frac{\partial T}{\partial z} \leq 0$), that is, velocity in a free atmosphere where the skill is high. [Siuta, 2017] compared the sensitivity of wind turbine hub-height wind speed forecasts to the PBL scheme, grid length, and initial condition selection in a WRF model, over complex terrain. In the present work, the observational data and point in the grid domain were located on flat terrain. [de Almeida, Gutierrez, 2015]

analyzed the skill of the WRF model run with different PBLs, with a grid resolution of 6 km over the same location as the CE tower, and compared the different mean wind velocity observations at 10 m and 100 m. The PBLs they analyzed show good skill for 100 m. Gust is a measure of the peak velocity when turbulence is produced. The scale of energy- and flux-containing turbulence is much smaller than the scale of the spatial filter employed for the equations of motion in the WRF model using horizontal grid resolution [Wyngaard, 2004].

Considering the development of the model to forecast extreme gust, according to the analysis of observation given in chapter 4, no extreme wind gust was noted during strongly stable conditions when $\frac{\partial T}{\partial z} > 0.01$. In the numerical model formulation, it is proposed that for stable cases ($\frac{\partial T}{\partial z} > 0$), and slightly stable cases (related to marginal stability, or transitions in stability class), the velocity scales are the velocity at hub height (V_{100}) and the top velocity ($V_{MAX} \sim 200m$). This scale is representative of the shear near the top of the turbine, representing the mechanical production of turbulence, and is useful for improving forecast of gusts in marginal or transitional stability regimes.

Figure 6.8 presents the schematic of further proposed relevant parameters for the gust model formulation. The blue vortex in the schematic represents the vortex related to mixing length; in [Prandtl, 1925] the turbulent vortex is assumed to have a length scale $l = kz$, with $k = 0.4$. There are no other descriptions with observational data analysis in the literature. Regarding the evolution of the mixing length during the stable and unstable evolution of the atmosphere, MYNN 2.5 [Nakanishi 2001] proposes a formulation for the mixing length in dependent of the stability regime. This scale of mixing and schematics vortexes are presented for conceptual representation and visualization of gusts as a consequence of the production of turbulence. A difference ΔV^{Top} between V_{MAX} and velocity at hub height V_{100} is proposed, to represent the mechanical vortex produced by mechanical forces (shear).

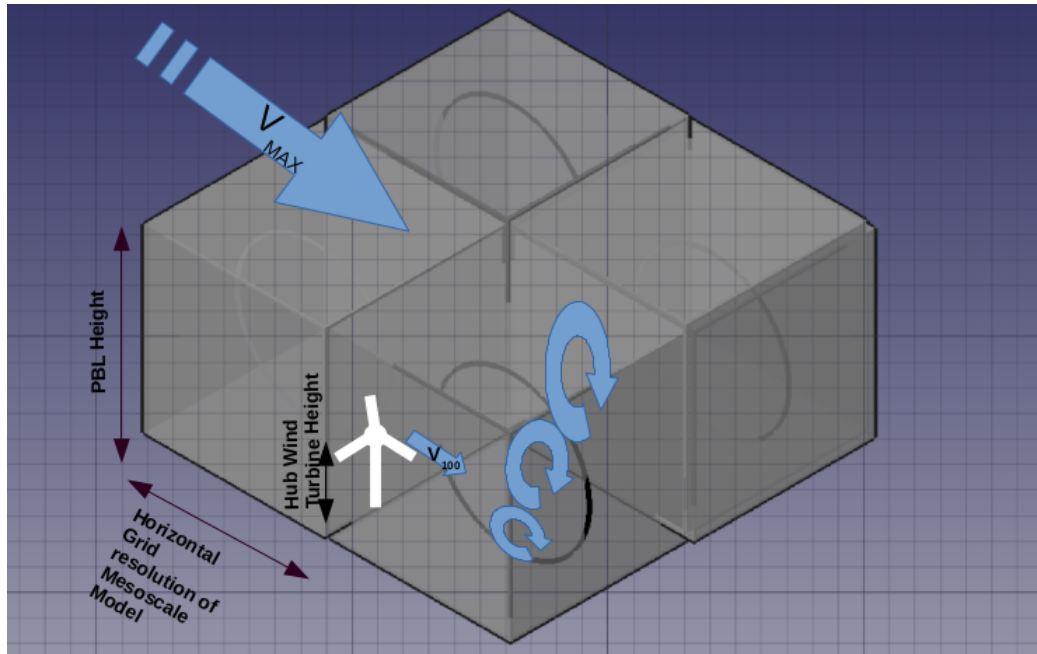


Figure 6.8: Schematic of further relevant parameters proposed for gust parameterization formulations, for wind turbine hub height in unstable conditions.

When running an atmospheric numerical model such as the WRF model, a vertical and horizontal grid resolution are defined. The horizontal grid resolution, in particular, is extremely relevant when focusing on gusts; that magnitude is directly related to turbulence. [Shin and Hong, 2013] examined the grid-size dependencies of resolved and parameterized vertical transports in CBLs for horizontal grid scales of 50–4,000 m. Their main focus was an analysis of the effects of the relative contributions of buoyancy and mechanical forcing on the grid-size dependency, in terms of forcing-dependent large eddies (i.e., coherent structures). They concluded that the relative contributions of the resolved TKE and vertical fluxes to the corresponding total TKE and fluxes increased as wind shear became important for a given grid size. This is attributed to the larger horizontal scale of the rolls in shear buoyancy-driven CBLs. The present work tests the new PBL scheme [Shin and Hong, 2013] that attempts to represent the subgrid-scale turbulent transport in CBLs.

Chapter 7

Analysis of numerical results

For the numerical analysis, the result of the ECMWF model is compared with those of the proposed GP model. The skill of the eight different PBL schemes with two nested grid resolutions of 12–4 km and two PBL schemes with 1.3 km and 0.44 km grid resolution, are presented.

The results of both models were tested with data from the RM tower measured over 365 days from August 8, 2014 to August 7, 2015. The selected period correlates with those for which continuous high-quality data measured from towers with the same mesoscale wind conditions were available. The GP model coefficients GF_{min} and K were computed and tuned with the CE tower data for each PBL scheme and for each horizontal grid resolution; therefore, the skill of the reference ECMWF model is shown compared to the data from the independent RM tower.

The RM tower is located on noncomplex topography near an estuary of the La Plata River. Therefore, the result of the comparison shown in this section can be associated with the incidence of PBL schemes when there are no relevant impacts from hills in the terrain. The comparison in this work shows how the increased resolution of the horizontal grid better represents mesoscale winds, that is, how the surface terrain and atmospheric interact over simple topography. This skill comparison can be useful in understanding the skill of the WRF model in capturing a mesoscale event that produces a gust event greater than the selected value.

This section presents the analysis results of the models to examine the performance in terms of forecasting gust events. It explores the concept of

developing an alarm for gust events, for practical application in managing the electric grid during wind gust events greater than the defined value. It does not classify mesoscale events; instead, it statistically compares the ability of the ECMWF model and developed GP models to forecast gust observations by wind cup measurement at the hub height of wind turbines (~ 100 m). First the impact of the discrimination of gusty cases with Ri is shown; then the skill of all simulated PBLs, and the impact of the skill of gusts with increasing horizontal grid resolutions, are compared.

7.1 Analysis of discrimination of gusty cases with Ri in GP

As described in Eqn. 6.3, the formulation of the GP developed in the present work proposes discriminating the gusty cases with the computed Ri number in the first 100 m of the PBL. Next, the RM tower observational data was analyzed with the best fit coefficient computed for the CE tower. To show the impact of the discrimination, figure 7.1 plots the results for Shin–Hong PBL using 4 km grid resolution. The top row shows the scatterplots of the forecast Ri and gusts g , the left-hand column shows computations of gust with $S_{Ri} = 1$ (without Ri discrimination), and the right-hand column shows plots of gust computed with $S_{Ri} = 1.15$ (with Ri discrimination). The cases in which the observed gust was greater than 15 m/s are shown in magenta, and the green line shows $g=15$ m/s. In the bottom row are the histograms of errors for gusty cases when the observed gust was greater than 15 m/s; the left-hand column shows $S_{Ri} = 1$, and the right-hand column shows $S_{Ri} = 1.15$.

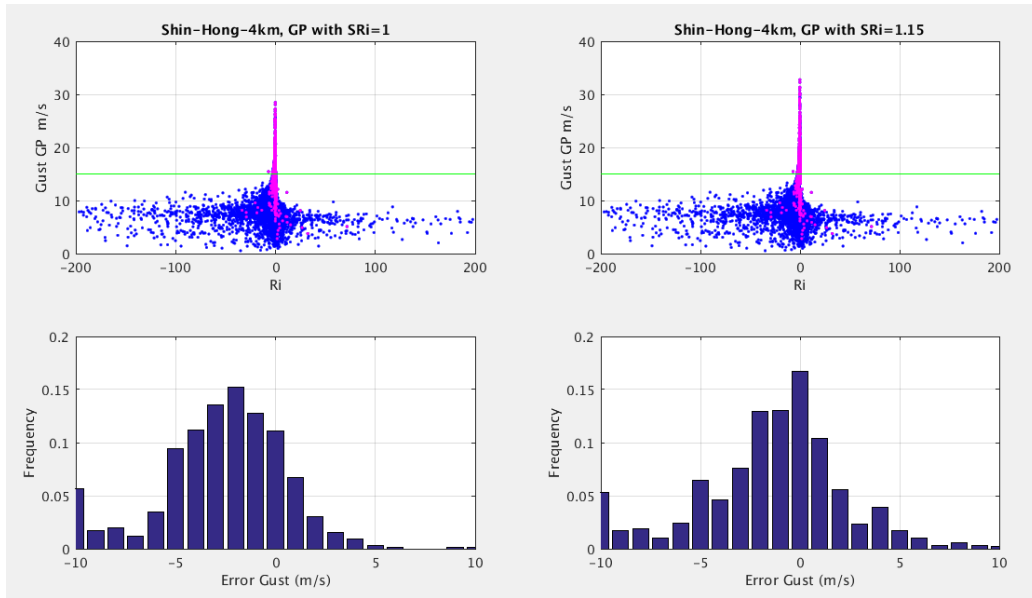


Figure 7.1: Shin-Hong PBL, using 4 km grid resolution, for the RM tower. The left-hand column shows forecast gust Ri when $S_{Ri} = 1$ and the right-hand column shows forecast gust when $S_{Ri} = 1.15$. The blue dots show all cases, the magenta dots show cases when the observed gust $g > 15m/s$, and the green line shows $g = 15m/s$. The bottom row shows the histograms of errors for gusty cases when observed gust $g > 15m/s$

Figure 7.1 shows how well the WRF model Shin-Hong works at correlating observed gusts with model computed Ri . All cases are shown with blue dots, and the distribution presents same pattern as the observations shown in Fig. 4.13, which means that all gusty cases happen with $Ri \sim 0$. The magenta-colored observations represent observations showing $g \geq 15m/s$. Most of these are clustered around the model-computed $Ri \sim 0$, with only a few points located at other Ri values, which also shows that when the observed $Ri \sim 0$, the model is in agreement with observations. The skill of the Ri discrimination shows an improvement for gusty cases, as can be seen in the histograms. Magenta dots on the scatterplots show how the parametrization works, increasing the computed gust (with $S_{Ri} = 1.15$), when $(GF_{min}V_{100} + K\Delta V^{Top}) > 11.5m/s$ for Ri between $(-0.5 < Ri < 0.5)$.

The histogram in figure 7.1, on the lower left, reveals that the model with $S_{Ri} = 1$ is under-forecasting extreme gusts. The empirically-derived

factor $S_{Ri} = 1.15$ helps compensate for this bias, and is applied when model-estimated Ri is close to zero. This helps concentrate the magenta points even more narrowly around model-estimated $Ri = 0$, which further improves the skill of the model.

7.2 Wind gust alarms

In [Friederichs, 2009], it is argued that reliable forecasts of wind gusts offer the potential to mitigate the destruction and human loss they cause, and to better plan disruption times and subsequent clean-up operations. Key users of gust warnings are emergency managers, air and rail traffic controllers, energy companies, and the general public. Thus, improving the quality of gust warnings is of great importance as wind gust warnings are given for different classes of wind gust speed, i.e., exceedances of certain thresholds.

In the present work, a true alarm (TA) is assigned to cases if the wind gust forecast computed by the model is greater than a selected gust. This work proposes a selected gust of 15 m/s to activate the alarm based on actual measurements. A false alarm (FA) is assigned if the gust forecast computed by the model is greater than the selected gust (15 m/s) but the actual measurement was not observed to be greater than the selected value.

Moreover, it is attempted to determine whether it is possible to enhance an operational model with the interval of time of the gust forecast. The wind gust forecast model can be analyzed in different objective time intervals, with maximum gust forecasts at 1, 6, and 12 hours. This condition could be useful for determining the time interval for an operational wind gust alarm forecast model. In an operational model, the concept of developing a forecast for wind gusts greater than the selected value (the gust alarm) can be of significant value in energy systems with high levels of wind power participation, such as the Uruguayan system [web, UTE].

Forecasting a gusty event presents useful information for abrupt changes to power production; therefore, 6 and 12 h are reasonable time intervals to the operation of human management decisions in an electric system. An operational model could bring new alarm forecasts four times a day related to the available initial condition of the model run at 00:00, 06:00, 12:00, and

18:00 GMT.

7.3 Skill of forecast gust with increasing horizontal grid resolution

Grid resolution analysis is relevant to understand the ability of the mesoscale model to simulate scales of turbulence when resolution is increased [Wyngaard, 2004]. In a practical sense, measuring the skill of different horizontal grid resolutions is useful to determine the best configuration related to the computational cost for application of the operational model.

In figures 7.2, 7.3, and 7.4, the forecast wind gust for the ECMWF model (m/s) is plotted vs. the forecast GP (m/s) for the RM tower at 100 m, considering an increasing time interval for computing wind gust for the model, that is, 1, 6, and 12 h. The scatterplots show the results of the Shin–Hong PBL scheme for 12 km, 4 km, 1.3 km, and 0.44 km horizontal grid resolutions, for intervals of 1, 6, and 12 h. Blue dots represent all cases, red dots represent the cases where the real gust observed in at the RM tower was higher than 15 m/s, and the green lines show the 15 m/s limit for both models. The horizontal green line shows the limit of TA for GP and the vertical green line shows the limit of TA for the ECMWF. Red dots represent the following in the following quadrants: a) TA-GP, event missed ECMWF, b) TA-GP and TA-ECMWF, c) event missed by GP and ECMWF, and d) event missed by GP, TA-ECMWF

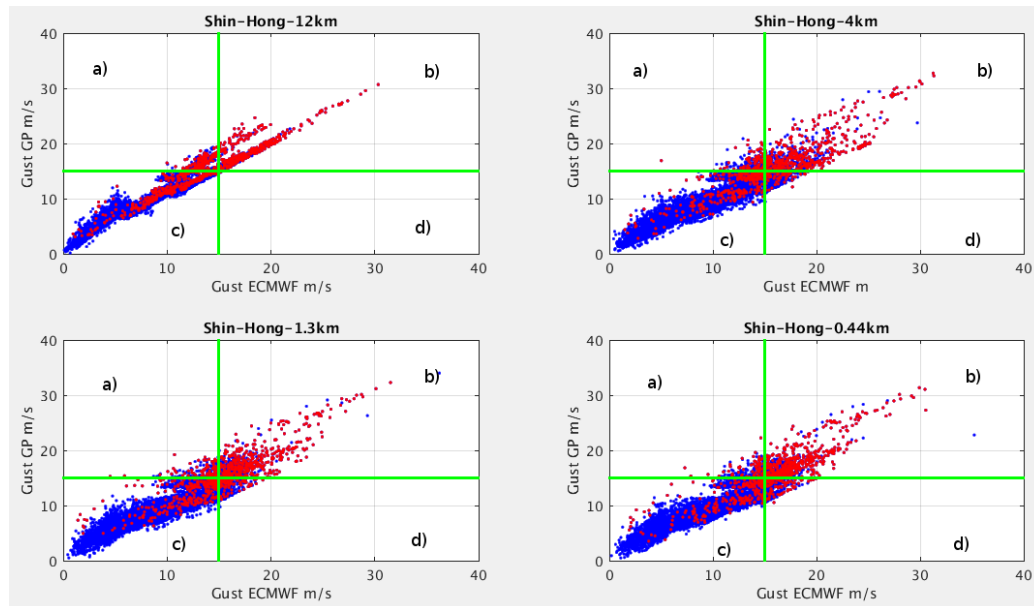


Figure 7.2: ECMWF g (m/s) vs. GP (m/s) gusts forecast at the RM tower, using the Shin-Hong PBL scheme at 12 km, 4 km, 1.3 km, and 0.44 km horizontal grid resolution. Red dots show gusts observed at $g > 15 \text{ m/s}$ for 1 h.

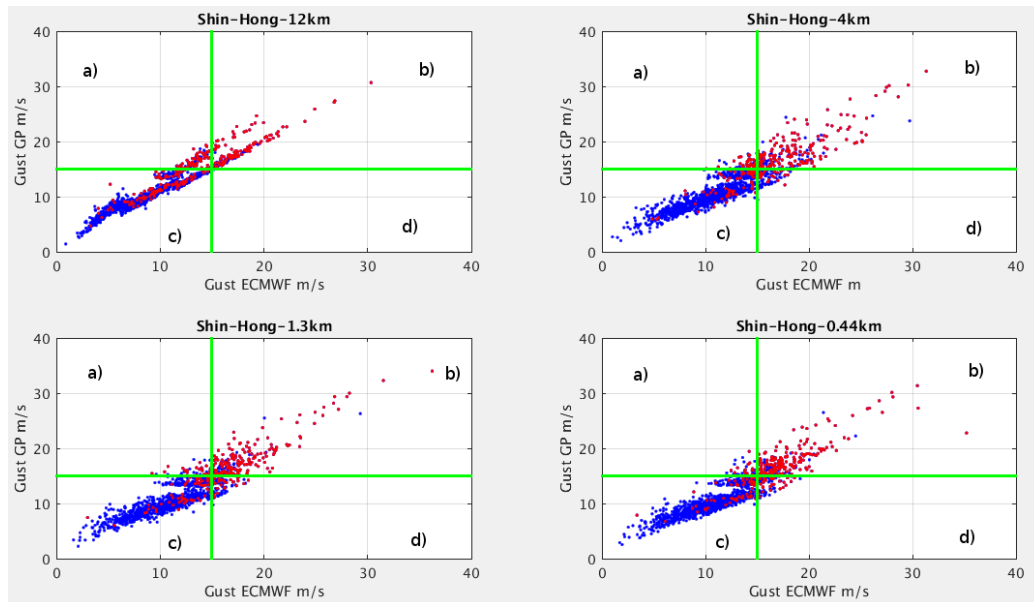


Figure 7.3: ECMWF g (m/s) vs. GP (m/s) gusts forecast at the RM tower, using the Shin-Hong PBL scheme for 12 km, 4 km, 1.3 km, and 0.44 km horizontal grid resolution. Red dots show gusts observed at $g > 15 \text{ m/s}$ for 6 h.

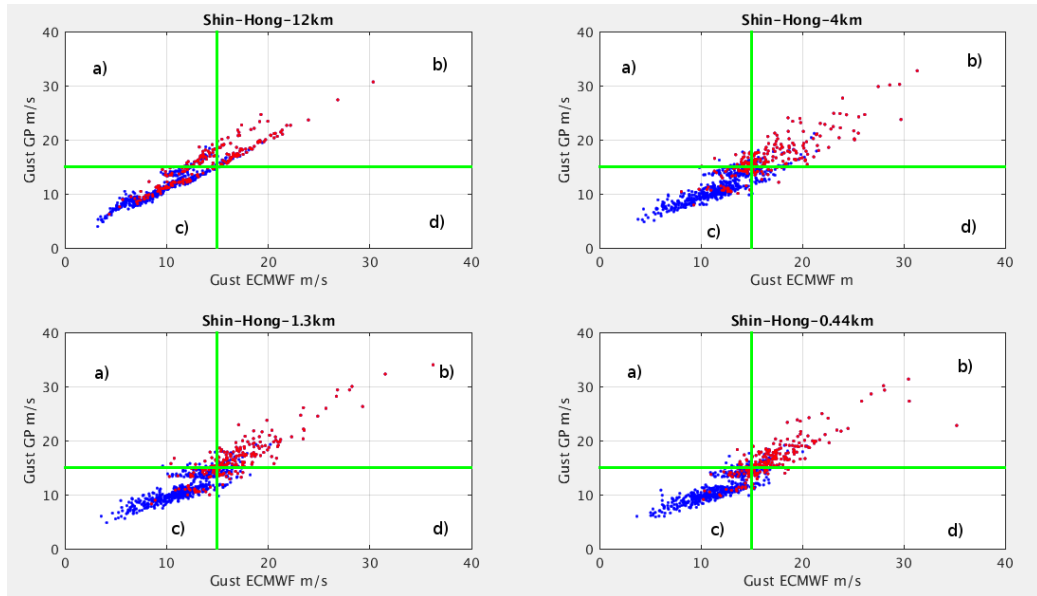


Figure 7.4: ECMWF g (m/s) vs. GP (m/s) gusts forecast at the RM tower, using the Shin–Hong PBL scheme for 12 km, 4 km, 1.3 km, and 0.44 km horizontal grid resolution. Red dots show gusts observed at $g > 15\text{m/s}$ for 12 h.

It can be seen that the number of red dots increase in quadrant b), and decrease in quadrant d), when the grid horizontal resolution is increased for all time intervals. This means the skill of both models at forecasting gusts $g > 15\text{m/s}$ tends to increase when the horizontal grid resolution is increased.

Figures 7.5, 7.6, and 7.7, present the same scatterplots, showing the results with blue dots plotted for all cases, magenta dots representing cases where the real gusts observed at the RM tower was lower than 15 m/s, and the green lines plotting the 15 m/s limit for both models (the horizontal green line limit of TA for GP, and the vertical green line limit of TA for ECMWF). Magenta dots represent the following in the following quadrants: a) FA-GP and not FA-ECMWF, b) FA-GP and FA-ECMWF, c) not FA-GP and not FA-ECMWF, and d) not FA-GP and FA-ECMWF.

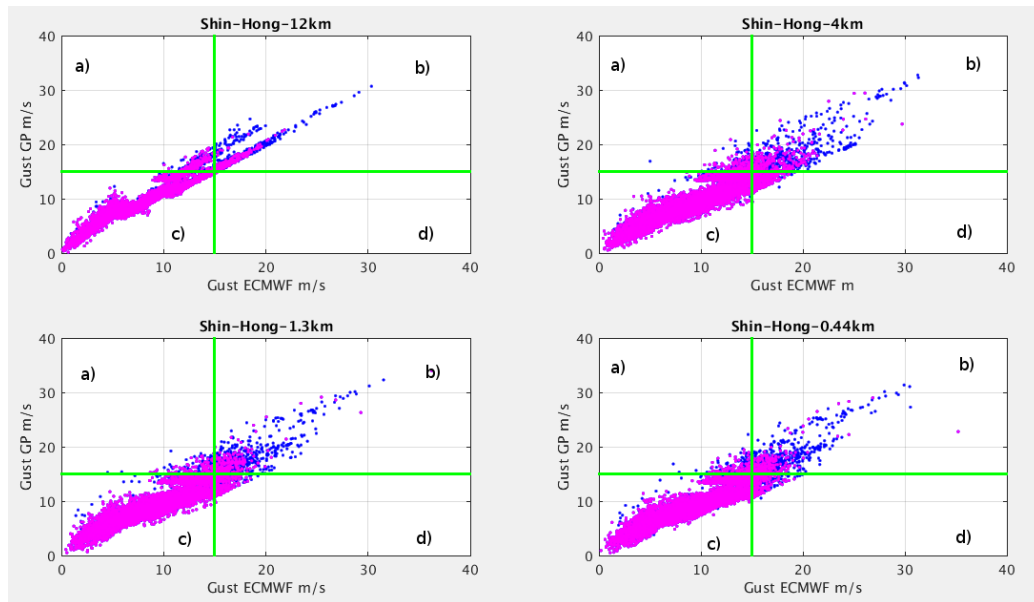


Figure 7.5: ECMWF g (m/s) vs. GP (m/s) gusts forecast at the RM tower, using the Shin-Hong PBL scheme for 12 km, 4 km, 1.3 km, and 0.44 km horizontal grid resolution. Magenta dots show gusts observed at $g < 15$ m/s for 1 h.

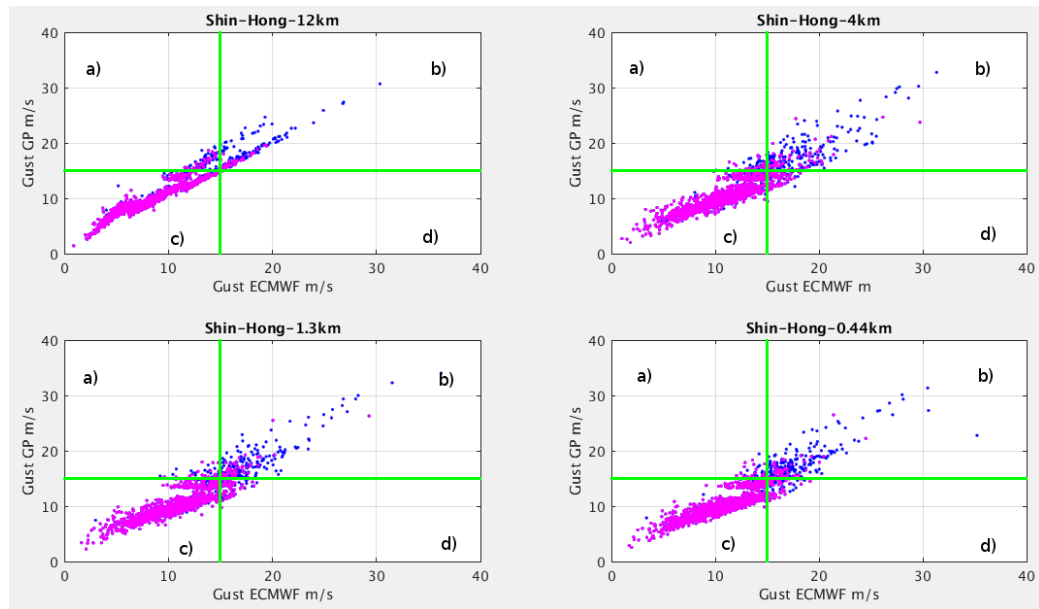


Figure 7.6: ECMWF g (m/s) vs. GP (m/s) gusts forecast at the RM tower, using the Shin-Hong PBL scheme for 12 km, 4 km, 1.3 km, and 0.44 km horizontal grid resolution. Magenta dots show gusts observed at $g < 15 \text{ m/s}$ for 6 h.

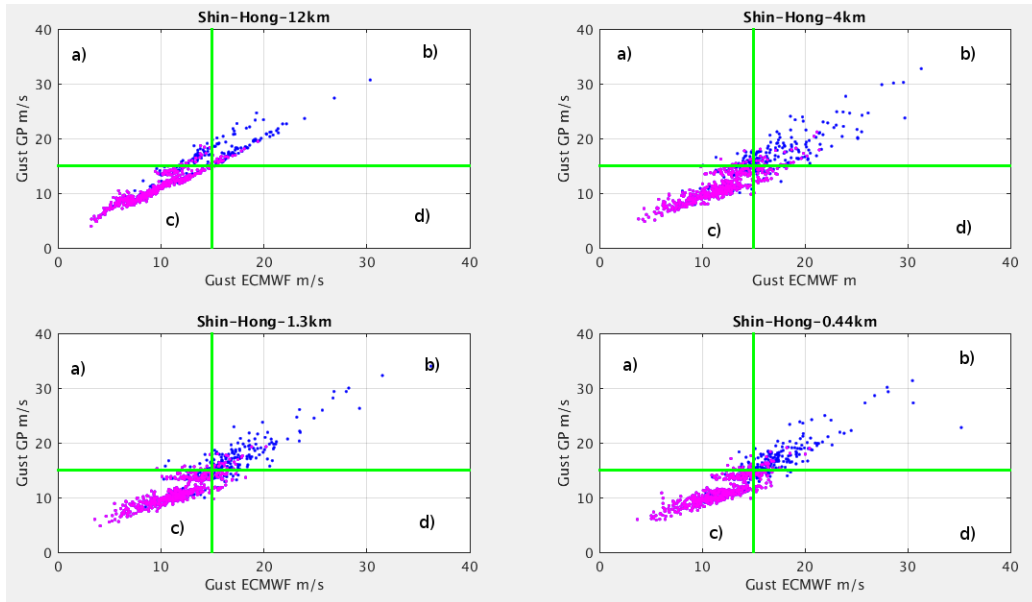


Figure 7.7: ECMWF g (m/s) vs. GP (m/s) gusts forecast at the RM tower, using the Shin–Hong PBL scheme for 12 km, 4 km, 1.3 km, and 0.44 km horizontal grid resolution. Magenta dots show gusts observed at $g < 15\text{m/s}$ for 12 h.

It can be seen that the number of magenta dots in quadrant b) decrease when the grid horizontal resolution is increased for all time intervals. This means that the skill of both models at forecasting wind gust tends to increase (meaning fewer FA cases), when the horizontal grid resolution is increased. The 12 km grid has more magenta dots in quadrant a), which means the GP model overestimated those cases. To see this tendency more clearly, the TA and FA for all PBL schemes and resolutions will be computed.

		12km								4km								1.3 km		0.44 km		
		YSU	MYJ	ACM2 Pleim	Boulac	Bretherton Park	GBM TKE	Shin Hongj	MYNN	YSU	MYJ	ACM2 Pleim	Boulac	Bretherton Park	GBM TKE	Shin- Hong	MYNN	MYJ	Shin Hongj	MYJ	Shin Hongj	
1h	N°-E	868																				
	ECMWF	TA	38%	38%	42%	40%	37%	40%	38%	40%	56%	62%	62%	52%	65%	61%	56%	70%	64%	57%	70%	64%
	ECMWF	FA	46%	42%	47%	42%	45%	42%	46%	42%	55%	58%	52%	62%	55%	54%	56%	52%	48%	54%	48%	
	GP	TA	57%	59%	55%	54%	56%	54%	59%	58%	59%	65%	61%	42%	63%	64%	59%	57%	62%	57%	62%	59%
	GP	FA	48%	51%	46%	45%	50%	45%	48%	46%	43%	49%	46%	38%	53%	53%	44%	45%	46%	41%	47%	41%
6h	N°-E	285																				
	ECMWF	TA	36%	37%	41%	39%	36%	39%	36%	39%	65%	69%	68%	56%	79%	68%	65%	78%	72%	67%	80%	73%
	ECMWF	FA	30%	28%	31%	28%	30%	28%	30%	26%	42%	49%	41%	41%	51%	45%	42%	46%	41%	36%	42%	34%
	GP	TA	56%	58%	54%	54%	56%	54%	53%	55%	66%	72%	65%	47%	72%	72%	67%	63%	70%	64%	72%	66%
	GP	FA	32%	36%	31%	30%	35%	30%	45%	32%	31%	39%	34%	28%	46%	43%	31%	36%	35%	29%	35%	28%
12h	N°-E	211																				
	ECMWF	TA	37%	38%	40%	38%	37%	38%	37%	39%	66%	73%	68%	56%	83%	72%	65%	81%	75%	68%	82%	74%
	ECMWF	FA	23%	22%	24%	22%	23%	22%	23%	21%	33%	40%	35%	34%	42%	37%	34%	39%	33%	30%	34%	26%
	GP	TA	56%	57%	55%	54%	57%	54%	52%	55%	67%	77%	68%	50%	75%	75%	67%	66%	73%	64%	75%	67%
	GP	FA	25%	31%	23%	26%	29%	26%	39%	27%	23%	31%	27%	22%	40%	37%	23%	28%	26%	20%	28%	19%

Table 7.1: True alarm (TA) and false alarm (FA) conditions for reference model ECMWF (EU) and the proposed GP model (GP) for all PBL schemes and grid horizontal resolutions within the time window at the RM tower from August 8, 2014, to August 7, 2015

7.4 Skill of alarms, for all PBL schemes and resolutions

The results of the TA and FA occurrences for all PBL schemes and resolutions are presented in Table 7.1. The TA percentage was computed by dividing by the total number of actual cases higher than 15 m/s, and the FA percentage was computed by taking the total number of cases higher than 15 m/s computed by the model. The TA and FA are shown for time intervals of 1, 6, and 12 h.

As shown in Table 7.1, TA increases and FA decreases when the horizontal grid resolution increases. The proposed GP model had a better skill under a horizontal grid domain with lower resolutions, this was shown in this work for 12 km. Bretherton–Park and MYNN have a higher global skill in the 4 km horizontal grid domain, with the former showing the most real representation of Ri , which means GP has the ability to discriminate gusty cases. MYNN is a parametrization with most refined approach for computing the master length independence of the stability regime. The increase in TA and decrease

in FA occurs when the time interval increases. For an operational model that provides information to decision makers, the time interval can be applied. GP can be useful in an operational model because its higher skill at low resolutions costs less in terms of the associated computational cost.

In this work, the forecast horizon is not evaluated. It can be considered that this result has a better configuration relative to other models. If an operational model is implemented, further analysis using the time horizon and impact on skill with ensembles need to be analyzed and computed.

Chapter 8

Conclusion

Both observed gust magnitudes and factors (the ratios of gusts to the mean winds) increased as the atmosphere became less stable and an asymptotic gust factor value of 1.33 was found. A characteristic observed bulk Richardson number Ri was identified for gusty cases, $-0.2 < Ri < 0$ in the first 100 m AGL. All PBL schemes under-predicted the shear in the first 100 m for gusty cases when the observed gust was $g > 15m/s$, with a particular under-prediction from the Boulac PBL scheme. The Ri forecast was over-predicted in all the PBL schemes, with Boulac showing a particular over-prediction of Ri when $g > 15m/s$.

For all PBL schemes, the established, theory-based gust parameterization based on mean velocity and friction velocity from the ECMWF forecast the gusts reasonably at hub wind turbine height (100 m), with increasing skill when the grid resolution was increased. The GP proposed in this work showed better performance in the gross domain (12 km). Increased mean and gust values were forecast with increasing horizontal grid resolutions, and an increasing skill in gusty cases with increasing grid resolution was observed.

Analysis of the time intervals of the forecast alarms for gusty cases showed an increase in TA and a decrease in FA when the time intervals increased. The GP proposed can be useful in an operational model because of its lower computational cost, considering the best skill in gross domain compared to ECMWF.

In this work, the forecast horizon was not evaluated. This result can be considered in terms of having a better configuration, relative to other models. If an operational model needs to be implemented, further analysis of the time horizon and impact on skill with ensembles needs to be computed.

Chapter 9

Appendix

- 9.1 Diurnal cycle by seasons of mean wind observed and forecast velocity by each PBL scheme

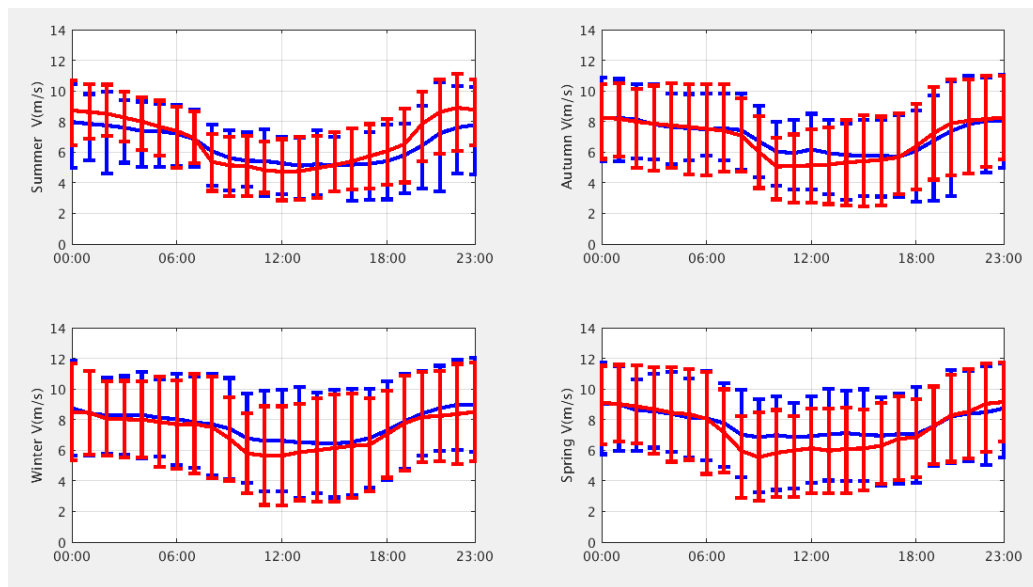


Figure 9.1: Mean wind velocity at 101.8 meters at CE tower diurnal cycle by seasons, blue observed velocity, red computed by WRF with YSU PBL scheme, 4 km horizontal grid resolution, vertical bar considering 16th and 84th percentiles.

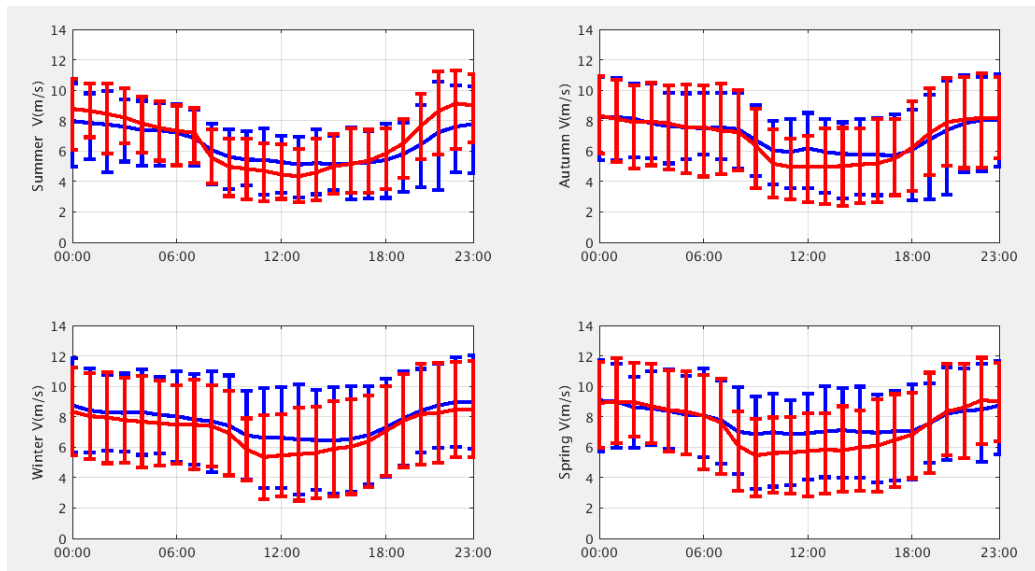


Figure 9.2: Mean wind velocity at 101.8 meters at CE tower diurnal cycle by seasons, blue observed velocity, red computed by WRF with MYJ PBL scheme, 4 km horizontal grid resolution, vertical bar considering 16th and 84th percentiles.

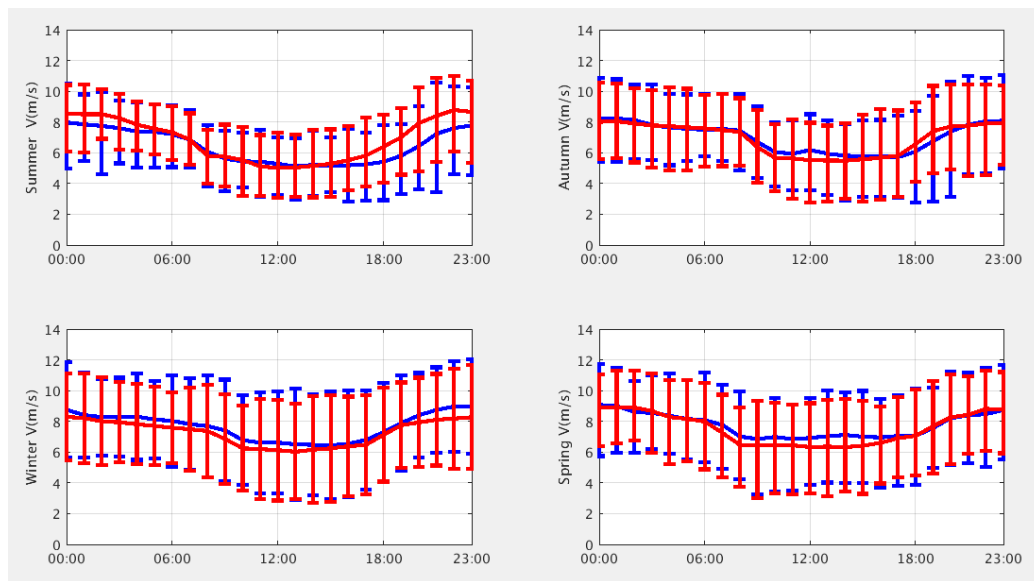


Figure 9.3: Mean wind velocity at 101.8 meters at CE tower diurnal cycle by seasons, blue observed velocity, red computed by WRF with ACM2-Pleim PBL scheme, 4 km horizontal grid resolution, vertical bar considering 16th and 84th percentiles.

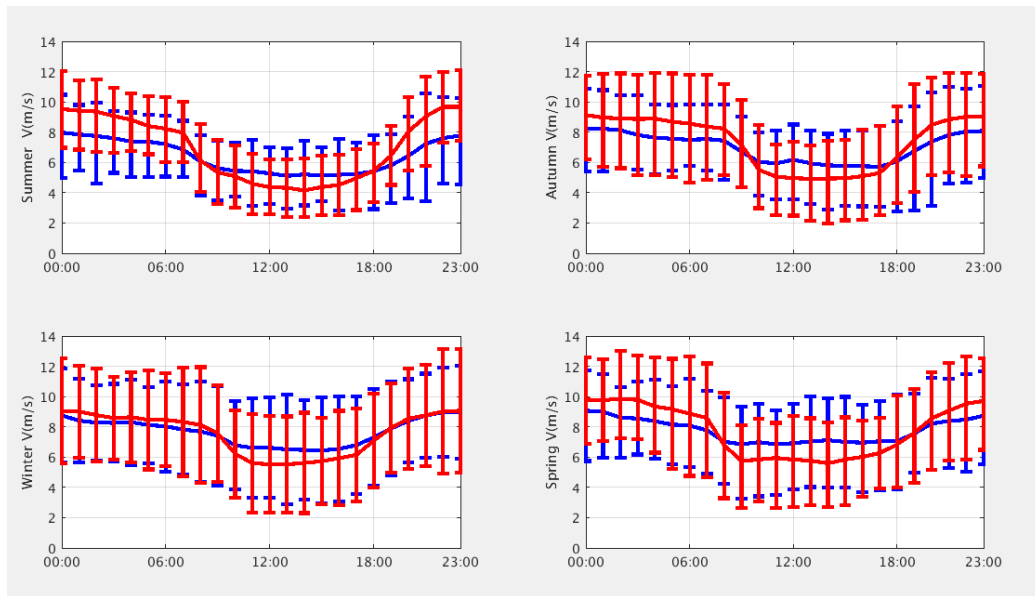


Figure 9.4: Mean wind velocity at 101.8 meters at CE tower diurnal cycle by seasons, blue observed velocity, red computed by WRF with Bretherton Park PBL scheme, 4 km horizontal grid resolution, vertical bar considering 16th and 84th percentiles.

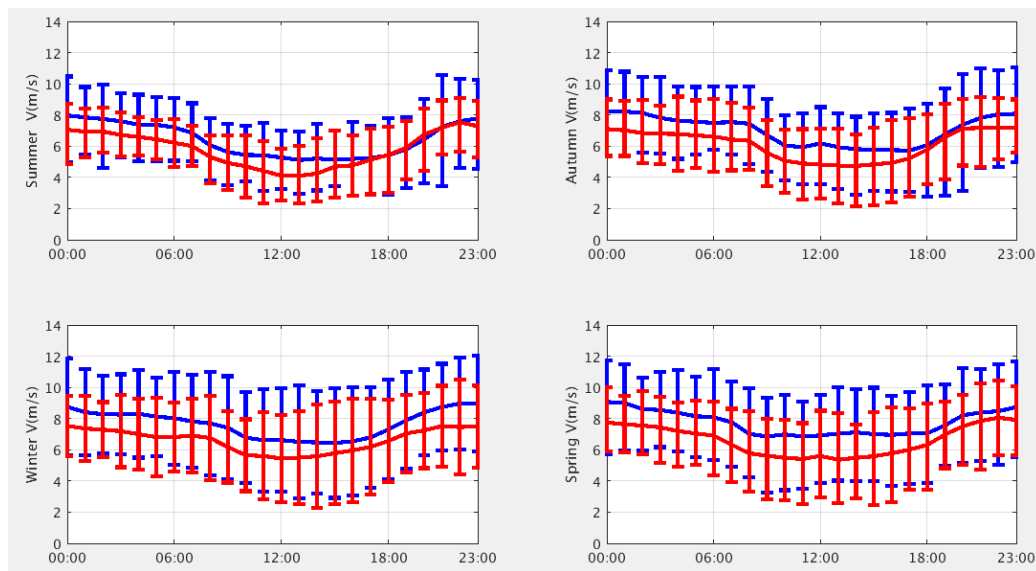


Figure 9.5: Mean wind velocity at 101.8 meters at CE tower diurnal cycle by seasons, blue observed velocity, red computed by WRF with Bretherton-Park PBL scheme, 4 km horizontal grid resolution, vertical bar considering 16th and 84th percentiles.

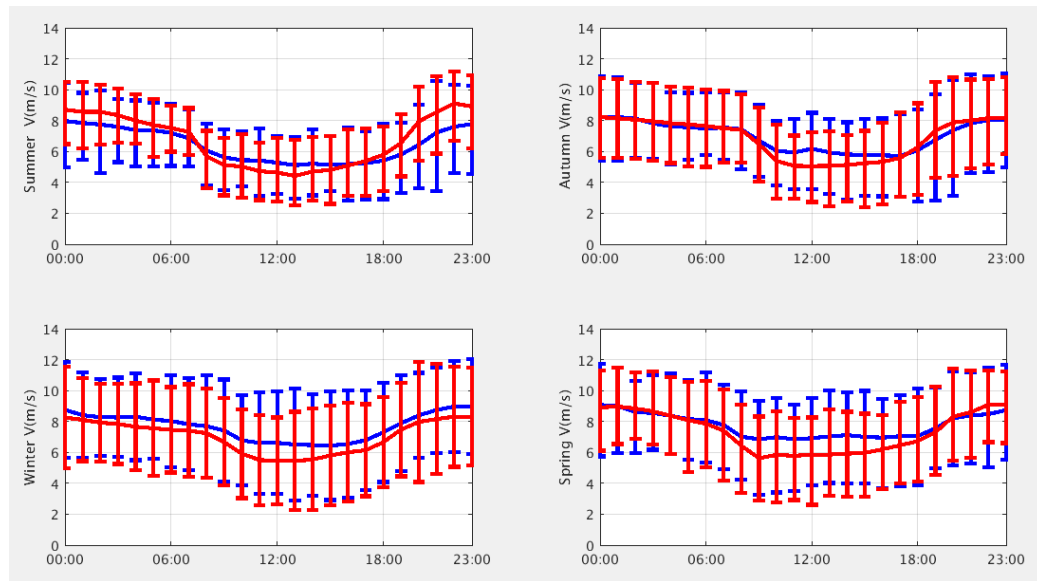


Figure 9.6: Mean wind velocity at 101.8 meters at CE tower diurnal cycle by seasons, blue observed velocity, red computed by WRF with GBM PBL scheme, 4 km horizontal grid resolution, vertical bar considering 16th and 84th percentiles.

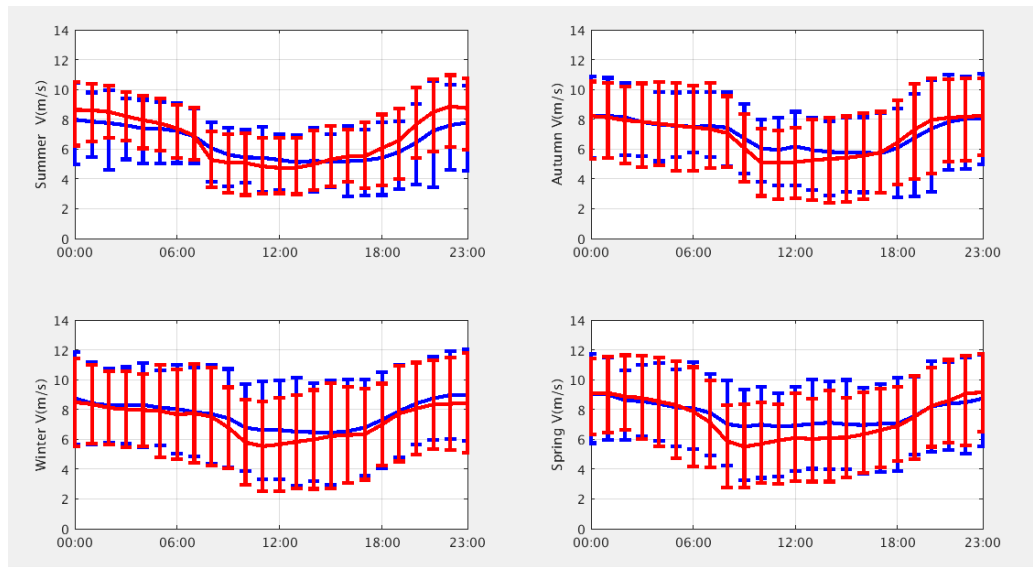


Figure 9.7: Mean wind velocity at 101.8 meters at CE tower diurnal cycle by seasons, blue observed velocity, red computed by WRF with Shin-Hong PBL scheme, 4 km horizontal grid resolution, vertical bar considering 16th and 84th percentiles.

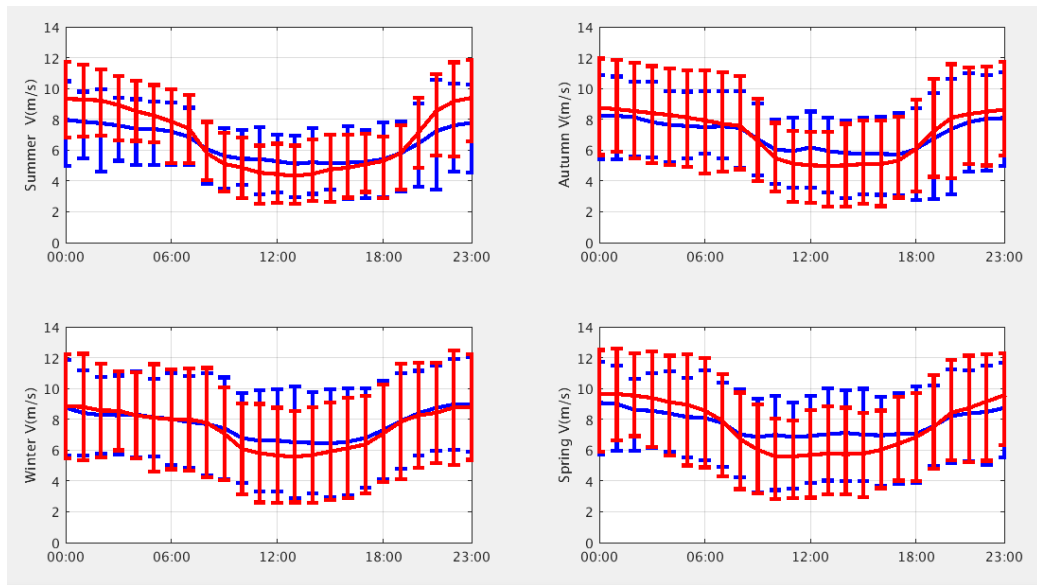


Figure 9.8: Mean wind velocity at 101.8 meters at CE tower diurnal cycle by seasons, blue observed velocity, red computed by WRF with MYNN PBL scheme, 4 km horizontal grid resolution, vertical bar considering 16th and 84th percentiles.

9.2 Diurnal cycle by seasons of PBL height computed by different schemes

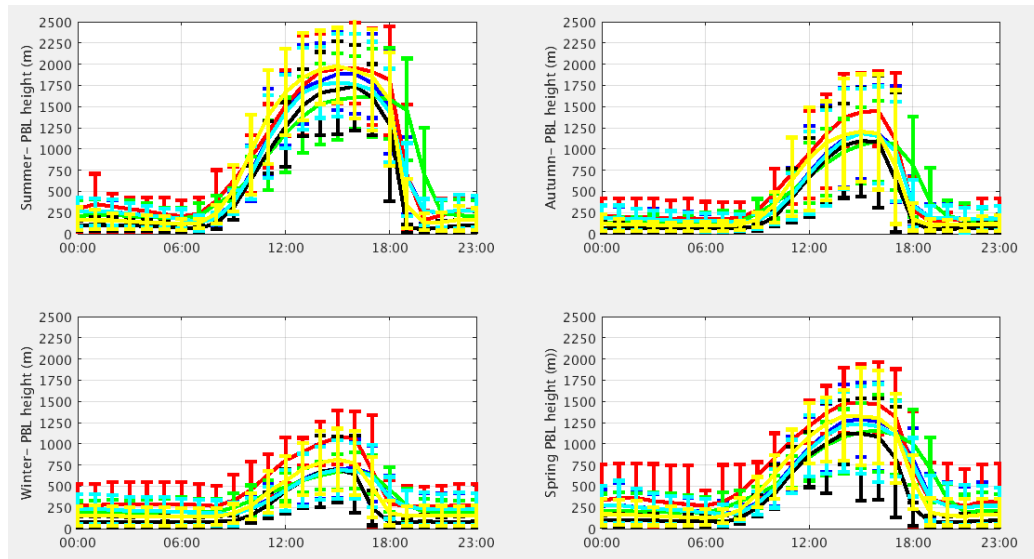


Figure 9.9: Diurnal cycle by seasons of PBL height computed by different schemes, 4 km horizontal grid resolution, blue YSU, red MYJ, yellow ACM2, black Bretherton Park, cyan Shin-Hong, green MYNN, vertical bar considering 16th and 84th percentiles

9.3 Gust Parametrization Coefficients

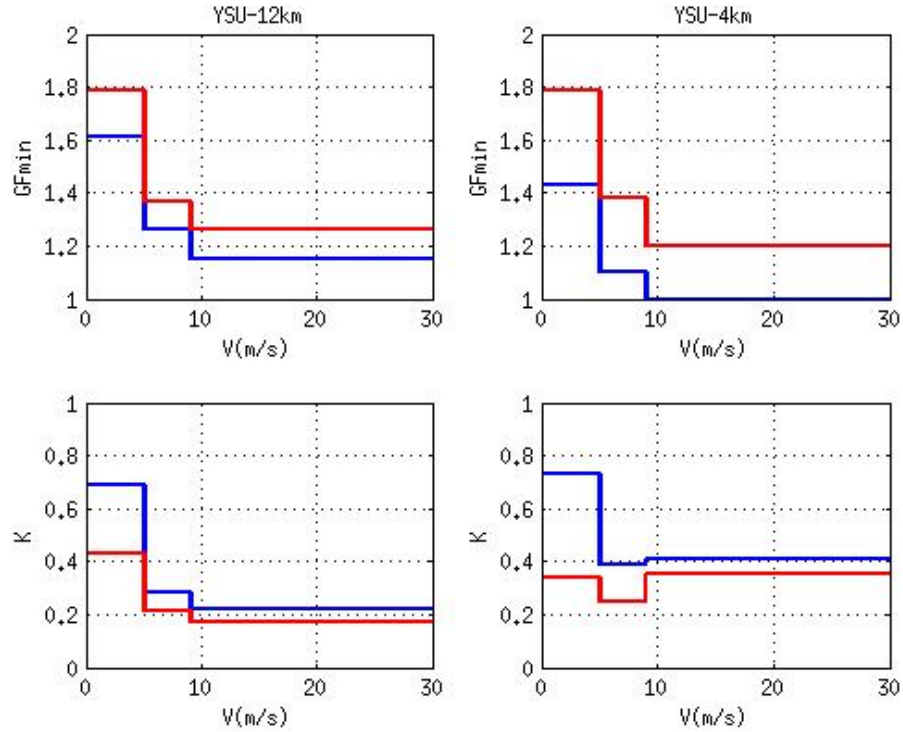


Figure 9.10: K and G_{min} optimal fit with CE tower observational data for YSU 12km and 0.44km horizontal grid resolution, blue for $\frac{\partial T}{\partial z} \geq 0$ and red for $\frac{\partial T}{\partial z} < 0$, intervals of velocities computed by WRF $0m/s < V \leq 5m/s$, $5m/s \leq V < 9m/s$ and $9m/s \leq V$

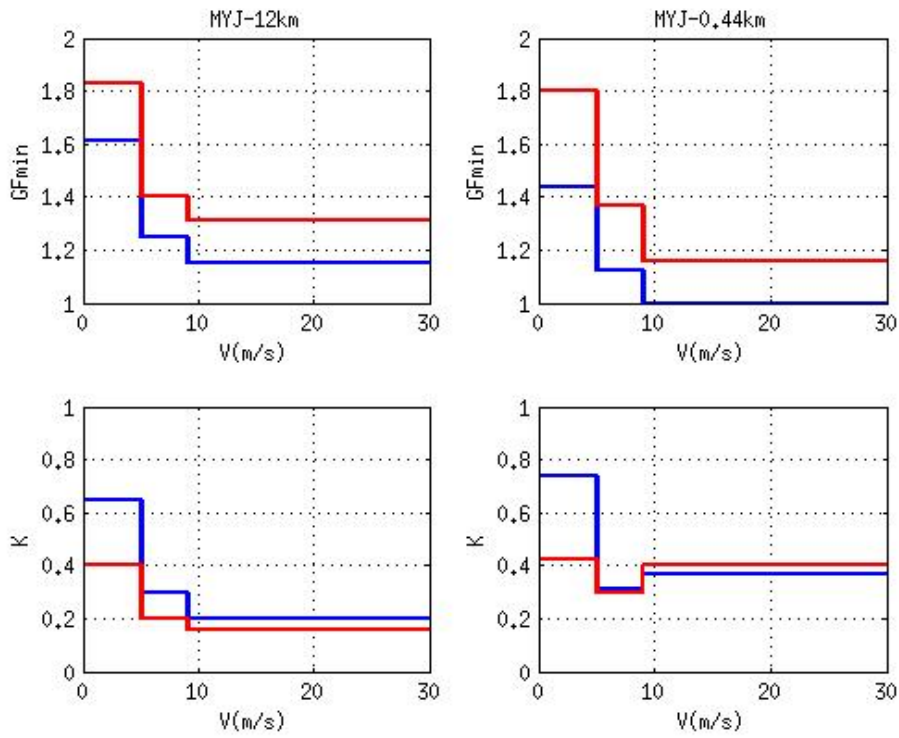


Figure 9.11: K and G_{min} optimal fit with CE tower observational data for MYJ 12km and 0.44km horizontal grid resolution, blue for $\frac{\partial T}{\partial z} \geq 0$ and red for $\frac{\partial T}{\partial z} < 0$, intervals of velocities computed by WRF $0m/s < V \leq 5m/s$, $5m/s \leq V < 9m/s$ and $9m/s \leq V$

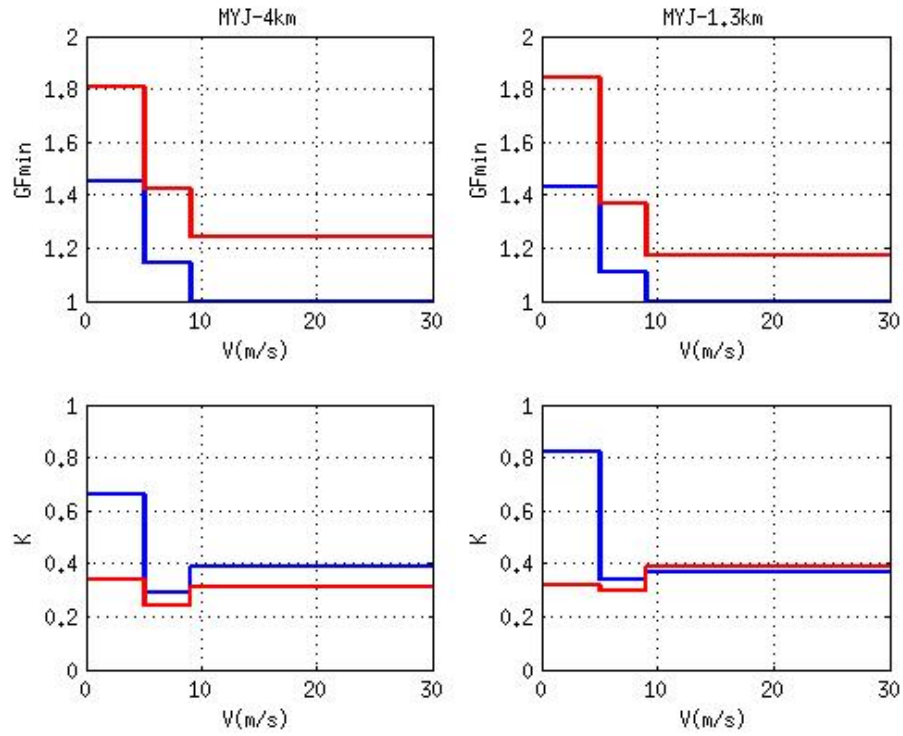


Figure 9.12: K and G_{min} optimal fit with CE tower observational data for YSU 4km and 1.3km horizontal grid resolution, blue for $\frac{\partial T}{\partial z} \geq 0$ and red for $\frac{\partial T}{\partial z} < 0$, intervals of velocities computed by WRF $0m/s < V \leq 5m/s$, $5m/s \leq V < 9m/s$ and $9m/s \leq V$

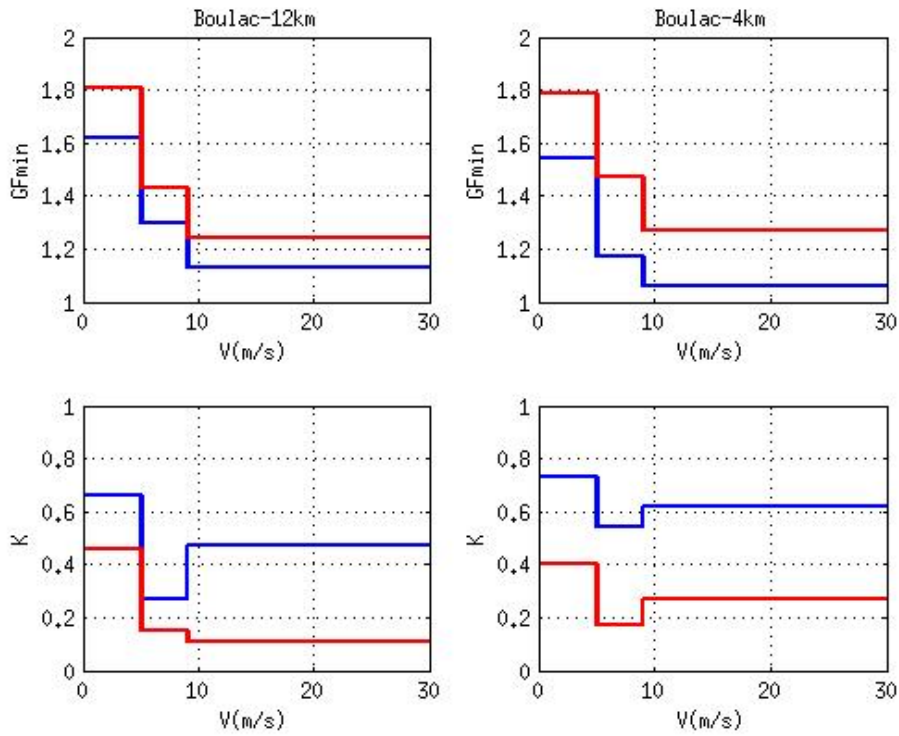


Figure 9.13: K and G_{min} optimal fit with CE tower observational data for Boulac 12km and 4km horizontal grid resolution, blue for $\frac{\partial T}{\partial z} \geq 0$ and red for $\frac{\partial T}{\partial z} < 0$, intervals of velocities computed by WRF $0m/s < V \leq 5m/s$, $5m/s \leq V < 9m/s$ and $9m/s \leq V$

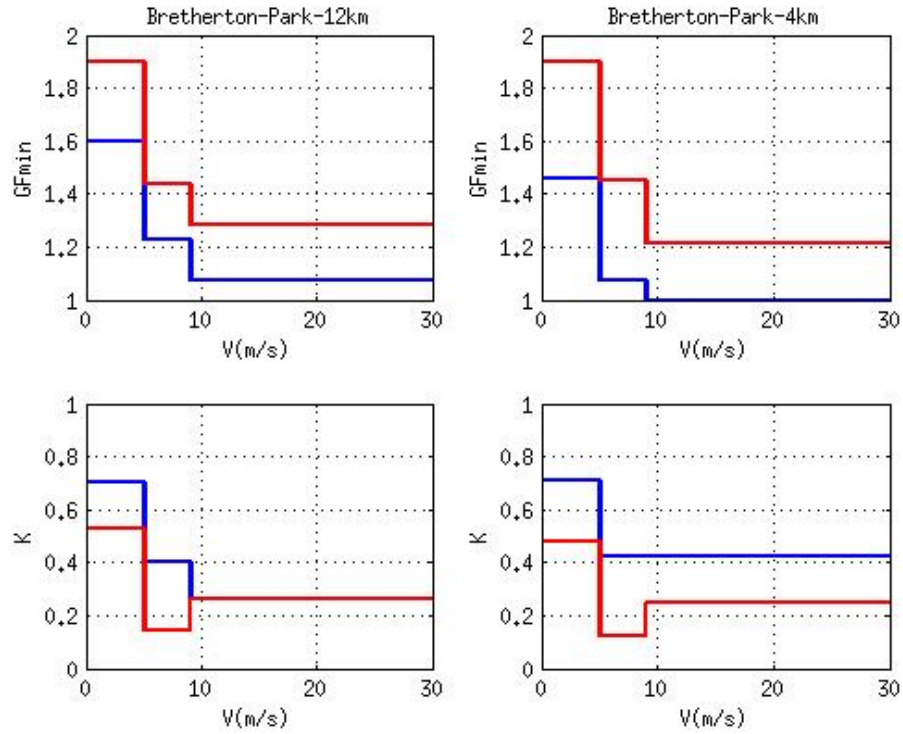


Figure 9.14: K and G_{min} optimal fit with CE tower observational data for Bretherton Park 12km and 4km horizontal grid resolution, blue for $\frac{\partial T}{\partial z} \geq 0$ and red for $\frac{\partial T}{\partial z} < 0$, intervals of velocities computed by WRF $0m/s < V \leq 5m/s$, $5m/s \leq V < 9m/s$ and $9m/s \leq V$

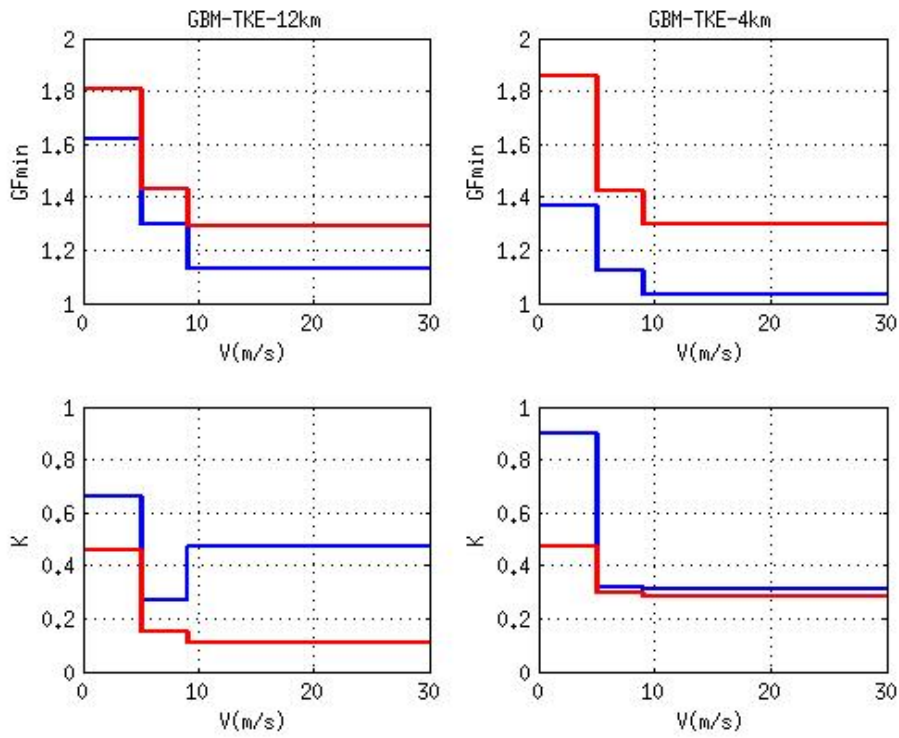


Figure 9.15: K and G_{min} optimal fit with CE tower observational data for GBM-TKE 12km and 4km horizontal grid resolution, blue for $\frac{\partial T}{\partial z} \geq 0$ and red for $\frac{\partial T}{\partial z} < 0$, intervals of velocities computed by WRF $0m/s < V \leq 5m/s$, $5m/s \leq V < 9m/s$ and $9m/s \leq V$

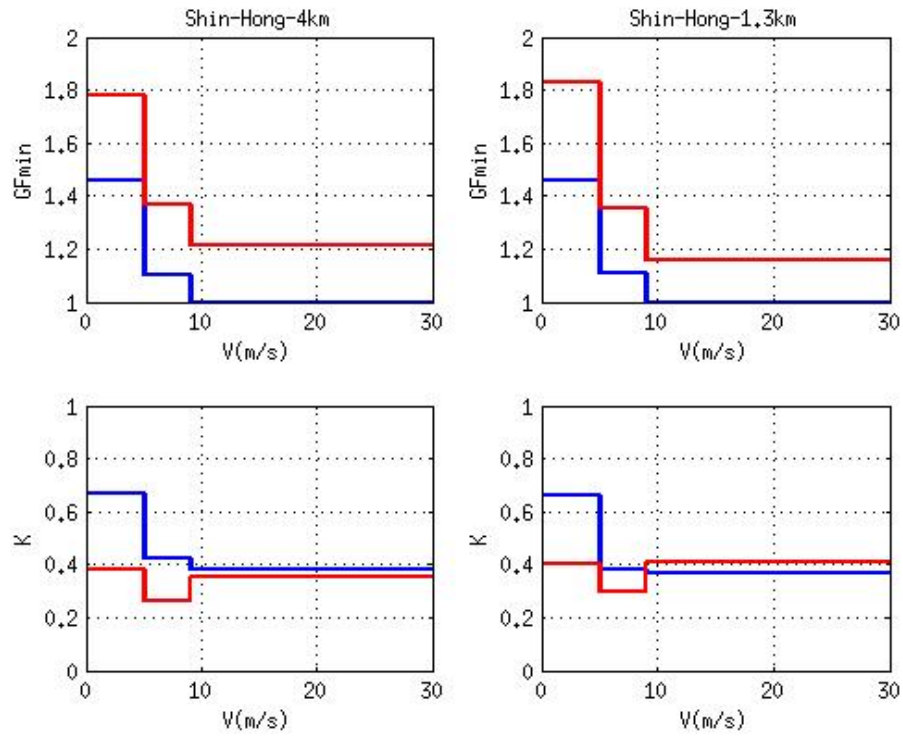


Figure 9.16: K and G_{min} optimal fit with CE tower observational data for Shin-Hong 4km and 1.3km horizontal grid resolution, blue for $\frac{\partial T}{\partial z} \geq 0$ and red for $\frac{\partial T}{\partial z} < 0$, intervals of velocities computed by WRF $0m/s < V \leq 5m/s$, $5m/s \leq V < 9m/s$ and $9m/s \leq V$

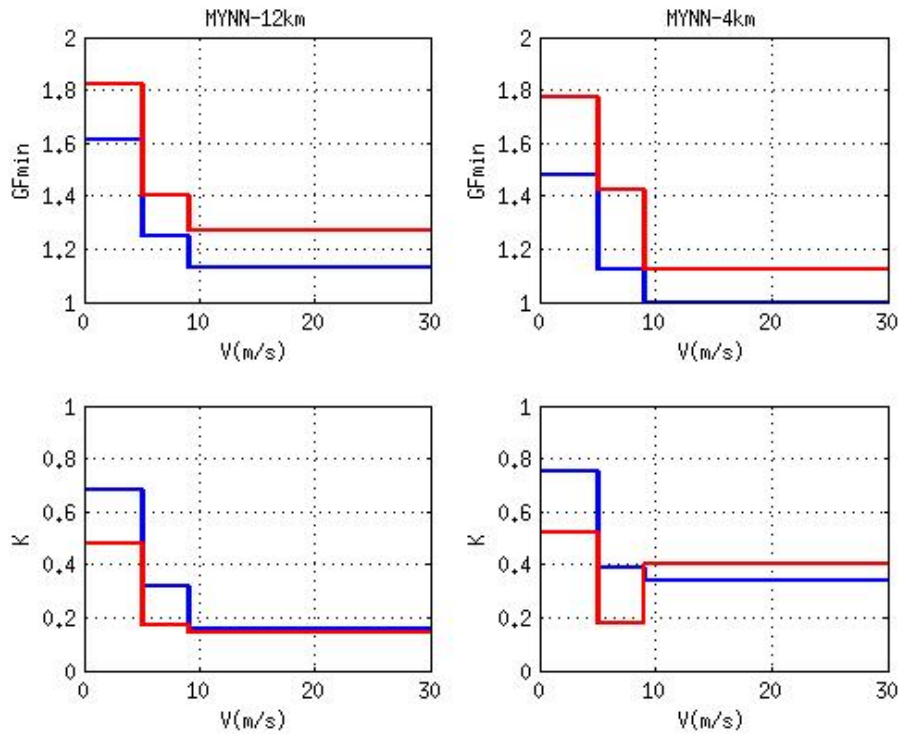


Figure 9.17: K and G_{min} optimal fit with CE tower observational data for MYNN 12km and 14km horizontal grid resolution, blue for $\frac{\partial T}{\partial z} \geq 0$ and red for $\frac{\partial T}{\partial z} < 0$, intervals of velocities computed by WRF $0m/s < V \leq 5m/s$, $5m/s \leq V < 9m/s$ and $9m/s \leq V$

Bibliography

- [Abal, 2011] González Abal, Mauro D' Angelo, José Cataldo, Alejandro Gutiérrez. Mapa Solar del Uruguay Versión 1.0 Memoria Técnica. 2011. ISBN 978-9974-0-0847-2.
- [Acevedo, 2001] Acevedo, O.C, Fitzjarrald, D.R.(2001) The Early Evening Surface-Layer Transition: Temporal and Spatial Variability. Journal of the Atmospheric Sciences: Vol. 58, No. 17, pp. 2650-2667.
- [Ackerman, 2005] Ackerman, Thomas, Wind Power in Power Systems, 2005, Wiley, ISBN 0-470-85508-8
- [AMS glossary, 2017] [http : //glossary.ametsoc.org/wiki/Atmosphere](http://glossary.ametsoc.org/wiki/Atmosphere)
- [Anca, 2010] Anca D. Hansen, Nicolaos A. Cutululis, Helen Markou, Poul Sørensen, Florin IovGrid fault and design-basis for wind turbines -Final report Sørensen, Florin Iov Risø-R-1714(EN) January 2010
- [Arakawa, 1977] Arakawa, A., and Lamb, V. R. (1977), "Computational design of the basic dynamical processes of the UCLA general circulation model". Methods in Computational Physics: Advances in Research and Applications, 17, 173-265.
- [Arakawa, 2004] Arakawa, A., 2004: The cumulus parameterization problem: Past, present, and future. J. Climate, 17, 2493-2525. Link
- [Arya, 1998] Arya, S. Pal (1998). Air Pollution Meteorology and Dispersion (1st Edition ed.). Oxford University Press. ISBN 0-19-507398-3.

- [Blackadar, 1957] Blackadar, A. K. 1957: Boundary layer wind maxima and their significance for the growth of the nocturnal inversions. *Bull. Amer. Meteor. Soc.*, 38, 283-290.
- [Bougeault and Lacarrere, 1989] Bougeault, P., and P. Lacarrère, 1989: Parameterization of orography-induced turbulence in a mesobeta-scale model. *Mon. Wea. Rev.*, 117, 1872-1890, doi:10.1175/1520-0493(1989)117,1872:POOITI.2.0.CO;2.
- [Bretherton and Park, 2009] Bretherton, C. S., and S. Park, 2009: A new moist turbulence parameterization in the Community Atmosphere Model. *J. Climate*, 22, 3422-3448, doi:10.1175/2008JCLI2556.1.
- [Businger, 1971] Businger, J. A., J. C. Wyngaard, Y. Izumi, and E. F. Bradley, 1971: Flux-profile relationships in the atmospheric surface layer. *J. Atmos. Sci.*, 28, 181-189.
- [Charney, 1950] Charney, J. G., Fjörtft, R. and von Neumann, J 1950 Numerical integration of the barotropic vorticity equation. *Tellus* 2,237-254
- [Chen, 2001] Chen, F., and J. Dudhia, 2001: Coupling an advanced land-surface/ hydrology model with the Penn State/ NCAR MM5 modeling system. Part I: Model description and implementation. *Mon. Wea. Rev.*, 129, 569-585.
- [Cotton, 1989] William R. Cotton *Storm and Cloud Dynamics* 1989, Department of Atmospheric Science Colorado State University Fort Collins, Colorado ISBN 0-12-192530-7
- [Czarnetzki, 2012] Czarnetzki, A. C., 2012: Persistent daytime superadiabatic surface layers observed by a microwave temperature profiler. Preprints, 37th Natl. Wea. Assoc. Annual Meeting, Madison, WI, Natl. Wea. Assoc., P2.55.
- [de Almeida, Gutierrez, 2015] Everton de Almeida Lucas, Alejandro Gutierrez Arce, Marcelo Romero de Moraes, Gabriel Cazes Boezio, Jose

Cataldo Ottieri Descrição estatística do ciclo diário do vento nos primeiros 100 metros de altura da C.L.P na localidade de Colonia Eulacio, Uruguai, *Ciência e Natura* v.38 Ed. Especial- IX Workshop Brasileiro de Micrometeorologia 2016, p. 426– 434

- [Dudhia, 2006] Hong, S. Y. Noh, and J. Dudhia, 2006: A new vertical diffusion package with an explicit treatment of entrainment processes. *Mon. Wea. Rev.*, 134, 2318–2341, doi:10.1175/MWR3199.1.
- [Floors, 2013] R. Floors C. L. Vincent S. -E. Gryning A. Peña E. Batchvarova The Wind Profile in the Coastal Boundary Layer: Wind Lidar Measurements and Numerical Modelling *Boundary-Layer Meteorol* (2013) 147: 469. doi:10.1007/s10546-012-9791-9
- [Fovell, 2005] Fovell Robert 2005 Convective initiation ahead of the sea breeze front. *Mon Weather Rev* 133: 264–278
- [Fovell, 2016] Fovell and Cao (2016), "The Santa Ana winds of Southern California: Winds, gusts, and the 2007 Witch fire", *Wind and Structures*, in press.
- [Fox, 2014] Brendan Fox, Damian Flynn and Leslie Bryans. *Wind Power Integration: Connection and system operational aspects*, 2nd Edition, 2014 IET Digital Library ISBN: 978-1-84919-493-8
- [Friederichs, 2009] Petra Friederichs , Martin Gober , Sabrina Bentzien, Anne Lenz and Rebekka Krampitz, 2009 A probabilistic analysis of wind gusts using extreme value statistics *Meteorologische Zeitschrift*, Vol. 18, No. 6, 615-629 (December 2009)
- [Fujita, 1981] Fujita, T. T., 1981: Tornadoes and downbursts in the context of generalized planetary scales. *J. Atmos. Sci.*, 38, 1511–1534.
- [Gray, 2003] Gray, M. E. B., 2003: The use of a cloud resolving model in the development and evaluation of a probabilistic forecasting algorithm for convective gusts. *Meteorol. Appl.* 10, 239–252.

- [Grenier, 2001] Grenier, H., and C. S. Bretherton, 2001: A moist PBL parameterization for large-scale models and its application to subtropical cloud-topped marine boundary layers. *Mon. Wea. Rev.*, 129, 357–377, doi:10.1175/1520-0493(2001)129,0357:AMPPFL.2.0.CO;2.
- [Gutierrez and Fovell, 2015] Alejandro Gutierrez Arce Robert G Fovell. Gust forecasting in Uruguay in support of wind energy. 14th International Conference on Wind Engineering Porto Alegre, Brazil June 21-26, 2015
- [Gutierrez, 2015] Alejandro Gutierrez Arce Description of Intensity of Turbulence IT in dependence with stability regime at swept area of wind turbines blades heights. 14Th International Conference on Wind Engineering – Porto Alegre, Brazil – June 21-26, 2015
- [Holtslag and Bruin, 1988] Holtslag, A. A. M. and H. A. R. de Bruin, 1988: Applied modeling of the nighttime surface energy balance over land. *J. Appl. Meteor.*, 27, 689–704.
- [IEC.61400-12, 1998] IEC. 61400-12. First edition. 1998-02. Wind turbine generator systems . Part 12: Wind turbine power performance testing
- [IFS, 2011] IFS DOCUMENTATION Cy37r2Operational implementation 18 May 2011 PART IV: PHYSICAL PROCESSES
- [Kaimal, 1976] J.C Kaimal, J. C. Wyngaard, D. A. Haugen, O. R. Coté, Y. Izumi, S. J. Caughey, and C. J. Readings, 1976: Turbulence Structure in the Convective Boundary Layer. *J. Atmos. Sci.*, 33, 2152–2169.
- [Kain, 2004] Kain, J. S., 2004: The Kain-Fritsch convective parameterization: An update. *J. Appl. Meteor.*, 43, 170–181.
- [Kalnay, 2003] Eugenia Kalnay. *Atmospheric Modeling, Data Assimilation and Predictability*. Cambridge University Press, UK, 2003
- [Khairoutdinov, 2005] Khairoutdinov, M. F., D. A. Randall, and C. DeMott, 2005: Simulations of the atmospheric general circulation using a cloud-resolving model as a superparameterization of physical processes. *J. Atmos. Sci.*, 62, 2136–2154, doi:10.1175/JAS3453.1.

- [Ligda, 1951] Ligda, M. G. H., 1951: Radar storm observation. *Compendium of Meteorology*, T. F. Malone, Ed., Amer. Meteor. Soc., 1265–1282.
- [Markowski, 2010] Paul Markowski and Yvette Richardson, *Mesoscale Meteorology in Midlatitudes* Penn State University, University Park, PA, USA 2010 by John Wiley Sons, Ltd
- [Lin, 1983] Lin, Y.-L., R. D. Farley, and H. D. Orville, 1983: Bulk parameterization of the snow field in a cloud model. *J. Climate Appl. Meteor.*,
- [Liou, 2002] K. N. Liou Academic Press. *An Introduction to Atmospheric Radiation*
- [Mellor and Yamada, 1974] Mellor, G. L., and T. Yamada, 1974: A hierarchy of turbulence closure models for planetary boundary layers. *J. Atmos. Sci.*, 31, 1791–1806, doi:10.1175/15200469(1974)031<1791:AHOTCM.2.0.CO;2.
- [Mellor and Yamada, 1982] Mellor, G. L., and T. Yamada, 1982: Development of a turbulence closure model for geophysical fluid problems. *Rev. Geophys. Space Phys.*, 20, 851–875, doi:10.1029/RG020i004p00851.
- [Mlawe, 1997] Mlawer, E. J., S. J. Taubman, P. D. Brown, M. J. Iacono, and S. A. Clough, 1997: Radiative transfer for inhomogeneous atmosphere: RRTM, a validated correlated-k model for the long-wave. *J. Geophys. Res.*, 102 (D14), 16663–16682.
- [Monin, 1954] Monin, A. S and A. M. Obukhov, Basic laws of turbulent mixing in the ground layer of the atmosphere. 1954 *Trans. Geophys. Inst Akad. Nauk USSR* 151 163-187.
- [Nakanishi 2001] Nakanishi, M., 2001: Improvement of the Mellor Yamada turbulence closure model based on large-eddy simulation data. *Boundary Layer Meteor.*, 99, 349–378, doi:10.1023/A:1018915827400.
- [Nakamura, 1996] Nakamura, K., R. Kershaw, and N. Gait, 1996: Prediction of near-surface gusts generated by deep convection. *Meteorol. Appl.*, 3, 157–167.

- [Orlanski, 1975] Orlanski, I., 1975: A rational subdivision of scales for atmospheric processes. *Bull. Amer. Meteor. Soc.*, 56, 527-530.
- [Panofsky, 1977] Panofsky, H. A., Tennekes, H., Lenschow, D. H. and Wyngaard, J. C. (1977). The characteristics of turbulent velocity components in the surface layer under convective conditions. *Boundary-Layer Meteorol.*, 11, 355-361.
- [Pasquill 1961] Pasquill, F., The Estimation of the Dispersion of Windborne Material, *The Meteorological Magazine*, Vol. 90, No. 1063 (1961).
- [Paulson, 1970] Paulson, C. A., 1970: The mathematical representation of wind speed and temperature profiles in the unstable surface layer. *J. Appl. Meteor.*, 9, 857-861.
- [Peña, 2010] Pena Diaz, Alfredo; Gryning, Sven-Erik; Mann, Jakob. On the length-scale of the wind profile. *Royal Meteorological Society. Quarterly Journal*, Vol. 136, No. 653, 2010, p. 2119-2131.
- [Pielke, 2013] Roger A Pielke 2013 *Mesoscale Meteorological Modeling* Academic Press eBook ISBN: 9780123852380
- [Pleim, 2007a] Pleim, J. E., 2007a: A combined local and nonlocal closure model for the atmospheric boundary layer. Part I: Model description and testing. *J. Appl. Meteor. Climatol.*, 46, 1383-1395, doi:10.1175/JAM2539.1.
- [Pleim, 2007b] Pleim, J. E., 2007b: A combined local and nonlocal closure model for the atmospheric boundary layer. Part II: Application and evaluation in a mesoscale meteorological model. *J. Appl. Meteor. Climatol.*, 46, 1396-1409, doi:10.1175/JAM2534.1.
- [Prandtl, 1925] Prandtl, L.: Bericht fiber Untersuchungen zur ausgebildeten Turbulenz. *Z. Angew. Math. Mech.*, Bd. 5, Heft 2, Apr. 1925, pp. 136-139.
- [Randall, 2003] Randall, D., M. Khairoutdinov, A. Arakawa, and W. Grabowski, 2003: Breaking the cloud parameterization deadlock. *Bull. Amer. Meteor. Soc.*, 84, 1547-1564, doi:10.1175/BAMS-84-11-1547.

- [Randall, 2000] David Randall 2000 General Circulation Model Development, Past, Present, and Future Volume 70 1st Edition ISBN: 9780080507231
- [Sheridan, 2011] P. Sheridan 2011, Review of techniques and research for gust forecasting and parameterisation Forecasting Research Technical Report 570 www.metoffice.gov.uk
- [Shin and Hong, 2013] Shin, H., and S. Hong, 2013: Analysis on resolved and parameterized vertical transports in convective boundary layers at gray-zone resolutions. *J. Atmos. Sci.*, 70, 3248-3261, doi:10.1175/JAS-D-12-0290.1.
- [Shin and Hong, 2015] Shin, H., and S. Hong 2015 Representation of the Subgrid-Scale Turbulent Transport in Convective Boundary Layers at Gray-Zone Resolutions *J. Atmos. Sci.*, DOI: <http://dx.doi.org/10.1175/MWR-D-14-00116.1>
- [Skamarock, 2008] Skamarock, 2008 NCAR/TN 475+STRNCAR TECHNICAL NOTE June 2008 A Description of the Advanced Research WRF Version 3
- [Siuta, 2017] Siuta, D., G. West, T. Nipen, and R. Stull, 2017: Calibrated probabilistic hub-height wind forecasts in complex terrain. *Wea. Forecasting*, doi:10.1175/WAF-D-16-0137.1, in press. Link
- [Stensurd, 2007] David J. Stensurd Parameterization Schemes: Keys to Understanding Numerical Weather Prediction Models Cambridge University Press 2007
- [Stull, 1988] Stull R.B.. 1988. An Introduction to Boundary Layer Meteorology (Atmospheric Sciences Library). Kluwer Academic Publishers, Dordrecht. ISBN 90-277-2768-6.
- [Stull, 2016] Roland Stull, Practical Meteorology An Algebra-based Survey of Atmospheric Science Copyright ©, 2016 Dept. of Earth, Ocean At-

atmospheric Sciences University of British Columbia ISBN-13: 978-0-88865-176-1

[Talke, 1983] Takle, E. S., 1983: Climatology of superadiabatic conditions for a rural area. *J. Climate Appl. Meteor.*, 22, 1129-1132.

[Tennekes, 1972] H. Tennekes J. L. Lumley, 1972 *A First Course in Turbulence*, (MIT Press, Cambridge, MA 1972), Section 8.2, p. 256-7

[Trenberth, 2009] Kevin E. Trenberth, John T. Fasullo, and Jeffrey Kiehl 2009 EARTH'S GLOBAL ENERGY BUDGET DOI:10.1175/2008BAMS2634.1 ©2009 American Meteorological Society 29 July 2008

[Troen, Marth 1986] Troen IB, Mahrt, 1986 L A simple model of the Atmospheric Boundary Layer; Sensitivity to surface evaporation *Boundary-Layer Meteorology*, Volume 37, Issue 1-2, pp 129-148

[web, UTE] www.ute.com.uy

[Wieringa, 1973] Wieringa J 1973 Gust factors over open water and built up country. *Bound Layer Meteor* 3:424-441

[Wyngaard, 1985] Wyngaard, J. C., 1985: Structure of the planetary boundary layer and implications for its modeling. *J. Climate Appl. Meteor*, 24, 1131-1142.

[Wyngaard, 1983] Wyngaard, J. C. and Richard Brost 1983, Top-Down and Bottom-Up Diffusion of a Scalar in the Convective Boundary Layer *J. Climate Appl. Meteor*, vol 41.

[Wyngaard, 2004] Wyngaard, J. C.: Toward numerical modelling in the Terra Incognita, *J. Atmos. Sci.*, 61, 1816-1826, 2004.